FLUID STRUCTURE INTERACTION BY MEANS OF REDUCED ORDER MODELS

FLUID STRUCTURE INTERACTION BY MEANS OF REDUCED ORDER MODELS

ALEXIS TELLO GUERRA

A Field to Field approach

May 2020

Alexis Tello Guerra

Fluid Structure Interaction by means of Reduced Order Models

May 2020

PhD in Structural Analysis
Escola Tècnica Superior d’Enginyers de Camins, Canals i Ports de Barcelona
Universitat Politècnica de Catalunya
c/ Jordi Girona 1-3, 08034 Barcelona
https://www.upc.edu/

Advisor: Ramon Codina Rovira
Joan Baiges Aznar

Ogorek, ogorek, ogorek, Zielony ma
garniturek, I czapke i sandaly, Zielony,
zielony jest caly.
Dla Mosy

ABSTRACT

The standard Fluid-Structure Interaction coupling (velocity–pressure/displacement) is compared against two novel types of coupling, a Two Field coupling (velocity–pressure/displacement–pressure) and a Three Field coupling (velocity–pressure–stress/displacement–pressure–stress) in this way completing our set of, what we call, field to field equations, all stabilized by means of the Variational Multi-Scale method using dynamic and orthogonal sub-scales. The solid Two field fluid structure interaction coupling formulation is benchmarked statically and dynamically. Proper Orthogonal Decomposition is applied to all three fluid structure interaction formulations to obtain reduced basis and asses their performance in a reduced space. Usual numerical benchmarks are shown comparing all three formulations. The three field Fluid Structure Interaction coupling proves to provide very accurate results in both Full Order Model and Reduced Order Model spaces, making it a reliable formulation. Field to field pairing appears to be beneficial providing more accurate results in all cases shown.

A Reduced Order Model designed by means of a Variational Multi-Scale method stabilized formulation has been applied successfully to Fluid-Structure Interaction problems in a strongly coupled partitioned solution scheme. Details of the formulation and the implementation both for the interaction problem and for the reduced models, for both the off-line and on-line phases, are shown. Results are obtained for cases in which both domains are reduced at the same time. Numerical results are presented for a semi-stationary and a fully transient case.

ACKNOWLEDGMENTS

This project has been possible thanks to the Colciencias scholarship for doctoral studies abroad (call 568 of 2012) from the Colombian government.

CONTENTS

INTRODUCTION 1

1 THE VARIATIONAL MULTI-SCALE METHOD 5
- 1.1 Some standard notation . . . 5
- 1.2 A generic variational problem . . . 6
- 1.3 Algebraic sub-grid scales . . . 7
- 1.4 Dynamic sub-grid scales . . . 8
- 1.5 Orthogonal sub-grid scales . . . 10

I SOLID ELASTO-DYNAMICS

2 IRREDUCIBLE SOLID EQUATIONS 15
- 2.1 Governing equations . . . 15
- 2.2 Weak form . . . 16
- 2.3 Spatial discretization . . . 16
- 2.4 Time discretization . . . 17

3 TWO FIELD SOLID EQUATIONS 18
- 3.1 Split of the stress tensor and field equations . . . 19
- 3.2 Linearization . . . 20
- 3.3 Initial and boundary-value problem . . . 21
- 3.4 Weak form . . . 22
- 3.5 Galerkin spatial discretization . . . 23
- 3.6 Stabilization . . . 23

4 THREE FIELD SOLID EQUATIONS 26
- 4.1 Split of the stress tensor and field equations . . . 26
- 4.2 Linearization . . . 27
- 4.3 Governing equations . . . 28
- 4.4 Weak form . . . 28
- 4.5 Galerkin spatial discretization . . . 30
- 4.6 Stabilization . . . 30

II FLUID DYNAMICS

5 TWO FIELD NAVIER-STOKES EQUATIONS 39
5.1 Governing equations . . . 39
5.2 Weak form . . . 40
5.3 Galerkin spatial discretization . . . 40
5.4 Time discretization . . . 41
5.5 Stabilization . . . 41

6 THREE FIELD NAVIER-STOKES EQUATIONS 43
6.1 Governing equations . . . 43
6.2 Weak form . . . 43
6.3 Galerkin spatial discretization . . . 44
6.4 Stabilization . . . 44

III FLUID STRUCTURE INTERACTION

7 FIELD TO FIELD PROBLEM 51
7.1 Weak form of the Field to Field problem . . . 51

8 COUPLING SCHEME 55

9 THE ALGORITHM 58

IV REDUCED ORDER MODELS

10 THEORY AND NOTATION 65
10.1 Construction of the basis . . . 65

11 VMS-ROM 68
11.1 A word on error measurement . . . 70

12 THE ALGORITHM 71
12.1 FOM-FOM case . . . 71
12.2 ROM-ROM case . . . 71

V TESTING THE THEORY

13 NUMERICAL EXAMPLES 79
13.1 Cook's membrane . . . 79
13.2 Dynamic oscillation of a cantilever bar . . . 84

13.3 Flow around a cylinder with supported flag 92
13.4 Semi-stationary FSI flag 103
13.5 Flow injection into a channel with an elastic solid 112
13.6 3D Flow around a plate 122
13.7 3D Driven Cavity 132

SUMMARY 145

BIBLIOGRAPHY 153

A LINEARIZATION OF CERTAIN TERMS 167

ACRONYMS

F2F	Field to Field.
FE	Finite Element.
FOM	Full Order Model.
FSI	Fluid-Structure Interaction.
MOR	Model Order Reduction.
POD	Proper Orthogonal Decomposition.
RMSD	Root-Mean-Square Deviation.
ROM	Reduced Order Model.
VMS	Variational Multi-Scale.

INTRODUCTION

OBJECTIVES AND OUTLINE

This dissertation came about from the passion surrounding the beautiful but very complex topic that is Fluid-Structure Interaction (FSI) and the search for alternatives towards more efficient but precise solutions through the field of Reduced Order Models (ROMs). FSI is a topic that concerns us in every way in our daily life; for example through the way we produce the circuit boards of the computer you are probably reading this on [57], (unless you are one of the lucky few that got a physical copy!), the different types of engines that move our machinery [44, 77], the way our planes fly [52], the field of bio-medicine as we try to understand more of our physiology [81], or more specialized topics as Fluid-Structure-Fracture interaction for example, see [80]. Even though mathematically the description of the interaction of these systems can be simple (the physics involved is nothing more than the interaction of the different subsystems, in this case fluid and solid, which have been widely studied), numerically their solution is not. These systems produce ill conditioned matrices of great size due to many factors like different time integrators of each physics, elasticity of each medium and different spatial descriptions. In the end this translates into long solution times for solvers that are tailored to this very end. The applications described are just but a few ways, but of great importance, in which FSI can impact our daily life. It is of our own interest to have a more detailed understanding of these phenomena; the need of optimization in this field is evident.

Model Order Reduction (MOR) was originally developed for the area of system control theory, its main purpose being reducing its complexity

while maintaining the input-output behavior. The resulting mathematical approximation to the original full order problem is precisely known as a ROM. MOR rapidly spread to other fields of research quite successfully. Various ways to achieve model reduction and achieve solution speed up are available, see [6, 7, 36, 74]. Amongst the various families of reduced order models, Proper Orthogonal Decomposition (POD) –motivated by the ground breaking work detailed in [3, 59, 78] on the field of turbulence–, gained considerable attention in the area of numerical analysis, particularly in fluid dynamics because of its applicability to non linear partial differential equations. POD is the foundation of the ROM methods used in this work.

Optimization and model reduction, however, is not the only way in which we seek to find answers to the problems discussed above. We have also tried shifting our way of thinking regarding the coupling of the physics surrounding FSI by proving that different kind of couplings of the same set of physics is possible and can produce better results not only in the full order space but in the reduced one, we coined the term Field to Field (F2F) to refer to this kind of interaction coupling. Though the hope was never to produce a paradigm shift it was to start a conversation towards another way of looking at a problem that has been treated in the same way for decades.

The dissertation is organized as follows: In chapter 1 we review the Variational Multi-Scale Method and set the mathematical ground for the two sets of formulations developed in the rest of the dissertation; in part i we detail the development of three formulations for the description of non-linear solid elasto-dynamics; in part ii we review two Navier-Stokes equation models needed to complete our sets of F2F-FSI equations, shown in part iii alongside the coupling conditions and the general algorithm we follow to successfully run interaction examples. In part iv we detail our ROM model and set the theoretical background as well as how we couple it with FSI. Finally in part v we

show detailed study of various test cases ranging from the most simple benchmark cases to truly challenging interaction cases.

1 A VMS METHOD FOR AN ABSTRACT STATIONARY LINEAR PROBLEM

The Variational Multi-Scale (VMS) framework to approximate boundary value problems states that a variational problem can be described by two sets of sub-problems, one (the scale) that can be directly resolved as usual from the discretized mathematical domain or mesh, and a second one (the sub-scale) that deals with that smaller part of the solution that cannot be captured even by the finest mesh. The Galerkin Finite Element (FE) projection can be thought of as a special case of the VMS where the sub-scale is ignored. The main objective of the VMS method is to develop stabilized FE problems, this is problems that do not suffer from the same sources of instability as the Galerkin method.

Most of the problems found in this dissertation are unstable unless stringent requirements are met for the interpolating spaces of the variables in play (see, e.g., [31, 69] concerning the three-field solid problem discussed in chapter 4). In order to be able to use arbitrary interpolations, a stabilized FE method is required. Here we describe the VMS approach we follow, first for an abstract linear stationary problem. This summary is required to extend it to second order problems in time, a class of problems not considered previously.

1.1 SOME STANDARD NOTATION

Let us first introduce some standard notation that will be useful in the development of the VMS framework we apply but as well in the following sections to define the FE space for each particular domain. The space of

functions whose p power ($p \geqslant 1$) is integrable in a domain Ω is denoted by $L^p(\Omega)$, and the space of functions whose distributional derivatives of order up to $m \geqslant 0$ belong to $L^2(\Omega)$ by $H^m(\Omega)$. The L^2 inner product in Ω (for scalars, vectors or tensors) is denoted by $(\cdot,\cdot)$. The integral of the product of two functions defined in ω is $\langle\cdot,\cdot\rangle_\omega$, with the subscript omitted when $\omega = \Omega$; this definition includes the duality pairing. Given a Banach space X of time dependent functions, $L^p(0, t_f; X)$ denotes the space of functions whose norm in X is in $L^p(0, t_f)$, $p \geqslant 1$. Let $\mathcal{P}_h$ denote a finite element partition of a domain Ω. For the spatial discretization, the standard Galerkin finite element approximation that we will define for each domain will make use of the following notation and operators. Let an element domain be defined by $K \in \mathcal{P}_h$ with boundary ∂K and its diameter by h_K so that we can define the diameter of the finite element partition by $h = \max\{h_K | K \in \mathcal{P}_h\}$.

1.2 A GENERIC VARIATIONAL PROBLEM

By means of this notation now let us consider a generic bilinear form $B(y, z)$ and a linear form $L(z)$, where y is a vector of n unknowns and z is the vector of test functions of the problem $B(y, z) = L(z)$ for all z. Let Z be the functional space where the continuous problem is posed (for simplicity, the same for unknowns and test functions) and $Z_h \subset Z$ the FE approximation. As mentioned the idea of VMS methods is to split our unknowns into a FE part and a sub-grid scale (or simply sub-scale) that needs to be modelled [32, 48]. Thus, let $Z = Z_h \oplus \check{Z}$, where $\check{Z}$ is the complement of Z_h in Z. This split will cause associated splittings $y = y_h + \check{y}$ and $z = z_h + \check{z}$ and, due to the linearity of B, we can write the problem as:

$$B(y_h, z_h) + B(\check{y}, z_h) = L(z_h) \qquad \forall z_h \in Z_h, \tag{1.1a}$$

$$B(y_h, \check{z}) + B(\check{y}, \check{z}) = L(\check{z}) \qquad \forall \check{z} \in \check{Z}. \tag{1.1b}$$

1.3 ALGEBRAIC SUB-GRID SCALES

It is possible to express the generic form $B(y,z)$ as:

$$B(y,z) = \sum_K [\langle \mathcal{L}(y), z\rangle_K + \langle \mathcal{F}(y), z\rangle_{\partial K}] = \sum_K [\langle y, \mathcal{L}^* z\rangle_K + \langle y, \mathcal{F}^*(z)\rangle_{\partial K}], \quad (1.2a)$$

where $\mathcal{L}(\cdot)$ is now the linear operator of the problem being solved and $\mathcal{F}(\cdot)$ is the associated flux operator acting on the inter-elemental boundaries ∂K, whereas $\mathcal{L}^*$ and $\mathcal{F}^*$ are the corresponding formal adjoints (see [32] for details).
Using equation (1.2) we can avoid computing derivatives of the sub-scale in equation (1.1a) and write problem (1.1) as

$$B(y_h, z_h) + \sum_K [\langle \check{y}, \mathcal{L}^*(z_h)\rangle_K + \langle \check{y}, \mathcal{F}^*(z_h)\rangle_{\partial K}] = L(z_h) \qquad \forall z_h \in Z_h, \quad (1.3a)$$

$$\sum_K [\langle \check{z}, \mathcal{L}(\check{y}) + \mathcal{L}(y_h)\rangle_K + \langle \check{z}, \mathcal{F}(\check{y}) + \mathcal{F}(y_h)\rangle_{\partial K}] = L(\check{z}) \qquad \forall \check{z} \in \check{Z}. \quad (1.3b)$$

If we assume that the inter-elemental fluxes across the element are continuous, the second term on the LHS of equation equation (1.3b) vanishes. We can express this equation as:

$$\mathcal{L}(\check{y}) = \check{\Pi}(r), \quad (1.4)$$

in the space of sub-scales, where we have defined the residual $r = f - \mathcal{L}(y_h)$, $\mathcal{L}(y) = f$ is the linear equation being approximated and $\check{\Pi}$ is the projection onto the space of sub-grid scales.
Assuming that $\check{\Pi} = I$, one can now use different arguments (see [32]) to approximate the solution of equation (1.4) within each element K as

$$\check{y} = \tau_K r, \quad (1.5)$$

where τ_K is the matrix of stabilization parameters by which we model $\mathcal{L}(\check{y})$ and is problem dependent, the particular expression we use for the FSI problem is presented later.

For simplicity, in the following we shall omit the element boundary term in equation (1.3a), although it would be necessary if discontinuous pressure and stress interpolations are used (see [31]). Thus, the final problem is obtained inserting equation (1.5) in equation (1.3a); this problem is posed in terms of the FE unknown only.

1.4 DYNAMIC SUB-GRID SCALES FOR SECOND ORDER EQUATIONS IN TIME

Let us consider now the time evolution version of the previous linear problem, considering second order time derivatives, i.e., the problem to be solved is now

$$\partial_{tt}\mathbf{y} + \mathcal{L}(\mathbf{y}) = \mathbf{f},$$

with adequate initial and boundary conditions, where ∂_{tt} is the second derivative with respect to time t. In our particular FSI problem, we only have time derivatives for the displacement in the solid domain and for the velocities in the fluid domain; the final equations to be solved are described in parts i and ii respectively.
The time evolution counterpart of equation (1.3a), neglecting the element boundary term, is

$$(\partial_{tt}\mathbf{y}_h, \mathbf{z}_h) + \sum_K \langle \partial_{tt}\breve{\mathbf{y}}, \mathbf{z}_h\rangle_K + B(\mathbf{y}_h, \mathbf{z}_h) + \sum_K \langle \breve{\mathbf{y}}, \mathcal{L}^*(\mathbf{z}_h)\rangle_K = L(\mathbf{z}_h) \quad \forall \mathbf{z}_h \in Z_h, \tag{1.6}$$

whereas the counterpart of approximation (1.5) is

$$\partial_{tt}\breve{\mathbf{y}} + \boldsymbol{\tau}_K^{-1}\breve{\mathbf{y}} = \mathbf{r} - \partial_{tt}\mathbf{y}_h. \tag{1.7}$$

This equation is approximated using finite differences in time. Suppose that the finite difference scheme employed leads to the following approximation at time t^{n+1}:

$$\partial_{tt}\breve{\mathbf{y}}|_{t^{n+1}} \approx \frac{\gamma_1 \breve{\mathbf{y}}^{n+1}}{\delta t^2} - \frac{\breve{\mathbf{y}}^{\theta}}{\delta t^2}, \tag{1.8}$$

where $\breve{y}^{\theta}$ is the collection of terms belonging to the previous time steps in our time integration scheme and γ_1 is the coefficient multiplying the variable at step $n+1$ and δt is the time step. In this way, for a BDF2 scheme $\gamma_1 = 2$ and $\breve{y}^{\theta} = 5y^n - 4y^{n-1} + y^{n-1}$. Substituting equation (1.8) into equation (1.7) and regrouping all unknowns from the current time step $n+1$ on the LHS and all known terms of time step n into the right-hand-side (RHS) we obtain:

$$\frac{\gamma_1 \breve{y}^{n+1}}{\delta t^2} + \tau_K^{-1} \breve{y}^{n+1} = R^{n+1} + \frac{\breve{y}^{\theta}}{\delta t^2}, \tag{1.9}$$

where R^{n+1} includes all time discretized terms of the RHS of equation (1.7). Note that for problems with first order derivative in time the approach is the same taking care to use the correct BDF integrator and replacing δt^2 for δt. We thus have:

$$\breve{y}^{n+1} = \tau_t \left(R^{n+1} + \frac{\breve{y}^{\theta}}{\delta t^2} \right), \qquad \tau_t := \left(\frac{\gamma_1}{\delta t^2} I_n + \tau_K^{-1} \right)^{-1}, \tag{1.10}$$

where I_n is the $n \times n$ identity matrix. From equation (1.7) we also have that

$$\langle \partial_{tt} \breve{y}, z_h \rangle_K = \langle R - \tau_K^{-1} \breve{y}, z_h \rangle_K, \tag{1.11}$$

Then, after time discretization and substituting equation (1.10) into equation (1.11) we have:

$$\langle \partial_{tt} \breve{y}|_{t^{n+1}}, z_h \rangle_K \approx \langle (I_n - \tau_K^{-1} \tau_t) R^{n+1}, z_h \rangle_K - \left\langle \tau_K^{-1} \tau_t \frac{\breve{y}^{\theta}}{\delta t^2}, z_h \right\rangle_K. \tag{1.12}$$

The final time discrete problem for the FE unknown y_h^{n+1} is obtained by replacing equation (1.12) and equation (1.10) into the time discrete form of equation (1.6). Note that both in equation (1.12) and in equation (1.10) we need $\breve{y}^{\theta}$, i.e., the sub-scales of previous time steps need to be stored at the numerical integration points. They will act as internal variables in a solid mechanics problem.

The idea presented is the same as for first order problems in time (see [34]), the main difference being that now the sub-scales need to be

stored in more previous time steps to allow computing an approximation to the second derivative. Even though it is not our purpose in this dissertation to study dynamic sub-scales for second order problems in detail, we have found them crucial to improve the behavior of iterative schemes. In particular, most of the FSI cases shown later do not converge without the use of dynamic sub-grid scales, their effect has been found critical.

1.5 ORTHOGONAL SUB-GRID SCALES

Recalling that section 1.3 states the generic form of a stabilized problem we can modify it assuming the sub-scale lives in a space which is orthogonal to the FE space; using dynamic sub-scales we can write:

$$\left(\rho\frac{\gamma_1 \mathbf{y}_h}{\delta t^2}, \mathbf{z}_h\right) + B(\mathbf{y}_h, \mathbf{z}_h) - \left(\Pi^{\perp}(\mathcal{L}(\mathbf{y}_h)), \boldsymbol{\tau}_t \mathcal{L}^*(\mathbf{z}_h)\right) = \left(\mathbf{f} + \rho\frac{\mathbf{y}_h^{\theta}}{\delta t^2}, \mathbf{z}_h\right) - \left(\rho\frac{\check{\mathbf{y}}^{\theta}}{\delta t^2}, \boldsymbol{\tau}_t \mathcal{L}^*(\mathbf{z}_h)\right) \quad \forall\, \mathbf{z}_h, \tag{1.13}$$

where now $\Pi^{\perp} = I - \Pi_h$, I being the identity operator and Π_h the L^2 projection onto the FE space.

For the sake of clarity we assume that all terms are evaluated at time instant $n+1$, except the ones clearly specified, and $\Pi^{\perp}(\mathbf{f}) = 0$, since the external forces either belong to the FE space or are approximated by elements in it, $\Pi^{\perp}(\rho\partial_{tt}\mathbf{y}_h) = 0$ since $\partial_{tt}\mathbf{y}_h$ is a FE function, and $(\rho\partial_{tt}\mathbf{y}_h, \check{\mathbf{z}}) = 0$ since these terms are mutually orthogonal. For more details on the orthogonal sub-scales see [30].

Part I

SOLID ELASTO-DYNAMICS

NON-LINEAR SOLID ELASTO-DYNAMICS

In the study of Finite Elements (FEs) generally one of the first applied instances of the method to the real world can be found through study of linear solid elasticity. This is because the mathematics involved are fairly straightforward and the assembly of the discrete operators easy. The jump to geometric non-linearity increases in complexity but in any case retains that characteristic simplicity of displacement based solid models. All this to say that there is ample bibliography and textbooks detailing the approach to linearity and displacement based non-linearity. However in the field of mixed methods bibliography is far less available, in this regard we give context to our work in the following lines.

The term 'mixed methods' in mechanics is generally applied to a formulation that approximates separately different variables, for example stress and displacement fields. In our case we apply the term to deal with the splitting of the stress tensor into its corresponding deviatoric and spherical parts, leading to a displacement–stress–pressure formulation approximated by the finite element (FE) method. This kind of stress splitting techniques are by no means new and have been shown to work properly for both solid mechanics and fluid dynamics. In [31] it was shown that it is possible to approximate successfully the Stokes problem by means of a three-field splitting and a stabilization of the Galerkin formulation using a Variational Multi-Scale (VMS) approach, in particular assuming that the sub-grid scales of the model belong to a space orthogonal to the space of the FE scale. Later, [27] applied this same three-field splitting technique to a linear solid mechanics setting, comparing it with a displacement–pressure

splitting. This is the basis of our work in terms of solid mechanics; however there are other types of approximations to the elastic problem, for example [76] explores a velocity–stress splitting that proves to be convenient and robust for time evolution settings. The assumptions and approximations made to develop stress–displacement and strain–displacement formulations are detailed in [25] and applied in [24] to approximate compressible and incompressible plasticity by means of a VMS method, producing a method with enhanced stability and convergence properties in comparison to the displacement based –or irreducible– formulation. In the context of geometrically nonlinear solid mechanics, a formulation accounting for the incompressible limit using a total Lagrangian approach is proposed in [19]; however we use a more common updated Lagrangian approach for modeling our solid domain.

2 IRREDUCIBLE SOLID EQUATIONS

In this chapter, a short review of the non-linear solid elasto-dynamics formulation we employ is given, as well as the spatial and temporal discretization schemes used.

2.1 GOVERNING EQUATIONS

Let Ω_{sl} be the domain of the solid, with boundary $\Gamma_{sl} = \Gamma_{sl,D} \cup \Gamma_{sl,N}$, where $\Gamma_{sl,D}$ and $\Gamma_{sl,N}$ are boundaries where Dirichlet and Neumann conditions are prescribed, respectively. The elasto-dynamics problem written in updated Lagrangian form (see for example [14]) consists in finding a displacement field $\mathbf{d} : \Omega_{sl} \times]0, t_f[\longrightarrow \mathbb{R}^d$ for a time interval of analysis $]0, t_f[$, such that:

$$\begin{aligned}
\rho_{sl}\partial_{tt}\mathbf{d} - \nabla \cdot \boldsymbol{\sigma}_{sl} &= \rho_{sl}\mathbf{f} && \text{in } \Omega_{sl}, \\
\mathbf{d} &= \mathbf{d}_D && \text{on } \Gamma_{sl,D}, \\
\mathbf{n}_{sl} \cdot \boldsymbol{\sigma}_{sl} &= \mathbf{t}_{sl} && \text{on } \Gamma_{sl,N}, \\
\partial_t \mathbf{d} &= \dot{\mathbf{d}}^0 && \text{in } \Omega_{sl}, \quad t = 0, \\
\mathbf{d} &= \mathbf{d}^0 && \text{in } \Omega_{sl}, \quad t = 0,
\end{aligned} \tag{2.1}$$

in $t \in]0, t_f[$, where ρ_{sl} is the solid's density, $\boldsymbol{\sigma}_{sl}$ is the solid's Cauchy stress tensor, $\mathbf{f}$ is the acceleration vector of the solid (now defined on Ω_{sl}), $\mathbf{d}^0$ is a prescribed initial displacement and $\dot{\mathbf{d}}^0$ is a prescribed initial velocity, $\mathbf{d}_D$ is a prescribed displacement on the boundary $\Gamma_{sl,D}$, $\mathbf{t}_{sl}$ is a prescribed traction on the boundary $\Gamma_{sl,N}$, and $\mathbf{n}_{sl}$ is the normal to the solid domain.

In the non-linear setting, the constitutive equation for the stress tensor can be modeled in a variety of ways and depends on the material to be

simulated. In the present case we are interested in the Neo-Hookean and Saint Venant-Kirchoff material models, which can be defined as follows:

$$\text{NeoHookean: } \boldsymbol{\sigma}_{sl} = \frac{1}{J}\left[\lambda_{sl}\ln(J)\mathbf{I} + \mu_{sl}(\mathbf{b} - \mathbf{I})\right],$$
$$\text{Saint Venant-Kirchoff: } \boldsymbol{\sigma}_{sl} = \frac{1}{J}\mathbf{F}\left[\lambda_{sl}\mathrm{tr}(\mathbf{E})\mathbf{I} + 2\mu_{sl}\mathbf{E}\right]\mathbf{F}^{T},$$

where $\mathbf{F} = \frac{\partial \mathbf{x}}{\partial \mathbf{X}}$ is the deformation gradient, $J = \det(\mathbf{F})$, λ_{sl} and μ_{sl} are Lamé's parameters, $\mathbf{b} = \mathbf{F}\mathbf{F}^{T}$ is the left Cauchy tensor, $\mathbf{I}$ is the identity tensor and $\mathbf{E}$ is the Green-Lagrange strain tensor.

2.2 WEAK FORM

By means of the notation defined in section 1.1 let $\mathcal{E}_0 = \{\boldsymbol{e} \in H^1(\Omega_{sl})^d \mid \boldsymbol{e}|_{\Gamma_D} = \mathbf{0}\}$ and $\mathcal{E}_D \subset \{\boldsymbol{e} \in H^1(\Omega_{sl})^d \mid \boldsymbol{e}|_{\Gamma_D} = \mathbf{d}_D\}$ be the appropriate spaces where the test functions and the displacement field (for $t \in]0, t_f[$) should belong, respectively. The weak form of the solid elastodynamics problem consists in finding $\mathbf{d}$ in an adequate subspace of $L^2(0, t_f; \mathcal{E}_D)$ such that:

$$\begin{aligned}
(\rho_{sl}\partial_{tt}\mathbf{d}, \boldsymbol{e}) - (\boldsymbol{\sigma}_{sl}, \nabla^s \boldsymbol{e}) &= \langle \rho_{sl}\mathbf{f}, \boldsymbol{e}\rangle + \langle \mathbf{t}_{sl}, \boldsymbol{e}\rangle_{\Gamma_{N,sl}}, && t \in]0, t_f[, \\
(\partial_t \mathbf{d}, \boldsymbol{e}) &= (\dot{\mathbf{d}}^0, \boldsymbol{e}), && t = 0, \\
(\mathbf{d}, \boldsymbol{e}) &= (\mathbf{d}^0, \boldsymbol{e}), && t = 0,
\end{aligned} \tag{2.2}$$

for all $\boldsymbol{e} \in \mathcal{E}_0$.

2.3 SPATIAL DISCRETIZATION

We can now construct conforming finite element spaces $\mathcal{E}_{h,D} \subset \mathcal{E}_D$ and $\mathcal{E}_{h,0} \subset \mathcal{E}_0$. Then, the Galerkin finite element approximation can be written as finding $\mathbf{d}_h$ in $L^2(0, t_f; \mathcal{E}_{h,D})$ such that:

$$(\rho_{sl}\partial_{tt}\mathbf{d}_h, \boldsymbol{e}_h) - (\boldsymbol{\sigma}_{sl,h}, \nabla^s \boldsymbol{e}_h) = \langle \rho_{sl}\mathbf{f}, \boldsymbol{e}_h\rangle + \langle \mathbf{t}_{sl}, \boldsymbol{e}_h\rangle_{\Gamma_{sl,N}}, \qquad t \in]0, t_f[, \tag{2.3}$$

$$(\partial_t \mathbf{d}_h, \mathbf{e}_h) = (\dot{\mathbf{d}}^0, \mathbf{e}_h), \qquad t = 0,$$
$$(\mathbf{d}_h, \mathbf{e}_h) = (\mathbf{d}^0, \mathbf{e}_h), \qquad t = 0,$$

for all $\mathbf{e}_h \in \mathcal{E}_{h,0}$, where $\sigma_{sl,h}$ is the Cauchy stress tensor evaluated with $\mathbf{d}_h$. This problem can be linearized using a Newton-Raphson scheme; for further details see for example [14].

2.4 TIME DISCRETIZATION

Even though any finite difference scheme in time could be used, including the popular Newmark scheme, the following second order Backward Differences scheme (BDF2) has been used for the temporal discretization:

$$\mathbf{a}^{n+1} = \frac{1}{(\delta t)^2}\left(2\mathbf{d}^{n+1} - 5\mathbf{d}^n + 4\mathbf{d}^{n-1} - \mathbf{d}^{n-2}\right),$$

where δt is the time delta and $\mathbf{d}^{n+1}$ and $\mathbf{a}^{n+1}$ are approximations to the position and acceleration vectors at time step $n+1$, respectively.

3 TWO FIELD SOLID EQUATIONS

In this chapter we present the two-field elasto-dynamic solid equations, their manipulation to obtain the governing equations and the way we approximate them using our VMS formulation, the main features being the use of orthogonal and dynamic sub-scales arising from the VMS concept. Such a formulation for finite strain elasticity in an updated Lagrangian framework is developed here for the first time.

Recalling from section 2.1 that the dynamic conservation of momentum equation for the solid problem can be written as:

$$\rho_{sl}\partial_{tt}d_i - \partial_j\sigma_{ij} = \rho_{sl}f_{sl,i} \quad \text{in } \Omega_s,\ t \in]0, t_f[, \tag{3.1}$$

where Ω_{sl} is the domain of $\mathbb{R}^{n_d}$ defined by the movement of the solid during the time interval $[0, t_f]$, $n_d = 2$ or 3 is the number of space dimensions, ∂_t denotes the partial time derivative (and thus ∂_{tt} is the second derivative with respect to time), and ∂_i the derivative with respect to the ith Cartesian coordinate x_i, $i = 1, \ldots, n_d$. The unknowns for this problem are the displacement field and the Cauchy stress tensor, with Cartesian components d_i and σ_{ij}, respectively, $i, j = 1, \ldots, n_d$. In this work vectors and tensors are assumed to be represented by their Cartesian components. In particular, $f_{sl,i}$ is the vector of external forces acting on the solid, its density being ρ_{sl}. Finally, in Eq. (3.1) and below repeated indexes imply summation over the number of space dimensions.

Eq. (3.1) will be expressed in an updated Lagrangian reference system for which the stress tensor has to be given in spatial form, this is, in terms of the Cauchy stress σ_{ij}. If the expression of the stress is defined

in terms of the displacement and inserted into Eq. (3.1), we will call *irreducible* the resulting problem posed for d_i alone. If the stress is expressed in terms of the pressure p_{sl} and the displacements, we will call this a two-field formulation. Initial and boundary conditions have to be appended to this equation.

3.1 SPLIT OF THE STRESS TENSOR AND FIELD EQUATIONS

We can define the pressure and the deviatoric stress of the stress tensor in the following way:

$$p_{sl} = \frac{1}{n_d}\sigma_{kk}, \tag{3.2a}$$

$$s_{sl,ij} = \sigma_{ij} - p_{sl}\delta_{ij}, \tag{3.2b}$$

where δ_{ij} is Kronecker's delta. If we assume the material model to be Neo-Hookean, the stress tensor is given by:

$$\sigma_{ij} = \frac{1}{J}\left[(\lambda \ln(J) - \mu_{sl})\delta_{ij} + \mu_{sl} b_{ij}\right], \tag{3.3}$$

where J is the determinant of the displacement gradient F_{iJ}, λ and μ_{sl} are Lame's parameters, b_{ij} is the left Cauchy tensor and b_{ii} its trace. These are defined as follows:

$$J = \det(F_{iJ}), \quad F_{iJ} = \frac{\partial x_i}{\partial X_J}, \quad b_{ij} = F_{iK}F_{jK}, \tag{3.4}$$

where x_i are the coordinates defined in the spatial frame of reference and X_I are the coordinates defined in the material frame of reference. Throughout this work, lower case letters will refer to the spatial configuration, whereas upper case letters will refer to the material one. Eq. (3.2a) can be expressed as:

$$p_{sl} = \frac{1}{J}\left[(\lambda \ln(J) - \mu_{sl}) + \frac{\mu_{sl}\, b_{ll}}{n_d}\right], \tag{3.5}$$

and the deviatoric part, Eq. (3.2b), as:

$$s_{sl,ij} = \frac{\mu_{sl}}{J}\left(b_{ij} - \frac{b_{ll}}{n_d}\delta_{ij}\right). \tag{3.6}$$

Finally, by replacing Eq. (3.6) into our momentum equation we can write the resulting system of equations as an alternative to Eq. (3.1) as:

$$\rho_{sl}\partial_{tt}d_i - \partial_j\left[\frac{\mu_{sl}}{J}\left(b_{ij} - \frac{b_{ll}}{n_d}\delta_{ij}\right)\right] - \partial_i p_{sl} = \rho_{sl} f_{sl,i}, \tag{3.7a}$$

$$\frac{J}{\lambda}p_{sl} = \ln(J) + \frac{\mu_{sl}}{\lambda}\left(\frac{b_{ll}}{n_d} - 1\right), \tag{3.7b}$$

where b_{ij} is expressed in terms of the displacements d_i and the density evolves as

$$\rho_{sl} = J\rho_{sl,0},$$

where $\rho_{sl,0}$ is the density in the initial configuration. This is the two-field form of the solid mechanics equations we shall consider, the unknowns being d_i and p_{sl}. We shall write these unknowns as $\mathbf{y}_{sl} = [\mathbf{d}, p_{sl}]$, and denote by $\mathcal{A}(\mathbf{y}_{sl})$ the spatial nonlinear operator associated to Eqs. (3.7), so that these equations can be written as

$$\mathcal{M}\partial_{tt}\mathbf{y}_{sl} + \mathcal{A}(\mathbf{y}_{sl}) = \mathbf{F}_{sl}, \tag{3.8}$$

where $\mathcal{M} := \mathrm{diag}[\rho_{sl}\mathbf{I}_{n_d}, 0]$, $\mathbf{I}_{n_d}$ being the identity on vectors and $\mathbf{F}_{sl} := [\rho_{sl}\mathbf{f}_{sl}, 0]$.

3.2 LINEARIZATION

In order to approximate a solution to this highly non-linear problem we can re-write it by approximating our variables $\mathbf{y}_{sl} = [\mathbf{d}, p_{sl}]$ in terms of their increment $\delta\mathbf{y}_{sl} = [\delta\mathbf{d}, \delta p_{sl}]$ in the following form:

$$\mathbf{y}_{sl} = \tilde{\mathbf{y}}_{sl} + \delta\mathbf{y}_{sl}, \tag{3.9}$$

where $\tilde{\mathbf{y}}_{sl} = [\tilde{\mathbf{d}}, \tilde{p}_{sl}]$ is the vector consisting of previously known values of $\mathbf{y}_{sl}$. The Newton-Raphson linearization is obtained inserting this

split in the equations to be solved and neglecting quadratic terms of the increments. Denoting with $\tilde{\cdot}$ the functions computed with $\tilde{\mathbf{y}}_{sl}$, Eqs. (3.7) can be re-written as (the linearization of these terms is shown in appendix A):

$$\begin{aligned}\rho_{sl}\partial_{tt}\delta d_i - \partial_j\left[\frac{\mu_{sl}}{\tilde{J}}\left(\frac{\partial\delta d_i}{\partial X_K}\tilde{F}_{jK}+\tilde{F}_{iK}\frac{\partial\delta d_j}{\partial X_K}\right)\right]+2\frac{\delta_{ij}}{n_d}\partial_j\left(\frac{\mu_{sl}}{\tilde{J}}\tilde{F}_{lK}\frac{\partial\delta d_l}{\partial X_K}\right)\\ +\partial_j\left[\frac{\mu_{sl}}{\tilde{J}}\left(\tilde{F}^{-1}_{Kl}\frac{\partial\delta d_l}{\partial X_K}\right)\left(\tilde{b}_{ij}-\frac{\tilde{b}_{ll}}{n_d}\delta_{ij}\right)\right]-\partial_i\delta p_{sl}\\ =\rho_{sl}f_{sl,i}+\partial_j\left[\frac{\mu_{sl}}{\tilde{J}}\left(\tilde{b}_{ij}-\frac{\tilde{b}_{ll}}{n_d}\delta_{ij}\right)\right]+\partial_i\tilde{p}_{sl}-\rho_{sl}\partial_{tt}\tilde{d}_i,\end{aligned}\tag{3.10a}$$

$$\frac{\tilde{J}}{\lambda}\delta p_{sl}+\left[\left(\frac{\tilde{J}\tilde{p}_{sl}}{\lambda}-1\right)\tilde{F}^{-1}_{Kl}-\frac{2\mu_{sl}}{\lambda n_d}\tilde{F}_{lK}\right]\frac{\partial\delta d_l}{\partial X_K}=-\frac{\tilde{J}}{\lambda}\tilde{p}_{sl}+\ln(\tilde{J})+\frac{\mu_{sl}}{\lambda}\left(\frac{\tilde{b}_{ii}}{n_d}-1\right).\tag{3.10b}$$

Let us denote by $\mathcal{L}_{sl}(\tilde{\mathbf{y}}_{sl};\delta\mathbf{y}_{sl})$ the spatial linear operator on $\delta\mathbf{y}_{sl}$, for given $\tilde{\mathbf{y}}_{sl}$, appearing in the left-hand-side (LHS) of these equations. Using the notation in Eq. (3.8), we may write

$$\mathcal{M}\partial_{tt}\delta\mathbf{y}_{sl}+\mathcal{L}_{sl}(\tilde{\mathbf{y}}_{sl};\delta\mathbf{y}_{sl})=\mathbf{F}_{sl}-\mathcal{M}\partial_{tt}\tilde{\mathbf{y}}_{sl}-\mathcal{A}(\tilde{\mathbf{y}}_{sl}).\tag{3.11}$$

In this way, upon convergence $\delta\mathbf{y}_{sl}\approx 0$ and $\tilde{\mathbf{y}}_{sl}$ is the solution of Eq. (3.8).

3.3 INITIAL AND BOUNDARY-VALUE PROBLEM

The problem to be solved consists in finding $\mathbf{y}_{sl}:\Omega_{sl}\times]0,t_f[\longrightarrow\mathbb{R}^{n_d}\times\mathbb{R}$ as the solution to Eq. (3.8) and such that

$$\begin{aligned}&d_i=d_{i,D} && \text{on } \Gamma_{sl,D},\quad t\in]0,t_f[,\\ &n_{sl,j}\sigma_{ij}=t_{sl,i} && \text{on } \Gamma_{sl,N},\quad t\in]0,t_f[,\\ &d_i=d_i^0 && \text{in } \Omega_{sl},\quad t=0,\\ &\dot{d}_i=\dot{d}_i^0 && \text{in } \Omega_{sl},\quad t=0,\end{aligned}$$

where all variables have been defined previously in section 2.1.

3.4 WEAK FORM

Let Y_{sl} be the space of functions where $\mathbf{y}_{sl}$ must belong for each time t; functions in Y_{sl} satisfy the Dirichlet boundary conditions. Let also $Y_{sl,0}$ be the space of functions with the same regularity as Y_{sl} but satisfying the homogeneous counterpart of the Dirichlet boundary conditions. The weak form of the two-field elasto-dynamic solid equations consists in finding $[\mathbf{d}, p_{sl}] : [0, t_f] \longrightarrow Y_{sl}$ such that

$$
\begin{aligned}
&(e_i, \rho_{sl}\partial_{tt}\delta d_i) + \left(\frac{\partial e_i}{\partial x_j}, \frac{\mu_{sl}}{\tilde{J}}\left(\frac{\partial \delta d_i}{\partial X_K}\tilde{F}_{jK} + \tilde{F}_{iK}\frac{\partial \delta d_j}{\partial X_K}\right)\right) \\
&\quad - \left(\frac{\partial e_i}{\partial x_i}, 2\frac{\mu_{sl}}{\tilde{J}n_d}\tilde{F}_{lK}\frac{\partial \delta d_l}{\partial X_K}\right) - \left(\frac{\partial e_i}{\partial x_j}, \frac{\mu_{sl}}{\tilde{J}}\left(\tilde{F}^{-1}_{Kl}\frac{\partial \delta d_l}{\partial X_K}\right)\left(\tilde{b}_{ij} - \frac{\tilde{b}_{ll}}{n_d}\delta_{ij}\right)\right) \\
&\quad + \left(\frac{\partial e_i}{\partial x_i}, \delta p_{sl}\right) = (e_i, \rho_{sl} f_{sl,i}) + (e_i, t_i)_{\Gamma_{sl,N}} - (\rho_{sl}\partial_{tt}\tilde{d}_i, e_i) \\
&\qquad - \left(\frac{\partial e_i}{\partial x_j}, \frac{\mu_{sl}}{\tilde{J}}\left(\tilde{b}_{ij} - \frac{\tilde{b}_{ll}}{n_d}\delta_{ij}\right)\right) - \left(\frac{\partial e_i}{\partial x_i}, \tilde{p}_{sl}\right), \qquad (3.12a) \\
&\left(q_{sl}, \frac{\tilde{J}}{\lambda}\delta p_{sl}\right) + \left(q_{sl}, \left[\left(\frac{\tilde{J}\tilde{p}_{sl}}{\lambda} - 1\right)\tilde{F}^{-1}_{Kl} - \frac{2\mu_{sl}}{\lambda n_d}\tilde{F}_{lK}\right]\frac{\partial \delta d_l}{\partial X_K}\right) \\
&\quad = \left(q_{sl}, -\frac{\tilde{J}}{\lambda}\tilde{p}_{sl} + \ln(\tilde{J}) + \frac{\mu_{sl}}{\lambda}\left(\frac{\tilde{b}_{ii}}{n_d} - 1\right)\right), \qquad (3.12b)
\end{aligned}
$$

for all $z_{sl} = [e, q_{sl}] \in Y_{sl,0},\ t \in]0, t_f[$, and satisfying initial conditions in a weak sense.

Let us define the form B_{sl} as:

$$
\begin{aligned}
B_{sl}(\tilde{\mathbf{y}}_{sl}; \delta\mathbf{y}_{sl}, z_{sl}) &= \left(\frac{\partial e_i}{\partial x_j}, \frac{\mu_{sl}}{\tilde{J}}\left(\frac{\partial \delta d_i}{\partial X_K}\tilde{F}_{jK} + \tilde{F}_{iK}\frac{\partial \delta d_j}{\partial X_K}\right)\right) - \left(\frac{\partial e_i}{\partial x_i}, 2\frac{\mu_{sl}}{\tilde{J}n_d}\tilde{F}_{lK}\frac{\partial \delta d_l}{\partial X_K}\right) \\
&\quad - \left(\frac{\partial e_i}{\partial x_j}, \frac{\mu_{sl}}{\tilde{J}}\left(\tilde{F}^{-1}_{Kl}\frac{\partial \delta d_l}{\partial X_K}\right)\left(\tilde{b}_{ij} - \frac{\tilde{b}_{ll}}{n_d}\delta_{ij}\right)\right) + \left(\frac{\partial e_i}{\partial x_i}, \delta p_{sl}\right) + \left(q_{sl}, \frac{\tilde{J}}{\lambda}\delta p_{sl}\right) \\
&\quad + \left(q_{sl}, \left[\left(\frac{\tilde{J}\tilde{p}_{sl}}{\lambda} - 1\right)\tilde{F}^{-1}_{Kl} - \frac{2\mu_{sl}}{\lambda n_d}\tilde{F}_{lK}\right]\frac{\partial \delta d_l}{\partial X_K}\right), \qquad (3.13)
\end{aligned}
$$

and a form

$$
\begin{aligned}
L_{sl}(\tilde{\mathbf{y}}_{sl}; z_{sl}) &= (e_i, \rho_{sl} f_{sl,i}) + (e_i, t_i)_{\Gamma_{sl,N}} - \left(\frac{\partial e_i}{\partial x_j}, \frac{\mu_{sl}}{\tilde{J}}\left(\tilde{b}_{ij} - \frac{\tilde{b}_{ll}}{n_d}\delta_{ij}\right)\right) \\
&\quad - \left(\frac{\partial e_i}{\partial x_i}, \tilde{p}_{sl}\right) + \left(q_{sl}, -\frac{\tilde{J}}{\lambda}\tilde{p}_{sl} + \ln(\tilde{J}) + \frac{\mu_{sl}}{\lambda}\left(\frac{\tilde{b}_{ii}}{n_d} - 1\right)\right), \qquad (3.14)
\end{aligned}
$$

which enable us to write Eqs. (3.12) in the following simplified form:

$$
(\rho_{sl}\partial_{tt}\delta d_i, e_i) + B_{sl}(\tilde{\mathbf{y}}_{sl}; \delta\mathbf{y}_{sl}, z_{sl}) = L_{sl}(\tilde{\mathbf{y}}_{sl}; z_{sl}) - (\rho_{sl}\partial_{tt}\tilde{d}_i, e_i), \qquad (3.15)
$$

for all test functions $z_{sl} = [e, q_{sl}] \in Y_{sl,0}$. Initial conditions have to added to this variational equation.

3.5 GALERKIN SPATIAL DISCRETIZATION

By means of the notation defined on section 1.1 we can construct the approximating space for the unknown and the test functions, $Y_{sl,h}$ and $Y_{sl,h,0}$, respectively, in the usual manner. We consider here conforming approximations.
The Galerkin FE approximation to the problem can be written as: find $y_{sl,h} = [d_h, p_{sl,h}] : [0, t_f] \longrightarrow Y_{sl,h}$ such that

$$(\rho_{sl}\partial_{tt}\delta d_h, e_h) + B_{sl}(\tilde{y}_{sl,h}; \delta y_{sl,h}, z_{sl,h}) = L_{sl,h}(\tilde{y}_{sl}; z_{sl,h}) - (\rho_{sl}\partial_{tt}\tilde{d}_h, e_h), \tag{3.16}$$

in $]0, t_f[$ for all $z_{sl,h} \in Y_{sl,h,0}$, and satisfying the initial conditions weakly. Considering the problem discretized in time, at each time step the problem to be solved until convergence is

$$(\rho_{sl}\delta a_h^{n+1}, e_h) + B_{sl}(\tilde{y}_{sl,h}^{n+1}; \delta y_{sl,h}^{n+1}, z_{sl,h}) = L_{sl,h}(\tilde{y}_{sl,h}^{n+1}; z_{sl,h}) - (\rho_{sl}\tilde{a}_h^{n+1}, e_h), \tag{3.17}$$

for $n = 1, 2, \ldots$ and for all $z_{sl,h} \in Y_{sl,h,0}$, d_h^0 and d_h^1 being given by the initial conditions and a^2 properly initialized (for example using a first order BDF scheme).
The time discretization used is the same as defined in section 2.4.

3.6 STABILIZATION OF THE NON-LINEAR TWO-FIELD SOLID PROBLEM

Following the developments from chapter 1, we can express in particular the forms and operators for our stabilized two-field solid problem. If we consider the splitting of the unknowns in the FE components and the sub-scales, instead of Eq. (3.17) we obtain:

$$(\rho_{sl}\delta a_h, e_h) + B_{sl}(\tilde{y}_{sl}; \delta y_{sl}, [e_h, 0])$$

$$
\begin{aligned}
&+\left(\frac{\partial e_{h,i}}{\partial x_j},\frac{\mu_{sl}}{\tilde{J}}\left(\frac{\partial \breve{d}_i}{\partial X_K}\tilde{F}_{jK}+\tilde{F}_{iK}\frac{\partial \breve{d}_j}{\partial X_K}\right)\right)\\
&-\left(\frac{\partial e_{h,i}}{\partial x_i},2\frac{\mu_{sl}}{\tilde{J}n_d}\tilde{F}_{lK}\frac{\partial \breve{d}_l}{\partial X_K}\right)-\left(\frac{\partial e_{h,i}}{\partial x_j},\frac{\mu_{sl}}{\tilde{J}}\left(\tilde{F}^{-1}_{Kl}\frac{\partial \breve{d}_l}{\partial X_K}\right)\left(\tilde{b}_{ij}-\frac{\tilde{b}_{ll}}{n_d}\delta_{ij}\right)\right)\\
&+\left(\frac{\partial e_{h,i}}{\partial x_i},\breve{p}_{sl}\right)=L_{sl}(\tilde{\mathfrak{y}}_{sl};[e_h,0])-(\rho_{sl}\tilde{a}_h,e_h) \qquad (3.18a)\\
&B_{sl}(\tilde{\mathfrak{y}}_{sl};\delta\mathfrak{y}_{sl},[0,q_{sl,h}])+\left(q_h,\frac{\tilde{J}}{\lambda}\breve{p}_{sl}\right)+\left(q_h,\left[\left(\frac{\tilde{J}\breve{p}_{sl,h}}{\lambda}-1\right)\tilde{F}^{-1}_{Kl}-\frac{2\mu_{sl}}{\lambda n_d}\tilde{F}_{lK}\right]\frac{\partial \breve{d}_l}{\partial X_K}\right)\\
&=L_{sl}(\tilde{\mathfrak{y}}_{sl};[0,q_{sl,h}]), \qquad (3.18b)
\end{aligned}
$$

where the sub-scale at the current time step is $\breve{\mathfrak{y}}_{sl}=[\breve{d},\breve{p}_{sl}]$. In these equations it is understood that all terms are evaluated at t^{n+1}, like previously, the variables with a tilde being guesses to the unknowns (from a past iteration step, for example).

This version of the problem is unfeasible as it deals with derivatives of the sub-scales for which we do not have an approximation. These terms are integrated by parts and derivatives transferred to the test functions. The stabilization terms can then be written as:

$$
\sum_K(\breve{\mathfrak{y}}_{sl,h},\mathcal{L}^*_{sl}(\tilde{\mathfrak{y}}_{sl};z_{sl,h}))_K+\sum_K(\breve{\mathfrak{y}}_{sl},\mathcal{F}^*_{sl}(\tilde{\mathfrak{y}}_{sl};z_{sl,h}))_{\partial K}\,. \qquad (3.19)
$$

We shall neglect the second term, although this approximation can be relaxed (see [33]) and, in fact, is needed if the pressure interpolation space is discontinuous. Concerning the first term, operator $\mathcal{L}^*_{sl}(\tilde{\mathfrak{y}}_{sl};z_{sl,h})$ has two components:

$$
\mathcal{L}^*_{sl}(\tilde{\mathfrak{y}}_{sl};z_{sl,h})=[\mathcal{L}^*_{sl,1}(\tilde{\mathfrak{y}}_{sl};z_{sl,h}),\mathcal{L}^*_{sl,2}(\tilde{\mathfrak{y}}_{sl};z_{sl,h})]^T,
$$

the first being a vector and the second a scalar, given by:

$$
\begin{aligned}
\mathcal{L}^*_1(\tilde{\mathfrak{y}}_{sl};z_{sl,h})=&-\frac{1}{2\tilde{J}}\left[\frac{\partial}{\partial X_K}\left(\frac{\partial e_{h,i}}{\partial x_j}\tilde{F}_{jK}\right)+\frac{\partial}{\partial X_K}\left(\frac{\partial e_{h,j}}{\partial x_i}\tilde{F}_{jK}\right)\right]+\frac{1}{n_d\tilde{J}}\frac{\partial}{\partial X_K}\left(\frac{\partial e_{h,l}}{\partial x_l}\tilde{F}_{iK}\right)\\
&-\frac{1}{2\tilde{J}}\left(\frac{\partial}{\partial X_K}\left(\frac{\partial e_{h,l}}{\partial x_j}\left(\tilde{b}_{lj}-\frac{\tilde{b}_{nn}}{n_d}\delta_{ij}\right)\tilde{F}^{-1}_{Ki}\right)\right)\\
&-\frac{\partial}{\partial X_K}\left(\left(\frac{\tilde{J}\breve{p}_{sl,h}}{\lambda}-1\right)q_h\tilde{F}^{-1}_{Ki}\right)+\left(\frac{2\mu_{sl}}{\lambda n_d}\frac{\partial}{\partial X_K}(q_h\tilde{F}_{iK})\right), \qquad (3.20a)\\
\mathcal{L}^*_2(\tilde{\mathfrak{y}}_{sl};z_{sl,h})=&\frac{\partial e_{h,i}}{\partial x_i}+\frac{\tilde{J}}{\lambda}q_{sl}. \qquad (3.20b)
\end{aligned}
$$

To obtain the final expression of the stabilized problem, we need the expression of the sub-scales to be introduced in Eq. (3.19). For that, we just have to apply the general expressions obtained in the previous chapter, taking into account that we only have time derivatives of the displacements.

Using the same arguments as in [31], we will take the matrix of stabilization parameters within each element K as

$$\boldsymbol{\tau}_{sl,K} = \text{diag}\,[\tau_{sl,1,K}\mathbf{I}_{n_d}, \tau_{sl,2}]\,, \tag{3.21}$$

$$\tau_{sl,1,K} := \left(c_{sl,1}\frac{\mu_{sl}}{h_K^2}\right)^{-1}, \quad \tau_{sl,2} := c_{sl,2}2\mu_{sl}, \tag{3.22}$$

where $c_{sl,1} = 4.0$ and $c_{sl,2} = 0.1$ are numerical constants defined in the same way as in [21] for linear elements, h_K being divided by the polynomial order for higher order interpolations.

The expression for the sub-scales is, finally:

$$\check{\mathbf{d}}^{n+1} = \tau_{sl,1,t}\left(\mathbf{R}_{sl,1}^{n+1} + \frac{\rho_{sl}\check{\mathbf{d}}^{\theta}}{\delta t^2}\right), \qquad \tau_{sl,1,t} := \left(\frac{\rho_{sl}\gamma_1}{\delta t^2} + \tau_{sl,1,K}^{-1}\right)^{-1}, \tag{3.23a}$$

$$\check{p}_{sl}^{n+1} = \tau_{sl,2}R_{sl,2}^{n+1}, \tag{3.23b}$$

where

$$\mathbf{R}_{sl}^{n+1} = [\mathbf{R}_{sl,1}^{n+1}, R_{sl,2}^{n+1}]^T = \mathbf{F}_{sl}^{n+1} - [\rho_{sl}\tilde{\mathbf{a}}_{sl}^{n+1}, 0]^T - \mathcal{A}(\tilde{\mathbf{y}}_{sl}^{n+1})$$

is the residual of the equation being solved at time step $n+1$, as it appears in Eq. (3.11).

The fully discrete and stabilized problem is now completely defined. It is given by equations (3.18), with the terms involving the subgrid scales given by the first term in Eq. (3.19), the adjoint operator given in Eqs. (3.20), the matrix of stabilization parameters in Eq. (3.21) and the sub-scales in Eqs. (3.23).

4 THREE FIELD SOLID EQUATIONS

Continuing our reformulation of the irreducible problem we expand on what we started on chapter 3, where now if the Cauchy stress $\sigma_{sl,ij}$ is additionally expressed in terms of the deviatoric stress $s_{sl,ij}$ and the pressure p_{sl} we will call this a three-field formulation. In this chapter we give an overview of the three field elasto-dynamic solid equations, their manipulation to obtain the governing equations we use all through out this work and the way we stabilize them.

4.1 SPLIT OF THE STRESS TENSOR AND FIELD EQUATIONS

From section 3.1 we may recall that the stress tensor for a neo-Hookean model can be expressed in terms of its volumetric part as:

$$p_{sl} = \frac{1}{J}\left((\lambda \ln(J) - \mu_{sl}) + \frac{\mu_{sl}\, b_{ll}}{n_d}\right), \tag{4.1}$$

and the deviatoric part as:

$$s_{sl,ij} = \frac{\mu_{sl}}{J}\left(b_{ij} - \frac{b_{ll}}{n_d}\delta_{ij}\right). \tag{4.2}$$

From this we can write the resulting system of equations as an alternative to equation (3.1) as:

$$\begin{aligned} \rho_{sl}\partial_{tt} d_i - \partial_j s_{sl,ij} - \partial_i p_{sl} &= \rho_{sl} f_{sl,i} \\ \frac{J}{\mu_{sl}} s_{sl,ij} &= \left(b_{ij} - \frac{b_{ll}}{n_d}\delta_{ij}\right), \\ \frac{J}{\lambda} p_{sl} &= \ln(J) + \frac{\mu_{sl}}{\lambda}\left(\frac{b_{ll}}{n_d} - 1\right). \end{aligned} \tag{4.3}$$

4.2 LINEARIZATION

In order to approximate a solution to this highly non-linear problem we can re-write our problem by approximating our variables $\mathbf{y}_{sl} = [\mathbf{d}, \mathbf{s}_{sl}, \mathbf{p}_{sl}]$ in terms of their increment $\delta\mathbf{y}_{sl} = [\delta\mathbf{d}, \delta\mathbf{s}_{sl}, \delta\mathbf{p}_{sl}]$ in the following form,

$$\mathbf{y}_{sl} = \tilde{\mathbf{y}}_{sl} + \delta\mathbf{y}_{sl}, \tag{4.4}$$

where $\tilde{\mathbf{y}}_{sl} = [\tilde{\mathbf{d}}, \tilde{\mathbf{s}}_{sl}, \tilde{\mathbf{p}}_{sl}]$ is the vector consisting of previously known values of $\mathbf{y}_{sl}$. This produces a problem written in an analogous form to a Newton-Raphson scheme, whereby our increment is solved in terms of the residual of the problem, as shown in the next lines.
Accounting for non-linear terms, equation (4.3) can be re-written as:

$$\rho_{sl}\partial_{tt}\delta d_i - \partial_j \delta s_{sl,ij} - \partial_i \delta p_{sl} = \rho_{sl} f_{sl,i} + \partial_j \tilde{s}_{sl,ij} + \partial_i \tilde{p}_{sl} - \rho_{sl}\partial_{tt}\tilde{d}_i, \tag{4.5a}$$

$$\frac{\tilde{J}}{2\mu_{sl}}\delta s_{sl,ij} - \frac{1}{2}\left(\frac{\partial \delta d_i}{\partial X_K}\tilde{F}_{jK} + \tilde{F}_{iK}\frac{\partial \delta d_j}{\partial X_K}\right) + \frac{1}{n_d}\left(\tilde{F}_{lK}\frac{\partial \delta d_l}{\partial X_K}\right)\delta_{ij} + \frac{\tilde{J}}{2\mu_{sl}}\left(\tilde{F}^{-1}_{Kl}\frac{\partial \delta d_l}{\partial X_K}\right)\tilde{s}_{sl,ij} = \frac{1}{2}\left(\tilde{b}_{ij} - \frac{\tilde{b}_{ll}}{n_d}\delta_{ij}\right) - \frac{\tilde{J}}{2\mu_{sl}}\tilde{s}_{sl,ij}, \tag{4.5b}$$

$$\frac{\tilde{J}}{\lambda}\delta p_{sl} + \left[\left(\frac{\tilde{J}\tilde{p}_{sl}}{\lambda} - 1\right)\tilde{F}^{-1}_{Kl} - \frac{2\mu_{sl}}{\lambda n_d}\tilde{F}_{lK}\right]\frac{\partial \delta d_l}{\partial X_K} = -\frac{\tilde{J}}{\lambda}\tilde{p}_{sl} + \ln(\tilde{J}) + \frac{\mu_{sl}}{\lambda}\left(\frac{\tilde{b}_{ii}}{n_d} - 1\right). \tag{4.5c}$$

In the same way as in chapter 3, we can denote by $\mathcal{L}_{sl}(\tilde{\mathbf{y}}_{sl}; \delta\mathbf{y}_{sl})$ the spatial linear operator on $\delta\mathbf{y}_{sl}$, for given $\tilde{\mathbf{y}}_{sl}$, appearing in the left-hand-side (LHS) of these equations. Using the notation in Eq. (3.8), we may write

$$\mathcal{M}\partial_{tt}\delta\mathbf{y}_{sl} + \mathcal{L}_{sl}(\tilde{\mathbf{y}}_{sl}; \delta\mathbf{y}_{sl}) = \mathbf{F}_{sl} - \mathcal{M}\partial_{tt}\tilde{\mathbf{y}}_{sl} - \mathcal{A}(\tilde{\mathbf{y}}_{sl}). \tag{4.6}$$

In this way, upon convergence $\delta\mathbf{y}_{sl} \approx 0$ and $\tilde{\mathbf{y}}_{sl}$ is the solution of Eq. (3.8) applied to the problem shown in equation (4.3).

4.3 GOVERNING EQUATIONS

For a certain domain Ω_{sl} with boundary Γ_{sl} and $]0, t_f[$ the interval of analysis, for a time partition from zero to a final time t_f, the three field elasto-dynamic solid equations can be written as, find a triplet $y_{sl} = [d, s_{sl}, p_{sl}]$ such that:

$$\rho_{sl}\partial_{tt}\delta d_i - \partial_j \delta s_{sl,ij} - \partial_i \delta p_{sl} = \rho_{sl} f_{sl,i} + \partial_j \tilde{s}_{sl,ij} + \partial_i \tilde{p}_{sl} - \rho_{sl}\partial_{tt}\tilde{d}_i \tag{4.7a}$$

$$\begin{aligned}\frac{\tilde{J}}{2\mu_{sl}}\delta s_{sl,ij} - \frac{1}{2}\left(\frac{\partial \delta d_i}{\partial X_K}\tilde{F}_{jK} + \tilde{F}_{iK}\frac{\partial \delta d_j}{\partial X_K}\right) + \frac{1}{n_d}\left(\tilde{F}_{lK}\frac{\partial \delta d_l}{\partial X_K}\right)\delta_{ij} \\ + \frac{\tilde{J}}{2\mu_{sl}}\left(\tilde{F}^{-1}_{Kl}\frac{\partial \delta d_l}{\partial X_K}\right)\tilde{s}_{sl,ij} = \frac{1}{2}\left(\tilde{b}_{ij} - \frac{\tilde{b}_{ll}}{n_d}\delta_{ij}\right) - \frac{\tilde{J}}{2\mu_{sl}}\tilde{s}_{sl,ij}\end{aligned} \tag{4.7b}$$

$$\begin{aligned}\frac{\tilde{J}}{\lambda}\delta p_{sl} + \left[\left(\frac{\tilde{J}\tilde{p}_{sl}}{\lambda} - 1\right)\tilde{F}^{-1}_{Kl} - \frac{2\mu_{sl}}{\lambda n_d}\tilde{F}_{lK}\right]\frac{\partial \delta d_l}{\partial X_K} \\ = -\frac{\tilde{J}}{\lambda}\tilde{p}_{sl} + \ln(\tilde{J}) + \frac{\mu_{sl}}{\lambda}\left(\frac{\tilde{b}_{ii}}{n_d} - 1\right),\end{aligned} \tag{4.7c}$$

$$\begin{aligned} d_i &= d_{i,D} && \text{on } \Gamma_{sl,D}, \\ n_{j,sl}\sigma_{ij} &= t_i && \text{on } \Gamma_{sl,N}, \\ d_i(0) &= d_i^0 && \text{in } \Omega_{sl}, t = 0, \\ \dot{d}_i(0) &= \dot{d}_i^0 && \text{in } \Omega_{sl}, t = 0, \end{aligned}$$

in $t \in]0, t_f[$, where all terms have been defined in section 2.1. Once we have obtained the governing equations of our problem we can define the corresponding weak form.

4.4 WEAK FORM

The weak form of the three field elasto-dynamic solid equations consists in finding $y_{sl} = [d, s_{sl}, p_{sl}]$ such that

$$\begin{aligned}(\rho_{sl}\partial_{tt}\delta d_i, e_i) + \left(\frac{\partial e_i}{\partial x_j}, \delta s_{sl,ij}\right) + \left(\frac{\partial e_i}{\partial x_i}, \delta p_{sl}\right) \\ = \langle e_i, \rho_{sl} f_{sl,i}\rangle + \langle e_i, t_i\rangle_{\Gamma_{sl}} - (\rho_{sl}\partial_{tt}\tilde{d}_i, e_i) \\ - \left(\frac{\partial e_i}{\partial x_j}, \tilde{s}_{sl,ij}\right) - \left(\frac{\partial e_i}{\partial x_i}, \tilde{p}_{sl}\right),\end{aligned} \tag{4.8a}$$

$$\left(\xi_{sl,ij}, \frac{\tilde{J}}{2\mu_{sl}}\delta s_{sl,ij}\right) - \left(\xi_{sl,ij}, \frac{1}{2}\left(\frac{\partial \delta d_i}{\partial X_K}\tilde{F}_{jK} + \tilde{F}_{iK}\frac{\partial \delta d_j}{\partial X_K}\right)\right) \tag{4.8b}$$
$$+ \left(\xi_{sl,ij}, \frac{1}{n_d}\left(\tilde{F}_{lK}\frac{\partial \delta d_l}{\partial X_K}\right)\delta_{ij}\right) + \left(\xi_{sl,ij}, \frac{\tilde{J}}{2\mu_{sl}}\left(\tilde{F}^{-1}_{Kl}\frac{\partial \delta d_l}{\partial X_K}\right)\tilde{s}_{sl,ij}\right)$$
$$= \left(\xi_{sl,ij}, \frac{1}{2}\left(\tilde{b}_{ij} - \frac{\tilde{b}_{ll}}{n_d}\delta_{ij}\right)\right) - \left(\xi_{sl,ij}, \frac{\tilde{J}}{2\mu_{sl}}\tilde{s}_{sl,ij}\right),$$
$$\left(q_{sl}, \frac{\tilde{J}}{\lambda}\delta p_{sl}\right) + \left(q_{sl}, \left[\left(\frac{\tilde{J}\tilde{p}_{sl}}{\lambda} - 1\right)\tilde{F}^{-1}_{Kl} - \frac{2\mu_{sl}}{\lambda n_d}\tilde{F}_{lK}\right]\frac{\partial \delta d_l}{\partial X_K}\right) \tag{4.8c}$$
$$= \left(q_{sl}, -\frac{\tilde{J}}{\lambda}\tilde{p}_{sl} + \ln(\tilde{J}) + \frac{\mu_{sl}}{\lambda}\left(\frac{\tilde{b}_{ii}}{n_d} - 1\right)\right),$$

$$(d_i(0), e_i) = (d_i^0, e_i), \qquad t = 0,$$
$$(\dot{d}_i(0), e_i) = (\dot{d}_i^0, e_i), \qquad t = 0,$$

in $t \in]0, t_f[$ for all $z_{sl} = [e, \xi_{sl}, q_{sl}]$ and satisfying initial conditions in a weak sense, where Γ_{sl} denotes the boundaries of the solid domain. It is possible to define a form B_{sl} as:

$$B_{sl}(y_{sl}; \delta y_{sl}, z_{sl}) = \left(\frac{\partial e_i}{\partial x_j}, \delta s_{sl,ij}\right) + \left(\frac{\partial e_i}{\partial x_i}, \delta p_{sl}\right) \tag{4.9}$$
$$+ \left(\xi_{sl,ij}, \frac{\tilde{J}}{2\mu_{sl}}\delta s_{sl,ij}\right) - \left(\xi_{sl,ij}, \frac{1}{2}\left(\frac{\partial \delta d_i}{\partial X_K}\tilde{F}_{jK} + \tilde{F}_{iK}\frac{\partial \delta d_j}{\partial X_K}\right)\right)$$
$$+ \left(\xi_{sl,ij}, \frac{1}{n_d}\left(\tilde{F}_{lK}\frac{\partial \delta d_l}{\partial X_K}\right)\delta_{ij}\right) + \left(\xi_{sl,ij}, \frac{\tilde{J}}{2\mu_{sl}}\left(\tilde{F}^{-1}_{lK}\frac{\partial \delta d_l}{\partial X_K}\right)\tilde{s}_{sl,ij}\right)$$
$$+ \left(q_{sl}, \frac{\tilde{J}}{\lambda}\delta p_{sl}\right) + \left(q_{sl}, \left[\left(\frac{\tilde{J}\tilde{p}_{sl}}{\lambda} - 1\right)\tilde{F}^{-1}_{Kl} - \frac{2\mu_{sl}}{\lambda n_d}\tilde{F}_{lK}\right]\frac{\partial \delta d_l}{\partial X_K}\right)$$

and a form L_{sl} as,

$$L_{sl}(z_{sl}) = \langle e_i, \rho_{sl} f_{sl,i}\rangle + \langle e_i, \sigma_{sl,ij}\cdot n_j\rangle - \left(\frac{\partial e_i}{\partial x_j}, \tilde{s}_{sl,ij}\right) - \left(\frac{\partial e_i}{\partial x_i}, \tilde{p}_{sl}\right)$$
$$+ \left(\xi_{sl,ij}, \frac{1}{2}\left(\tilde{b}_{ij} - \frac{\tilde{b}_{ll}}{n_d}\delta_{ij}\right)\right) - \left(\xi_{sl,ij}, \frac{\tilde{J}}{2\mu_{sl}}\tilde{s}_{sl,ij}\right) \tag{4.10}$$
$$+ \left(q_{sl}, -\frac{\tilde{J}}{\lambda}\tilde{p}_{sl} + \ln(\tilde{J}) + \frac{\mu_{sl}}{\lambda}\left(\frac{\tilde{b}_{ii}}{n_d} - 1\right)\right)$$

which enables us to write equation (4.8) in the following simplified form,

$$(\rho_{sl}\partial_{tt}\delta d_i, e_i) + B_{sl}(y_{sl}; \delta y_{sl}, z_{sl}) = L_{sl}(z_{sl}) - (\rho_{sl}\partial_{tt}\tilde{d}_i, e_i), \forall\, z_{sl}, \tag{4.11}$$

where $y_{sl} := [d, s_{sl}, p_{sl}]$ for $\delta y_{sl} \equiv [\delta d, \delta s_{sl}, \delta p_{sl}]$ and $z_{sl} := [e, \xi_{sl}, q_{sl}]$, where initial and boundary conditions should hold.

4.5 GALERKIN SPATIAL DISCRETIZATION

Once again, by means of the notation defined in section 1.1, the problem can be written as: find $\mathbf{y}_{sl,h}$ as the solution to the problem:

$$
\begin{aligned}
(\rho_{sl}\partial_{tt}\delta\mathbf{d}_h, \boldsymbol{e}_h) + B_{sl,h}(\mathbf{y}_{sl,h}; \delta\mathbf{y}_{sl,h}, \boldsymbol{z}_{sl,h}) &= L_{sl,h}(\boldsymbol{z}_{sl,h}) \qquad \forall\, \boldsymbol{z}_{sl,h}, \\
(\mathbf{d}_h, \boldsymbol{e}_h) &= (\mathbf{d}^0, \boldsymbol{e}_h) \qquad \forall\, \boldsymbol{e}_h, \quad t = 0.
\end{aligned} \tag{4.12}
$$

The time discretization used is the same as defined in section 2.4.

4.6 STABILIZATION OF THE NON-LINEAR THREE-FIELD SOLID PROBLEM

Additionally, following the development from chapter 1 we can express in particular the forms and operators for our stabilized three-field solid problem. If we consider the splitting of the unknown in the FE component and the sub-scale, instead of equation (3.17) we obtain:

$$
\begin{aligned}
&(\rho_{sl}\delta\mathbf{a}_h, \boldsymbol{e}_h) + \sum_K \langle \rho_{sl}\check{\mathbf{a}}, \boldsymbol{e}_h\rangle_K + B_{sl}(\tilde{\mathbf{y}}_{sl,h}; \delta\mathbf{y}_{sl,h}, [\boldsymbol{e}_h, 0, 0]) \\
&\quad + \sum_K \left\langle \frac{\partial e_{h,i}}{\partial x_j}, \check{s}_{sl,ij} \right\rangle_K + \sum_K \left\langle \frac{\partial e_{h,i}}{\partial x_i}, \check{p}_{sl} \right\rangle_K \\
&\quad = L_{sl}(\tilde{\mathbf{y}}_{sl,h}; [\boldsymbol{e}_h, 0, 0]) - \sum_K \langle \rho_{sl}\tilde{\mathbf{a}}_h, \boldsymbol{e}_h\rangle_K,
\end{aligned} \tag{4.13a}
$$

$$
\begin{aligned}
&B_{sl}(\tilde{\mathbf{y}}_{sl,h}; \delta\mathbf{y}_{sl,h}, [0, \boldsymbol{\xi}_{sl,h}, 0]) + \sum_K \left\langle \xi_{sl,h,ij}, \frac{\tilde{J}}{2\mu_{sl}}\check{s}_{ij} \right\rangle_K - \sum_K \left\langle \xi_{sl,h,ij}, \frac{\partial \check{d}_i}{\partial X_K}\tilde{F}_{jK} \right\rangle_K \\
&\quad + \sum_K \left\langle \xi_{sl,h,ij}, \frac{1}{n_d}\tilde{F}_{lK}\frac{\partial \check{d}_l}{\partial X_K}\delta_{ij} \right\rangle_K + \sum_K \left\langle \xi_{sl,ij}, \frac{\tilde{J}}{2\mu_{sl}}\tilde{F}^{-1}_{Kl}\frac{\partial \check{d}_l}{\partial X_K}\tilde{s}_{sl,ij} \right\rangle_K \\
&\quad = L_{sl}(\tilde{\mathbf{y}}_{sl,h}; [0, \boldsymbol{\xi}_{sl,h}, 0]),
\end{aligned} \tag{4.13b}
$$

$$
\begin{aligned}
&B_{sl}(\tilde{\mathbf{y}}_{sl,h}; \delta\mathbf{y}_{sl,h}, [0, 0, q_{sl,h}]) + \sum_K \left\langle q_{sl,h}, \frac{\tilde{J}}{\lambda}\check{p}_{sl} \right\rangle_K \\
&\quad + \sum_K \left\langle q_{sl,h}, \left[\left(\frac{\tilde{J}\tilde{p}_{sl,h}}{\lambda} - 1 \right) \tilde{F}^{-1}_{Kl} - \frac{2\mu_{sl}}{\lambda n_d}\tilde{F}_{lK} \right] \frac{\partial \check{d}_l}{\partial X_K} \right\rangle_K \\
&\quad = L_{sl}(\tilde{\mathbf{y}}_{sl,h}; [0, 0, q_{sl,h}]),
\end{aligned} \tag{4.13c}
$$

where the sub-scale at the current time step is $\breve{\mathbf{y}}_{sl} = [\breve{\mathbf{d}}, \breve{\mathbf{s}}_{sl}, \breve{p}_{sl}]$ and $\breve{\mathbf{a}} = \partial_{tt}\breve{\mathbf{d}}$. In these equations, we have made use of the fact that tensors $\mathbf{s}_h$ and $\boldsymbol{\xi}_{sl,h}$ are symmetric, and it is understood that all terms are evaluated at t^{n+1}, the variables with a tilde being guesses to the unknowns (from a previous iteration step, for example). Observe that the problem is linear in $\delta\mathbf{y}_{sl,h}$.

This version of the problem is unfeasible as it deals with gradients of the sub-scales for which we do not have an approximation. These terms are integrated by parts and derivatives transferred to the test functions. As explained for the abstract problem, the stabilization terms can then be written as (see equation (1.3a)):

$$\sum_K \langle \breve{\mathbf{y}}_{sl,h}, \mathcal{L}^*_{sl}(\tilde{\mathbf{y}}_{sl}; z_{sl,h})\rangle_K + \sum_K \langle \breve{\mathbf{y}}_{sl}, \mathcal{F}^*_{sl}(\tilde{\mathbf{y}}_{sl}; z_{sl,h})\rangle_{\partial K}. \tag{4.14}$$

As explained before, we shall neglect the second term, although this approximation can be relaxed (see [33]) and, in fact, is needed if stresses or pressures are discontinuous. Concerning the first term, operator $\mathcal{L}^*_{sl}(\tilde{\mathbf{y}}_{sl}; z_{sl,h})$ has three components:

$$\mathcal{L}^*_{sl}(\tilde{\mathbf{y}}_{sl}; z_{sl,h}) = [\mathcal{L}^*_{sl,1}(\tilde{\mathbf{y}}_{sl}; z_{sl,h}), \mathcal{L}^*_{sl,2}(\tilde{\mathbf{y}}_{sl}; z_{sl,h}), \mathcal{L}^*_{sl,3}(\tilde{\mathbf{y}}_{sl}; z_{sl,h})]^T,$$

the first being a vector, the second a tensor and the third a scalar, given by:

$$\begin{aligned}
\mathcal{L}^*_{sl,1}(\tilde{\mathbf{y}}_{sl}; z_{sl,h})|_i = {} & \frac{\partial}{\partial X_K}\left[\xi_{sl,h,ij}\tilde{F}_{jK} - \frac{1}{n_d}\xi_{sl,h,ll}\tilde{F}_{iK}\right] - \frac{\partial}{\partial X_K}\left(\frac{\tilde{J}}{2\mu_{sl}}\xi_{h,lm}\tilde{s}_{sl,ml}\tilde{F}^{-1}_{Ki}\right) \\
& - \frac{\partial}{\partial X_K}\left(\left(\frac{\tilde{J}\tilde{p}_{sl,h}}{\lambda} - 1\right) q_{sl,h}\tilde{F}^{-1}_{Ki}\right) \\
& + \left(\frac{2\mu_{sl}}{\lambda n_d}\frac{\partial}{\partial X_K}\left(q_{sl,h}\tilde{F}_{iK}\right)\right),
\end{aligned} \tag{4.15a}$$

$$\mathcal{L}^*_{sl,2}(\tilde{\mathbf{y}}_{sl}; z_{sl,h})|_{ij} = \frac{\partial e_{h,i}}{\partial x_j} + \frac{\tilde{J}}{2\mu_{sl}}\xi_{sl,h,ij}, \tag{4.15b}$$

$$\mathcal{L}^*_{sl,3}(\tilde{\mathbf{y}}_{sl}; z_{sl,h}) = \frac{\partial e_{h,i}}{\partial x_i} + \frac{\tilde{J}}{\lambda}q_{sl}. \tag{4.15c}$$

To obtain the final expression of the stabilized problem, we need the expression of the sub-scales to be introduced in equation (4.14), as

well as the expression of $\langle \rho_{sl} \breve{a}, e_h \rangle_K$ in equation (4.13a). For that, we just have to apply the general expressions obtained in the previous section, taking into account that we only have time derivatives of the displacements.

Using the same arguments as in [31], we will take the matrix of stabilization parameters within each element K as

$$\tau_{sl,K} = \text{diag}\,[\tau_{sl,1,K} I_{n_d}, \tau_{sl,2} I_{n_d \times n_d}, \tau_{sl,3}], \tag{4.16}$$

$$\tau_{sl,1,K} := \left(c_{sl,1} \frac{\mu_{sl}}{h_K^2} \right)^{-1}, \quad \tau_{sl,2} := c_{sl,2} 2\mu_{sl}, \quad \tau_{sl,3} := c_{sl,3} 2\mu_{sl}, \tag{4.17}$$

where $I_{n_d \times n_d}$ is the identity on second order tensors and $c_{sl,1} = 4.0$, $c_{sl,2} = 0.1$ and $c_{sl,3} = 0.1$ are numerical constants defined in the same way as in [21] for linear elements, h_K being divided by the polynomial order for higher order interpolations.

Using equation (4.16), from expression (1.10) we now have, within each element K:

$$\breve{d}^{n+1} = \tau_{sl,1,t} \left(R_{sl,1}^{n+1} + \frac{\rho_{sl} \breve{d}^{\theta}}{\delta t^2} \right), \qquad \tau_{sl,1,t} := \left(\frac{\rho_{sl} \gamma_1}{\delta t^2} + \tau_{sl,1,K}^{-1} \right)^{-1}, \tag{4.18a}$$

$$\breve{s}_{sl}^{n+1} = \tau_{sl,2} R_{sl,2}^{n+1}, \tag{4.18b}$$

$$\breve{p}_{sl}^{n+1} = \tau_{sl,3} R_{sl,3}^{n+1}, \tag{4.18c}$$

where

$$R_{sl}^{n+1} = [R_{sl,1}^{n+1}, R_{sl,2}^{n+1}, R_{sl,3}^{n+1}]^T = F_{sl}^{n+1} - [\rho_{sl} \tilde{a}_{sl}^{n+1}, 0, 0]^T - \mathcal{A}(\tilde{y}_{sl}^{n+1}) \tag{4.19}$$

is the residual of the equation being solved at time step $n+1$, as it appears in equation (4.6).

From expression (1.12) we have:

$$\begin{aligned} \langle \rho_{sl} \breve{a}^{n+1}, e_h \rangle_K = & \left\langle (1 - \tau_{sl,1,K}^{-1} \tau_{sl,1,t}) R_{sl,1}^{n+1}, e_h \right\rangle_K \\ & - \left\langle \tau_{sl,1,K}^{-1} \tau_{sl,1,t} \frac{\rho_{sl} \breve{d}^{\theta}}{\delta t^2}, e_h \right\rangle_K . \end{aligned} \tag{4.20}$$

It is seen from this expression that for the solid we have decided to approximate the acceleration of the sub-scale with the same kind of time integrator as for the FE scale, this is, a BDF2 scheme.
The fully discrete and stabilized problem is now completely defined. It is given by equations (4.13), with the terms involving the subgrid scales given by the first term in equation (4.14), the adjoint operator given in Eqs. (4.15), the matrix of stabilization parameters in equation (4.16), the sub-scales in Eqs. (4.18) and the acceleration of the sub-scales appearing in (4.13) given in equation (4.20).

Part II

FLUID DYNAMICS

INCOMPRESSIBLE NAVIER-STOKES EQUATIONS

Similarly to our approach to solid elasto-dynamics, our focus regarding fluid dynamics involves two main formulations for the Navier-Stokes equations, the first one being the standard two-field velocity–pressure equations, and the second one being the three-field (velocity–pressure–stress) equations. While we will deal with Newtonian flows exclusively in this dissertation, by making use of the benefits of mixed methods and our stabilized Variational Multi-Scale (VMS) approach it is however possible to apply any other type of description to the fluid's stress tensor. Regarding mixed methods in the field of fluid dynamics the spectrum is wider than in solid mechanics problems detailed in part i. In [21, 22] a FE velocity–stress–pressure formulation is applied to flows with non-linear viscosity, stabilized again by means of a VMS method. In [23] the same method is shown to behave better than velocity–pressure approximations for high Weissenberg number flows of visco-elastic fluids. Later, [64] expands this work, reformulating it into a logarithmic version of the problem able to cope with higher elastic effects.

Both in solids and in fluids, a major reason for using stabilized FE methods is that the Galerkin method is only stable for certain choices of the interpolating spaces for the unknowns, which turn out to be very restrictive. There are two inf-sup conditions to be met (see e.g. [69]), one between the displacement and the pressure space to yield stable pressures and another one between the stresses and the displacements in order to have control on the displacement gradients. In the case of fluids, there is also the need of using stabilized FE methods when convection dominates. The inf-sup conditions require complex interpolations, one of the first being the element proposed in

[60] and analyzed in [42]; see also [70, 72]. Stabilized FE methods allow one to use arbitrary interpolations [31], thus simplifying enormously the implementation.

In the following chapters we will detail our approach to both formulations from their governing equations, their weak form and their stabilization. In any case this will not be done with as much detail as done for the solid as further information can be found in the references already shown.

5 TWO FIELD NAVIER-STOKES EQUATIONS

In this chapter we present the governing equations and finite element approximation we employ to solve the incompressible Navier-Stokes equations formulated in a velocity–pressure model, this can be taken as the standard two field approximation.

5.1 GOVERNING EQUATIONS

Let Ω_{fl} be the domain where the fluid flow takes place, with boundary $\Gamma_{fl} = \Gamma_{D,fl} \cup \Gamma_{N,fl}$, where $\Gamma_{D,fl}$ and $\Gamma_{N,fl}$ are boundaries where Dirichlet and Neumann conditions are prescribed, respectively. Let $[0, t_f]$ be the time interval of analysis. The incompressible Navier-Stokes equations can be written as finding a velocity-pressure pair $[\mathbf{u}, p] : \Omega_{fl} \times [0, t_f[\longrightarrow \mathbb{R}^d \times \mathbb{R}$, where d is the space dimension, as the solution to the following equations:

$$
\begin{aligned}
\rho_{fl}\partial_t \mathbf{u} - 2\mu_{fl}\nabla \cdot \nabla^s \mathbf{u} + \rho_{fl}\mathbf{u} \cdot \nabla \mathbf{u} + \nabla p &= \rho_{fl}\mathbf{f} && \text{in } \Omega_{fl}, \\
\nabla \cdot \mathbf{u} &= 0 && \text{in } \Omega_{fl}, \\
\mathbf{u} &= \mathbf{u}_D && \text{on } \Gamma_{D,fl}, \\
\mathbf{n}_{fl} \cdot \boldsymbol{\sigma}_{fl} &= \mathbf{t}_{fl} && \text{on } \Gamma_{N,fl}, \\
\mathbf{u} &= \mathbf{u}^0 && \text{in } \Omega_{fl}, \qquad t = 0,
\end{aligned}
$$

in $t \in]0, t_f[$ where ρ_{fl} is the fluid density, μ_{fl} the fluid dynamic viscosity, $\nabla^s \mathbf{u}$ the symmetrical part of the velocity gradient, $\mathbf{f}$ the body acceleration vector, $\boldsymbol{\sigma}_{fl} = -p\mathbf{I} + 2\mu_{fl}\nabla^s \mathbf{u}$ the fluid Cauchy stress tensor ($\mathbf{I}$ being the identity tensor), $\mathbf{u}^0$ a prescribed initial velocity, $\mathbf{u}_D$ a prescribed ve-

locity on the boundary $\Gamma_{D,fl}$, $\mathbf{t}_{fl}$ is a prescribed traction on the boundary $\Gamma_{N,fl}$, and $\mathbf{n}_{fl}$ the normal to the boundary.

5.2 WEAK FORM

From section 1.1 we can introduce the spaces for the Navier-Stokes equations, where now $\Omega = \Omega_{fl}$. Let $\mathcal{V}_0 = \{\boldsymbol{v} \in H^1(\Omega_{fl})^d \mid \boldsymbol{v}|_{\Gamma_D} = 0\}$, $\mathcal{V}_D = \{\boldsymbol{v} \in H^1(\Omega_{fl})^d \mid \boldsymbol{v}|_{\Gamma_D} = \mathbf{u}_D\}$, $\mathcal{Q} = L^2(\Omega_{fl})$, $\mathcal{W}_0 = \mathcal{V}_0 \times \mathcal{Q}$ and $\mathcal{W}_D = \mathcal{V}_D \times \mathcal{Q}$. The weak form of the Navier-Stokes equations consists in finding $[\mathbf{u}, p] \in L^2(0, t_f; \mathcal{V}_D) \times L^1(0, t_f; \mathcal{Q})$ (or a distribution in time) such that:

$$(\rho_{fl}\partial_t \mathbf{u}, \boldsymbol{v}) - 2\mu_{fl}(\nabla^s \mathbf{u}, \nabla^s \boldsymbol{v}) + \rho_{fl}\langle \mathbf{u} \cdot \nabla \mathbf{u}, \boldsymbol{v}\rangle - (p, \nabla \cdot \boldsymbol{v}) = \langle \rho_{fl}\mathbf{f}, \boldsymbol{v}\rangle + \langle \mathbf{t}, \boldsymbol{v}\rangle_{\Gamma_{N,fl}}, \tag{5.1}$$

$$(q, \nabla \cdot \mathbf{u}) = 0, \tag{5.2}$$

$$(\mathbf{u}, \boldsymbol{v}) = (\mathbf{u}^0, \boldsymbol{v}), \qquad t = 0,$$

for all $[\boldsymbol{v}, q] \in \mathcal{V}_0 \times \mathcal{Q}$ in $t \in]0, t_f[$. For $\mathbf{y}_{fl} \equiv [\mathbf{u}, p] :]0, t_f[\longrightarrow \mathcal{W}_D$ and $\boldsymbol{z}_{fl} \equiv [\boldsymbol{v}, q] \in \mathcal{W}_0$, we can define the form B as

$$B(\mathbf{y}_{fl}, \boldsymbol{z}_{fl}) = 2\mu_{fl}(\nabla^s \mathbf{u}, \nabla^s \boldsymbol{v}) + \rho_{fl}\langle \mathbf{u} \cdot \nabla \mathbf{u}, \boldsymbol{v}\rangle - (p, \nabla \cdot \boldsymbol{v}) + (q, \nabla \cdot \mathbf{u}),$$

and the linear form L as

$$L(\boldsymbol{z}_{fl}) = \langle \rho_{fl}\mathbf{f}, \boldsymbol{v}\rangle + \langle \mathbf{t}, \boldsymbol{v}\rangle_{\Gamma_{N,fl}},$$

which enable us to write (5.1)-(5.2) in the following simplified form:

$$(\rho_{fl}\partial_t \mathbf{u}, \boldsymbol{v}) + B(\mathbf{y}_{fl}, \boldsymbol{z}_{fl}) = L(\boldsymbol{z}_{fl}) \quad \forall\, \boldsymbol{z}_{fl} \in \mathcal{W}_0. \tag{5.3}$$

We linearize the term $\rho_{fl}\langle \mathbf{u} \cdot \nabla \mathbf{u}, \boldsymbol{v}\rangle$ by means of a Picard linearization scheme.

5.3 GALERKIN SPATIAL DISCRETIZATION

For the spatial discretization, the standard Galerkin finite element approximation can be defined as follows. In the case $\Omega = \Omega_{fl}$, we can

now construct conforming finite element spaces $\mathcal{V}_h \subset \mathcal{V}_D$, $\mathcal{Q}_h \subset \mathcal{Q}$ and $\mathcal{W}_{h,D} = \mathcal{V}_h \times \mathcal{Q}_h$, as well as $\mathcal{V}_{h,0} \subset \mathcal{V}_0$ and $\mathcal{W}_{h,0} = \mathcal{V}_{h,0} \times \mathcal{Q}_h$, in the usual manner. Then the problem can be written as: find $\mathbf{y}_{fl,h} :]0, t_f[\longrightarrow \mathcal{W}_{h,D}$ as the solution to the problem:

$$\begin{aligned} (\rho_{fl}\partial_t \mathbf{u}_h, \boldsymbol{\nu}_h) + B(\mathbf{y}_{fl,h}, \mathbf{z}_{fl,h}) &= L(\mathbf{z}_{fl,h}) \qquad \forall\, \mathbf{z}_{fl,h} \in \mathcal{W}_{h,0}, \\ (\mathbf{u}_h, \boldsymbol{\nu}_h) &= (\mathbf{u}^0, \boldsymbol{\nu}_h) \qquad \forall\, \boldsymbol{\nu}_h \in \mathcal{V}_{h,0}, \quad t = 0. \end{aligned} \tag{5.4}$$

5.4 TIME DISCRETIZATION

Let us consider a uniform partition of the time interval $]0, t_f[$ of size δt, and let us denote with superscript n the time level. For the temporal discretization, usual finite difference schemes can be adopted. In particular, we have used the second order Backward Difference (BDF2) scheme, which has the following form:

$$\left.\frac{\partial \mathbf{u}_h}{\partial t}\right|_{t^{n+1}} = \frac{3\mathbf{u}_h^{n+1} - 4\mathbf{u}_h^n + \mathbf{u}_h^{n-1}}{\delta t} + \mathcal{O}(\delta t^2) =: \delta_{2,t}\mathbf{u}_h^{n+1} + \mathcal{O}(\delta t^2),$$

where $t^k = k\delta t$, $k = n-1,\ n,\ n+1$.

5.5 STABILIZATION OF THE TWO-FIELD FLUID PROBLEM

To circumvent the restrictions imposed by the inf-sup condition and convection dominated flows, a Variational Multi-Scale (VMS) stabilization is applied, originally proposed in [48] and later further developed in [28, 30] (see also [32] for a review). When applied to the Navier-Stokes problem, the time discrete version of Eq. (5.4) is replaced by:

$$\begin{aligned} (\rho_{fl}\delta_{2,t}\mathbf{u}_h^{n+1}, \boldsymbol{\nu}_h) + B(\mathbf{y}_{fl,h}^{n+1}, \mathbf{z}_{fl,h}) + \sum_K \left\langle \tilde{\mathbf{u}}^{n+1}, \rho_{fl}\mathbf{u}_h^{n+1}\cdot\nabla\boldsymbol{\nu}_h + \mu_{fl}\Delta\boldsymbol{\nu}_h + \nabla q_h \right\rangle_K \\ - \sum_K \left\langle \tilde{p}^{n+1}, \nabla\cdot\boldsymbol{\nu}_h \right\rangle_K = L(\mathbf{z}_{fl,h}), \end{aligned} \tag{5.5}$$

where $\tilde{\mathbf{u}}^{n+1}$ and $\tilde{p}^{n+1}$ are the solution of

$$\frac{\rho_{fl}}{\Delta t}\left(\tilde{\mathbf{u}}^{n+1} - \tilde{\mathbf{u}}^n\right) + \frac{1}{\tau_1}\tilde{\mathbf{u}}^{n+1} = \Pi^{\perp}\left(\mathbf{r}\left(\mathbf{y}_{fl,h}^{n+1}\right)\right), \tag{5.6}$$

$$\frac{1}{\tau_2}\tilde{p}^{n+1} = -\Pi^{\perp}\left(\nabla\cdot\mathbf{u}_h^{n+1}\right), \tag{5.7}$$

within each element domain K of the finite element partition of the fluid domain, with

$$\mathbf{r}\left(\mathbf{y}_{fl,h}^{n+1}\right) = \rho_{fl}\delta_{2,t}\mathbf{u}_h^{n+1} - \mu_{fl}\Delta\mathbf{u}_h^{n+1} + \rho_{fl}\mathbf{u}_h^{n+1}\cdot\nabla\mathbf{u}_h^{n+1} + \nabla p_h^{n+1} - \rho_{fl}\mathbf{f}^{n+1},$$

$$\tau_1 = \left[c_1\frac{\mu_{fl}}{h^2} + c_2\frac{\rho_{fl}|\mathbf{u}_h|_K}{h}\right]^{-1}, \tag{5.8}$$

$$\tau_2 = c_3\frac{h^2}{\tau_1}. \tag{5.9}$$

In Eqs. (5.6)-(5.7), $\Pi^{\perp}$ is the projection orthogonal to the finite element space (either of velocities or of pressures), computed as $\Pi^{\perp} = I - \Pi$, Π being the projection onto the adequate finite element space. In Eqs. (5.8)-(5.9), $|\mathbf{u}_h|_K$ is the mean velocity modulus in element K, h is the element size and c_1, c_2 and c_3 are stabilization constants. For linear elements we take $c_1 = 4.0$, $c_2 = 2.0$ and $c_3 = 1.0$; for quadratic elements we use the same values but taking h half the element size (roughly the distance between nodes of the element), as justified in [29].

6 THREE FIELD NAVIER-STOKES EQUATIONS

In this chapter a short review of the three field Navier-Stokes equations is given as well as the spatial discretization schemes used as shown in [20, 23].

6.1 GOVERNING EQUATIONS

For a certain domain Ω_{fl} with boundary Γ_{fl} and $]0, t_f[$ the interval of analysis, from zero to a final time t_f, the three field Navier-Stokes problem consists in finding $[\mathbf{u}, \mathbf{s}_{fl}, p_{fl}]$ such that:

$$\rho_{fl}\partial_t \mathbf{u} - \nabla \cdot \mathbf{s}_{fl} + \rho_{fl}\mathbf{u} \cdot \nabla \mathbf{u} + \nabla p_{fl} = \rho_{fl}\mathbf{f}_{fl} \qquad \text{in } \Omega_{fl}, \tag{6.1a}$$

$$\frac{1}{2\mu_{fl}}\mathbf{s}_{fl} - \nabla^s \mathbf{u} = 0 \qquad \text{in } \Omega_{fl}, \tag{6.1b}$$

$$\nabla \cdot \mathbf{u} = 0 \qquad \text{in } \Omega_{fl}, \tag{6.1c}$$

$$\mathbf{u} = \mathbf{u}_D \qquad \text{on } \Gamma_{fl,D},$$

$$\mathbf{n}_{fl} \cdot \boldsymbol{\sigma} = \mathbf{t} \qquad \text{on } \Gamma_{fl,N},$$

$$\mathbf{u}(0) = \mathbf{u}^0 \qquad \text{in } \Omega_{fl}, \qquad t = 0,$$

in $t \in]0, t_f[$ where we make use of all the terms defined in section 5.1 and in this case $\mathbf{s}_{fl}$ is the deviatoric component of the fluid stress tensor.

6.2 WEAK FORM

The weak form of the three field Navier-Stokes equations consists in finding $[\mathbf{u}, \mathbf{s}_{fl}, p_{fl}]$ such that for a domain Ω_{fl} in $t \in]0, t_f[$,

$$(\rho_{fl}\partial_t \mathbf{u}, \boldsymbol{\nu}) + (\mathbf{s}_{fl}, \nabla^s \boldsymbol{\nu}) + (\rho_{fl}\mathbf{u} \cdot \nabla \mathbf{u}, \boldsymbol{\nu}) \tag{6.2a}$$

$$
\begin{aligned}
-(p_{\mathfrak{fl}}, \nabla \cdot \boldsymbol{v}) &= \langle \rho_{\mathfrak{fl}} \boldsymbol{f}_{\mathfrak{fl}}, \boldsymbol{v} \rangle + \langle \boldsymbol{\sigma}_{\mathfrak{fl}} \cdot \boldsymbol{n}, \boldsymbol{v} \rangle_{\Gamma_{\mathfrak{fl},N}}, \\
\left(\frac{1}{2\mu_{\mathfrak{fl}}} \boldsymbol{s}_{\mathfrak{fl}}, \boldsymbol{\xi}_{\mathfrak{fl}} \right) - (\nabla^s \boldsymbol{u}, \boldsymbol{\xi}_{\mathfrak{fl}}) &= 0, \qquad (6.2b) \\
(\nabla \cdot \boldsymbol{u}, q_{\mathfrak{fl}}) &= 0, \qquad (6.2c) \\
\boldsymbol{u}(0) &= \boldsymbol{u}^0 \qquad t = 0,
\end{aligned}
$$

for all $[\boldsymbol{v}, \boldsymbol{\xi}_{\mathfrak{fl}}, q_{\mathfrak{fl}}]$ and satisfying initial conditions in a weak sense. It is possible to define a form $B_{\mathfrak{fl}}$ as:

$$
\begin{aligned}
B_{\mathfrak{fl}}(\boldsymbol{y}_{\mathfrak{fl}}, \boldsymbol{z}_{\mathfrak{fl}}) = (\boldsymbol{s}_{\mathfrak{fl}}, \nabla^s \boldsymbol{v}) + \langle \rho_{\mathfrak{fl}} \boldsymbol{u} \cdot \nabla \boldsymbol{u}, \boldsymbol{v} \rangle + (p_{\mathfrak{fl}}, \nabla \cdot \boldsymbol{v}) \\
+ (\nabla \cdot \boldsymbol{u}, q_{\mathfrak{fl}}) + \left(\frac{1}{2\mu_{\mathfrak{fl}}} \boldsymbol{s}_{\mathfrak{fl}}, \boldsymbol{\xi}_{\mathfrak{fl}} \right) + (\nabla^s \boldsymbol{u}, \boldsymbol{\xi}_{\mathfrak{fl}})
\end{aligned} \qquad (6.3)
$$

and a form,

$$
L_{\mathfrak{fl}}(\boldsymbol{z}_{\mathfrak{fl}}) = \langle \rho_{\mathfrak{fl}} \boldsymbol{f}_{\mathfrak{fl}}, \boldsymbol{v} \rangle + \langle \boldsymbol{\sigma}_{\mathfrak{fl}} \cdot \boldsymbol{n}, \boldsymbol{v} \rangle_{\Gamma_{\mathfrak{fl},N}} \qquad (6.4)
$$

which enables us to write equation (6.2) in the following simplified form,

$$
(\rho_{\mathfrak{fl}} \partial_t \boldsymbol{u}, \boldsymbol{v}) + B_{\mathfrak{fl}}(\boldsymbol{y}_{\mathfrak{fl}}, \boldsymbol{z}_{\mathfrak{fl}}) = L_{\mathfrak{fl}}(\boldsymbol{z}_{\mathfrak{fl}}), \forall\, \boldsymbol{z}_{\mathfrak{fl}}, \qquad (6.5)
$$

where $\boldsymbol{y}_{\mathfrak{fl}} := [\boldsymbol{u}, \boldsymbol{s}_{\mathfrak{fl}}, p_{\mathfrak{fl}}]$ and $\boldsymbol{z}_{\mathfrak{fl}} := [\boldsymbol{v}, \boldsymbol{\xi}_{\mathfrak{fl}}, q_{\mathfrak{fl}}]$, where initial conditions should hold.

6.3 GALERKIN SPATIAL DISCRETIZATION

Making use of the notation developed in section 1.1 the spatial discretization for the Navier-Stokes problem can be written as: find $\boldsymbol{y}_{\mathfrak{fl},h}$ as the solution to the problem:

$$
\begin{aligned}
(\rho_{\mathfrak{fl}} \partial_t \boldsymbol{u}_h, \boldsymbol{v}_h) + B_{\mathfrak{fl}}(\boldsymbol{y}_{\mathfrak{fl},h}, \boldsymbol{z}_{\mathfrak{fl},h}) &= L_{\mathfrak{fl}}(\boldsymbol{y}_{\mathfrak{fl},h}) \qquad \forall\, \boldsymbol{y}_{\mathfrak{fl},h}, \qquad (6.6) \\
(\boldsymbol{u}_h, \boldsymbol{v}_h) &= (\boldsymbol{u}^0, \boldsymbol{v}_h) \qquad \forall\, \boldsymbol{y}_{\mathfrak{fl},h} \in \mathcal{V}_{h,0}, \quad t = 0.
\end{aligned}
$$

6.4 STABILIZATION OF THE THREE-FIELD FLUID PROBLEM

The discrete Navier-Stokes three field problem suffers from the same instability issues as the solid three field problem, i.e incompatibility of

interpolation spaces plus the instabilities present when dealing with dominant convection. In this regard we follow the same choice as previously done to stabilize our problem as shown in chapter 1.
The adjoint operator for the fluid problem the can be expressed as,

$$\mathcal{L}^*_{fl}(\mathbf{y}_{fl,h}) = \begin{bmatrix} \nabla\cdot\boldsymbol{\xi}_h + \nabla q_{fl,h} - \rho_{fl}\mathbf{u}\cdot\nabla\boldsymbol{\nu}_h \\ -\nabla\cdot\boldsymbol{\nu}_h \\ \frac{1}{2\mu_{fl}}\boldsymbol{\xi}_h + \nabla^s\boldsymbol{\nu}_h \end{bmatrix}, \tag{6.7}$$

where the term $\rho_{fl}\mathbf{u}\cdot\nabla\boldsymbol{\nu}_h$ is linearized by means of a Picard scheme. We define the matrix of stabilization parameters $\boldsymbol{\tau}_{fl,k}$ as:

$$\boldsymbol{\tau}_{fl,k} = \begin{bmatrix} \left[c_{fl,1}\frac{\mu_{fl}}{h_1^2} + c_{fl,2}\frac{\rho_{fl}\|\mathbf{u}_h\|}{h_2}\right]^{-1} & 0 & 0 \\ 0 & c_{fl,3}2\mu_{fl} & 0 \\ 0 & 0 & c_{f,4}2\mu_{fl} \end{bmatrix}, \tag{6.8}$$

where $c_{fl,1} = 4.0$, $c_{fl,2} = 1.0$, $c_{fl,3} = 0.1$ and $c_{fl,4} = 0.1$ are numerical constants as defined in [20].
Finally we can write the specific form of equation (1.13) for the three field fluid problem as:

$$\begin{aligned} &\left(\rho_{fl}\frac{\gamma_1\mathbf{u}_h}{\Delta t},\boldsymbol{\nu}_h\right) + B_{fl}(\mathbf{y}_{fl},\mathbf{z}_{fl,h}) \\ &\quad -\left(\mathcal{L}_{fl}(\mathbf{y}_{fl,h}) + \rho_{fl}\frac{\gamma_1\mathbf{u}_h}{\Delta t},\boldsymbol{\tau}_{fl,t}\mathcal{L}^*_{fl}(\mathbf{z}_{fl,h}) + \mathbf{z}_{fl,h}(1-\boldsymbol{\tau}^{-1}_{fl,k}\boldsymbol{\tau}_{fl,t})\right) \\ &\qquad = \langle \mathbf{f}_{fl} + \rho_{fl}\frac{\mathbf{u}_h^\theta}{\Delta t},\mathbf{z}_{fl,h}\rangle \\ &\qquad -\langle \mathbf{f}_{fl} + \rho_{fl}\frac{\mathbf{u}_h^\theta}{\Delta t},\boldsymbol{\tau}_{fl,t}\mathcal{L}^*_{fl}(\mathbf{z}_{fl,h}) + \mathbf{z}_{fl,h}(1-\boldsymbol{\tau}^{-1}_{fl,k}\boldsymbol{\tau}_{fl,t})\rangle \\ &\qquad +\langle \rho_{fl}\frac{\breve{\mathbf{u}}^\theta}{\Delta t},\mathbf{z}_{fl,h}\boldsymbol{\tau}^{-1}_{fl,k}\boldsymbol{\tau}_{fl,t} - \boldsymbol{\tau}_{fl,t}\mathcal{L}^*_{fl}(\mathbf{z}_{fl,h})\rangle \;\;\forall\,\mathbf{z}_{fl,h}, \end{aligned} \tag{6.9}$$

where, in this case $\mathbf{u}^\theta$ and $\breve{\mathbf{u}}^\theta$ are the past time interval values for the velocity and the velocity sub-scale respectively. We have taken into account time evolution only for the velocities (scale and sub-scale) as it is the only variable in this formulation with time derivative.
The time discretization used is the same as defined in section 5.4.

Part III

FLUID STRUCTURE INTERACTION

FLUID STRUCTURE INTERACTION

Fluid Structure Interaction (FSI) is a topic of constant research and development, and even though fluid and solid formulations might be well understood, FSI remains a complex problem owing to factors such as the added mass effect, instabilities of the fluid and solid problems, and the overall conditioning of the problem due to factors like different scales of material parameters (this is viscosities of 10^{-3} and Young modulus of 10^{6}), temporal stiffness caused by the coupling of a parabolic problem (Navier-Stokes equations) and a Hyperbolic one (Elasticity equations) and the bad conditioning that arises from the discretization of second order spatial differential operators [68]. Broadly, research in the field can be grouped into two categories based on how the mesh is treated, namely, conforming and non conforming methods. Essentially, conforming mesh methods consider interface conditions as physical boundary conditions, thus treating the interface as part of the solution. In this approach, the mesh reproduces or conforms to the interface; when the interface is moved it is also necessary to displace the mesh, which carries on all related problems of mesh recalculation and inherent instabilities of the method, be it partitioned or monolithic, see [4, 12, 13, 15, 38, 39, 56]. On the other hand, non-conforming methods treat the interface and boundary as constraints imposed on the governing equations, which makes possible to use meshes that do not reproduce the interface; the main problem in this case is the treatment of the interface conditions and the complexity of the formulation, see for example [1, 9, 16, 45, 65, 75] for further reading. For a general review of significant Fluid-Structure Interaction (FSI) advances and developments, see [46]. Overall, for highly non-linear problems, arriving at a solution can take a large

amount of time, an issue that becomes even more apparent when dealing with problems with a high number of degrees of freedom. It is well known that Reduced Order Models (Reduced Order Model (ROM)) can speed up solution time dramatically, which leads to the idea of introducing them into FSI analysis in part iv.

7 FIELD TO FIELD PROBLEM

Once all ingredients have been identified (fluid and solid models), it is possible to detail the process of dealing with FSI problems by means of what we came to call Field to Field (F2F) interaction. In this section we first express the F2F-FSI equations in weak form, and then we detail the FSI algorithm as well as the boundary relaxation scheme used.

7.1 WEAK FORM OF THE FIELD TO FIELD PROBLEM

As an interaction problem, each one of the formulations is treated naturally in different frames of reference. While the mesh tracks the solid particles, it does not track the fluid. The approach followed in this work can be taken as the traditional in a broad sense, where the fluid is treated by means of an Arbitrary-Lagrangian-Eulerian formulation while the solid follows the usual Updated Lagrangian approach. [35] explains in a very detailed manner the ALE formulation, as well as its advantages and disadvantages. The mesh movement algorithm has been taken from [26], which has proven simple, robust and reliable. In what follows $\mathbf{c}$ is known as the convection velocity from the domain point of view, which is given in the discrete level by $\mathbf{c} = \mathbf{u} - \mathbf{u}_{\text{mesh}}$, where $\mathbf{u}_{\text{mesh}}$ is the velocity of the points in the computational domain to which the unknowns are referred. Also note that in this form, the domain to which the fluid and solid pertains, $\Omega_{\text{fl}}(t)$ and $\Omega_{\text{sl}}(t)$, respectively, is now time dependent as it changes according to what the ALE formulation dictates.

Borrowing from the notation developed in previous chapters we

can expand it to account for moving domain and to take into account the interaction between sub-domains;

7.1.1 *Standard FSI problem*

The standard two-field/one-field FSI problem can be stated as; for a time partition from zero to a final time t_f, find $[\mathbf{u}, p_{fl}, \mathbf{d}]$ such that

$$\begin{aligned}
&\rho_{fl}(\boldsymbol{v}, \partial_t \mathbf{u}) - 2\mu_{fl}(\nabla^s \boldsymbol{v}, \nabla^s \mathbf{u}) && && (7.1a)\\
&\quad + \rho_{fl}\langle \boldsymbol{v}, \mathbf{c}\cdot\nabla\mathbf{u}\rangle - (\nabla\cdot\boldsymbol{v}, p) = \langle \boldsymbol{v}, \rho_{fl}\mathbf{f}\rangle + \langle \boldsymbol{v}, \mathbf{t}_{fl}\rangle_{\Gamma_{N,fl}} && \text{in } \Omega(t)_{fl},\\
&\qquad (q, \nabla\cdot\mathbf{u}) = 0 && \text{in } \Omega(t)_{fl},\\
&\qquad (\boldsymbol{e}, \rho_{sl}\partial_{tt}\mathbf{d}) - (\nabla^s \boldsymbol{e}, \boldsymbol{\sigma}_{sl}) = \langle \boldsymbol{e}, \rho_{sl}\mathbf{f}\rangle + \langle \boldsymbol{e}, \mathbf{t}_{sl}\rangle_{\Gamma_{N,s}} && \text{in } \Omega(t)_{sl}, && (7.1b)\\
&\qquad \mathbf{u} = \partial_t \mathbf{d} && \text{on } \Gamma(t)_I,\\
&\qquad \mathbf{n}_{sl}\cdot\boldsymbol{\sigma}_{sl} + \mathbf{n}_{fl}\cdot\boldsymbol{\sigma}_{fl} = 0 && \text{on } \Gamma(t)_I,
\end{aligned}$$

for all $[\boldsymbol{v}, q, \boldsymbol{e}]$ in $t \in]0, t_f[$ and satisfying initial conditions in a weak sense. With $\boldsymbol{\sigma}_{fl} = -p_{fl}\mathbf{I}_{n_d} + 2\mu_{fl}\nabla^s\mathbf{u}$ for a Newtonian fluid and $\boldsymbol{\sigma}_{sl} = \frac{1}{J}\left[\lambda_{sl}\ln(J)\mathbf{I}_{n_d} + \mu_{sl}(\mathbf{b} - \mathbf{I})\right]$ for a Neo-Hookean solid as previously defined.

7.1.2 *Two field FSI problem*

The two-field FSI problem can be stated as; for a time partition from zero to a final time t_f, find $[\mathbf{u}, p_{fl}, \mathbf{d}, p_{sl}]$ such that

Fluid equations, defined for $\Omega(t)_{fl}$:

$$\begin{aligned}
&\rho_{fl}(v_i, \partial_t u_i) - \mu_{fl}(\partial_i v_j + \partial_j v_i, \partial_i u_j + \partial_j u_i) && (7.2a)\\
&\qquad + \rho_{fl}\langle v_i, c_j\partial_j u_i\rangle - (\partial_i v_i, p) = \langle v_i, \rho_{fl} f_i\rangle + \langle v_i, t_{fl,i}\rangle_{\Gamma_{N,fl}}\\
&\qquad\qquad (q, \partial_i u_i) = 0, && (7.2b)
\end{aligned}$$

Solid equations, defined for $\Omega(t)_{sl}$:
Solve until convergence for $\delta y_{sl} \approx 0$, such that $y_{sl} \approx \tilde{y}_{sl}$

$$\begin{aligned}
&\left(e_i, \frac{\rho_{sl}}{2\mu_{sl}}\partial_{tt}\delta d_i\right) + \left(\frac{\partial e_i}{\partial x_j}, \frac{1}{2\tilde{J}}\partial_j\left(\frac{\partial \delta d_i}{\partial X_K}\tilde{F}_{jK} + \tilde{F}_{iK}\frac{\partial \delta d_j}{\partial X_K}\right)\right) \qquad (7.2c)\\
&\quad - \left(\frac{\partial e_i}{\partial x_j}, \frac{\delta_{ij}}{\tilde{J}nd}\partial_j\left(\tilde{F}_{lK}\frac{\partial \delta d_l}{\partial X_K}\right)\right) - \left(\frac{\partial e_i}{\partial x_j}, \frac{1}{2\tilde{J}}\left(\tilde{F}^{-1}_{Kl}\frac{\partial \delta d_l}{\partial X_K}\right)\partial_j\left(\tilde{b}_{ij} - \frac{\tilde{b}_{ll}}{nd}\delta_{ij}\right)\right)\\
&\quad + \left(\frac{\partial e_i}{\partial x_i}, \frac{1}{2\mu_{sl}}\delta p_{sl}\right) = \langle e_i, \frac{\rho_{sl}}{2\mu_{sl}} f_{sl,i}\rangle + \langle e_i, \frac{1}{2\mu_{sl}} t_i\rangle\\
&\quad - \left(\frac{\partial e_i}{\partial x_j}, \frac{1}{2\tilde{J}}\partial_j\left(\tilde{b}_{ij} - \frac{\tilde{b}_{ll}}{nd}\delta_{ij}\right)\right) - \left(\frac{\partial e_i}{\partial x_i}, \frac{1}{2\mu_{sl}}\partial_i \tilde{p}_{sl}\right)\\
&\left(q_{sl}, \frac{\tilde{J}}{\lambda}\delta p_{sl}\right) + \left(q_{sl}, \left[\left(\frac{\tilde{J}\tilde{p}_{sl}}{\lambda} - 1\right)\tilde{F}^{-1}_{Kl} - \frac{2\mu_{sl}}{\lambda nd}\tilde{F}_{lK}\right]\frac{\partial \delta d_l}{\partial X_K}\right) \qquad (7.2d)\\
&\quad = \left(q_{sl}, -\frac{\tilde{J}}{\lambda}\tilde{p}_{sl} + \ln(\tilde{J}) + \frac{\mu_{sl}}{\lambda}\left(\frac{\tilde{b}_{ii}}{nd} - 1\right)\right),
\end{aligned}$$

Interaction boundary defined on $\Gamma_I(t)$:

$$\begin{aligned}
&u_i = \partial_t d_i\\
&n_{s,j}\left(p_{sl} I_{n_d,ij} + \left[\frac{\mu_{sl}}{J}\left(b_{ij} - \frac{b_{ll}}{nd}\delta_{ij}\right)\right]\right) = n_{fl,j}\left(-p_{fl} I_{n_d,ij} + \mu_{fl}\left(\partial_i u_j + \partial_j u_i\right)\right),
\end{aligned}$$

for all $[v_i, q_{fl}, e_i, q_{sl}]$ in $t \in]0, t_f[$ and satisfying initial conditions in a weak sense.

7.1.3 *Three field FSI problem*

The three-field FSI problem can be stated as; for a time partition from zero to a final time t_f, find $[u, s_{fl}, p_{fl}, d, s_{sl}, p_{sl}]$ such that

Fluid equations, defined for $\Omega(t)_{fl}$:

$$\begin{aligned}
&(v_i, \rho_{fl}\partial_t u_i) - \left(\frac{1}{2}\left(\partial_j v_i + \partial_i v_j\right), s_{fl,ij}\right)\\
&\qquad + (v_i, \rho_{fl} c_j \partial_j u_i) + (\partial_i v_i, p_{fl}) = \langle v_i, \rho_{fl} f_{fl,i}\rangle + \langle v_i, \sigma_{fl,ij} n_j\rangle \qquad (7.3a)\\
&\left(\xi_{fl,ij}, \frac{1}{2\mu_{fl}} s_{fl,ij}\right) - \left(\xi_{fl,ij}, \frac{1}{2}\left(\partial_j u_i + \partial_i u_j\right)\right) = 0 \qquad (7.3b)
\end{aligned}$$

$$(q_{fl}, \partial_i u_i) = 0 \tag{7.3c}$$

Solid equations, defined for $\Omega(t)_{sl}$:
Solve until convergence for $\delta y_{sl} \approx 0$, such that $y_{sl} \approx \tilde{y}_{sl}$

$$\begin{aligned}
&(\rho_{sl}\partial_{tt} d_i, e_i) + \left(\frac{\partial e_i}{\partial x_j}, \delta s_{sl,ij}\right) + \left(\frac{\partial e_i}{\partial x_i}, \delta p_{sl}\right) \qquad (7.3d)\\
&\quad = \langle e_i, \rho_{sl} f_{sl,i}\rangle + \langle e_i, \sigma_{sl,ij}\cdot n_j\rangle - \left(\frac{\partial e_i}{\partial x_j}, \tilde{s}_{sl,ij}\right) - \left(\frac{\partial e_i}{\partial x_i}, \tilde{p}_{sl}\right)\\
&\left(\xi_{sl,ij}, \frac{\tilde{J}}{2\mu_{sl}}\delta s_{sl,ij}\right) - \left(\xi_{sl,ij}, \frac{1}{2}\left(\frac{\partial \delta d_i}{\partial X_K}\tilde{F}_{jK} + \tilde{F}_{iK}\frac{\partial \delta d_j}{\partial X_K}\right)\right) \qquad (7.3e)\\
&\quad + \left(\xi_{sl,ij}, \frac{1}{nd}\left(\tilde{F}_{lK}\frac{\partial \delta d_l}{\partial X_K}\right)\delta_{ij}\right) + \left(\xi_{sl,ij}, \frac{\tilde{J}}{2\mu_{sl}}\left(\tilde{F}^{-1}_{Kl}\frac{\partial \delta d_l}{\partial X_K}\right)\tilde{s}_{sl,ij}\right)\\
&\quad = \left(\xi_{sl,ij}, \frac{1}{2}\left(\tilde{b}_{ij} - \frac{\tilde{b}_{ll}}{nd}\delta_{ij}\right)\right) - \left(\xi_{sl,ij}, \frac{\tilde{J}}{2\mu_{sl}}\tilde{s}_{sl,ij}\right)\\
&\left(q_{sl}, \frac{\tilde{J}}{\lambda}\delta p_{sl}\right) + \left(q_{sl}, \left[\left(\frac{\tilde{J}\tilde{p}_{sl}}{\lambda} - 1\right)\tilde{F}^{-1}_{Kl} - \frac{2\mu_{sl}}{\lambda nd}\tilde{F}_{lK}\right]\frac{\partial \delta d_l}{\partial X_K}\right) \qquad (7.3f)\\
&\quad = \left(q_{sl}, -\frac{\tilde{J}}{\lambda}\tilde{p}_{sl} + \ln(\tilde{J}) + \frac{\mu_{sl}}{\lambda}\left(\frac{\tilde{b}_{ii}}{nd} - 1\right)\right)
\end{aligned}$$

Interaction boundary defined on $\Gamma_I(t)$:

$$u_i = \partial_t d_i$$

$$n_{fl,ij}\cdot(-p_{fl} I_{n_d,ij} + s_{fl,ij}) + n_{sl,ij}\cdot(p_{sl} I_{n_d,ij} + s_{sl,ij}) = 0$$

for all $[v_i, \xi_{fl,ij}, q_{fl}, e_i, \xi_{sl,ij}, q_{sl}]$ in $t \in]0, t_f[$ and satisfying initial conditions in a weak sense.

8 COUPLING SCHEME

There are various ways to treat the numerical system for the interaction problem regardless of the particular formulation used to solve each domain. In a monolithic coupling the whole problem is assembled and solved, coupling is treated implicitly (see for example [37, 63, 73]). This approach benefits from increased stability on the solution but requires a solver specially tailored for coupled FSI problems. On the other hand, partitioned approaches assemble each domain independently and coupling is achieved through right-hand-side terms of each system that need to be guessed. For strongly coupled systems, sub-iterations, and very often relaxation, are necessary to guarantee convergence on the interaction boundaries. In some cases, a high number of coupling iterations are necessary to achieve convergence (see [2, 55]). Finally, one can use a staggered coupling (or loosely coupled interaction); this is essentially a partitioned approach where the boundary conditions are treated explicitly and no sub-iterations are done. This approach is less popular as it can suffer from instabilities like the added mass effect (see for example [41]), severe time-step limitations and the fact that global invariants like energy conservation will not be fulfilled [61]. For a comprehensive discussion on the added mass effect on partitioned coupled solvers see [84].

In this work we employ a partitioned strongly coupled scheme to achieve domain coupling; this means that for every time-step each domain is iterated independently until convergence is achieved for our field variables on the interaction boundary. This creates the necessity of an additional iteration loop that guarantees coupling convergence. In total we are left with three coupling blocks, these

being the internal solver convergence, the non-linearity convergence of each problem (fluid and solid) and the coupling convergence for the interaction boundary. This is clarified in Chapter 9. As a main difference from standard FSI algorithms, two and three field FSI has an additional cost in the information transfer between sub-domains, as not only displacement or velocity has to be passed but as well their associated pressures and deviatoric stresses in the latter case, all quantities have to be interpolated if non matching meshes are used. Note that this means we are passing from one domain to another each field separately to then assemble the tractions and boundary velocities for solid and fluid, respectively. In our implementation, iteration by sub-domain can be done for non matching meshes by means of the Lagrange interpolation functions to ensure continuity of certain quantities. However there are other types of interpolation as shown in [47] for example. The order in which we iterate is the standard one, the one that guarantees stability of the process due to the different 'stiffnesses' of the sub-problems, namely, a Dirichlet-Neumann coupling. The way to proceed is to determine the shape of the fluid domain from the deformation obtained at a certain iteration within a given time step for the solid, as well as the velocity of the domain boundary; from this, one can compute the velocity of the mesh in the fluid domain and solve the flow equations. Once the field variables in the fluid are computed, the resulting normal stress on the solid boundary can be obtained, and this can be used to solve the problem in the solid domain. The process needs to be repeated until convergence is achieved. This guarantees that both transmission conditions in problems (equations (7.1) to (7.3)) will hold.

In order to ensure accurate and stable dynamic simulations of FSI problems dynamic and kinematic continuity should be guaranteed on the interaction interface for partitioned problems, monolithic schemes naturally satisfy these conditions. Kinematic and dynamic continuity require that displacements and tractions be continuous at the inter-

face respectively, energy conservation requires that both conditions be satisfied simultaneously [86]. There are various ways to avoid instabilities, like introducing viscous damping or fluid compressibility, see [54], but these options change the nature of the problem. One of the few solutions that preserve the original problem is the introduction of sub-iterations among the sub-domains and adaptive time-stepping of the interaction algorithm (which has proven to be beneficial used in monolithic coupling schemes [62] but has not been explored in the development of this dissertation). Regarding sub-iterations, these are dependent upon a relaxation coefficient that ensures interface compatibility which can be either chosen from careful study of the problem at hand (a tiresome method an often inefficient) or can be calculated through optimal algorithms automatically without any user input. In this respect, we have used a relaxation of the position and velocity of the interface boundary that the solid solver transmits to the fluid solver. We denote this position as $\mathbf{d}_{\Gamma_I}$; from it, one may compute the velocity of the fluid boundary and $\mathbf{u}_{\text{mesh}}$, as explained above. We have implemented an Aitken relaxation scheme, in particular Aitken Δ^2, detailed in [53] which is a reformulation from the algorithm initially proposed in [50], which we describe now in our context.

Within each time step, let us denote by a superscript k the k-th block-iteration of any variable. For clarity, let us omit the superscript with the time step counter. Suppose that from values at the k-th iteration, the solid is solved, obtaining the boundary displacements $\mathbf{d}_{\Gamma_I,\text{sl}}^{k+1}$. Then, the fluid is solved from the boundary displacements $\mathbf{d}_{\Gamma_I}^{k+1}$ computed as

$$\mathbf{d}_{\Gamma_I}^{k+1} = \mathbf{d}_{\Gamma_I}^{k} + \omega^{k+1}\mathbf{r}_{\Gamma_I}^{k+1}, \tag{8.1}$$

where

$$\mathbf{r}_{\Gamma_I}^{k+1} := \mathbf{d}_{\Gamma_I,\text{sl}}^{k+1} - \mathbf{d}_{\Gamma_I}^{k}, \tag{8.2}$$

$$\omega^{k+1} = -\omega^{k}\frac{(\mathbf{r}_{\Gamma_I}^{k})^{T}(\mathbf{r}_{\Gamma_I}^{k+1} - \mathbf{r}_{\Gamma_I}^{k})}{|\mathbf{r}_{\Gamma_I}^{k+1} - \mathbf{r}_{\Gamma_I}^{k}|^2}. \tag{8.3}$$

9 THE ALGORITHM

For a time interval between 0 and t_f, let n be the current time partition, n_{last} the last time step, i the current internal iteration of a particular sub-domain (fluid or solid), k the current coupling iteration for both domains, Tol_{time} the temporal tolerance (to decide whether the steady state has been reached or nor), Tol_{cou} the coupling tolerance between sub-domains, Tol_{sl} the internal tolerance for convergence for the solid sub-domain, and Tol_{fl} the internal tolerance for convergence for the fluid sub-domain. The FSI algorithm is displayed in Algorithm 1. For $i = 0$ (either for the fluid or for the solid) the unknowns are initialized to those of the previous block-iteration, whereas for $k = 0$ they are initialized to those of the previous time step.

Algorithm 1 General FSI algorithm: Part 1

Read case parameters and initialize values for the fluid and the solid domains
for $n = 1; n \leqslant n_{last}; n + 1$ **do**
  for $k = 1; k \leqslant k_{max}; k + 1$ **do**
    for $i = 1; i \leqslant i_{max}; i + 1$ **do**
      Solve the fluid problem for $[\mathbf{u}_h, p_h]^{i+1}$ from $\mathbf{u}_{mesh}^{k}$
      Calculate error $\epsilon_{\mathbf{u}}^{i+1} = \frac{|\mathbf{u}_h^{i+1} - \mathbf{u}_h^{i}|}{|\mathbf{u}_h^{i+1}|}$; $\epsilon_{p}^{i+1} = \frac{|p_h^{i+1} - p_h^{i}|}{|p_h^{i+1}|}$;
      if $\epsilon_{\mathbf{u}}^{i+1}$ and $\epsilon_{p}^{i+1} \leqslant Tol_{fl}$ **then**
        Non linearity converged; break non-linearity loop
      end if
    end for

Algorithm 1 General FSI algorithm: Part 2

Set $[\mathbf{u}_h, p_h]^{k+1} \leftarrow [\mathbf{u}_h, p_h]^{i+1}$
Calculate tractions $\mathbf{t}_{fl}^{k+1}$ on Γ_I (to be transmitted to the solid)
for $i = 1; i \leqslant i_{max}; i + 1$ **do**
Solve the solid problem for $\mathbf{d}_h^{i+1}$ from $\mathbf{t}_{fl}^{k+1}$
Calculate error $\epsilon_{\mathbf{d}}^{i+1} = \frac{|\mathbf{d}_h^{i+1} - \mathbf{d}_h^{i}|}{|\mathbf{d}_h^{i+1}|}$
if $\epsilon_{\mathbf{d}}^{i+1} \geqslant \mathrm{Tol}_{sl}$ **then**
Non linearity converged; break non-linearity loop
end if
end for
Set $\mathbf{d}_h^{k+1} \leftarrow \mathbf{d}_h^{i+1}$ and $\mathbf{d}_{\Gamma_I,sl}^{k+1}$ the values of $\mathbf{d}_h^{k+1}$ on Γ_I
Calculate the residual on the $\mathbf{r}_{\Gamma_I}^{k+1}$ from (8.2)
Calculate the relaxation parameter ω^{k+1} from (8.3)
Calculate the mesh interface movement $\mathbf{d}_{\Gamma_I}^{k+1} = \mathbf{d}_{\Gamma_I}^{k} + \omega^{k+1}\mathbf{r}_{\Gamma_I}^{k+1}$
Calculate the fluid mesh movement $\mathbf{d}_{mesh}^{k+1}$
and the fluid mesh velocity $\mathbf{u}_{mesh}^{k+1}$ from $\mathbf{d}_{\Gamma_I}^{k+1}$
Calculate the coupling error $\epsilon_{\mathbf{u}}^{k+1} = \frac{|\mathbf{u}_h^{k+1} - \mathbf{u}_h^{k}|}{|\mathbf{u}_h^{k+1}|}$;
$\epsilon_p^{k+1} = \frac{|p_h^{k+1} - p_h^{k}|}{|p_h^{k+1}|}$; $\epsilon_{\mathbf{d}}^{k+1} = \frac{|\mathbf{d}_h^{k+1} - \mathbf{d}_h^{k}|}{|\mathbf{d}_h^{k+1}|}$
if $\epsilon_{\mathbf{u}}^{k+1}$ and ϵ_p^{k+1} and $\epsilon_{\mathbf{d}}^{k+1}$ on $\Gamma_I \leqslant \mathrm{Tol}_{coup}$ **then**
Coupling converged; break coupling loop
end if
end for
Calculate temporal increment $\epsilon_{\mathbf{u}}^{n+1} = \frac{|\mathbf{u}_h^{n+1} - \mathbf{u}_h^{n}|}{|\mathbf{u}_h^{n+1}|}$;
$\epsilon_p^{n+1} = \frac{|p_h^{n+1} - p_h^{n}|}{|p_h^{n+1}|}$; $\epsilon_{\mathbf{d}}^{n+1} = \frac{|\mathbf{d}_h^{n+1} - \mathbf{d}_h^{n}|}{|\mathbf{d}_h^{n+1}|}$
if $\epsilon_{\mathbf{u}}^{n+1}$ and ϵ_p^{n+1} and $\epsilon_{\mathbf{d}}^{n+1} \leqslant \mathrm{Tol}_{time}$ **then**
Stationary state achieved; break temporal loop
end if
end for
Finalize case
Output if necessary

Part IV

REDUCED ORDER MODELS

REDUCED ORDER MODELS

Possibly the major drawback of numerical simulation of complex physical phenomena, in our case coupled interaction between sub-domains, is the long solution times due to the great number of degrees of freedom necessary to accurately represent a specific problem. To this end reduced order modeling was developed where the idea is to reproduce the input-output behavior of a problem while reducing drastically the degrees of freedom that compose it.

As discussed in Chapter 8, strongly coupled partitioned Fluid-Structure Interaction (FSI) algorithms may require a high number of sub-iterations and sub-relaxation, making the problem potentially expensive numerically and consequently taking a long time to achieve a solution. In this sense, the development of model order reduction schemes that increase performance while maintaining output accuracy is of interest. Herein lies our motivation to introduce Reduced Order Model (ROM) into FSI. In this section we give a short review of the methodology we apply and the algorithmic aspects that concern it.

It is however convenient to give a wider framework for our proposed ROM strategy. As mentioned earlier, the stabilization of the reduced space problem is not a new field of research. Particularly of interest is [10] where the concept of an inf-sup compatible ROM formulation is introduced by the addition of supremizer terms to the reduced formulation. The supremizer serves as a restriction to the reduced system to enforce incompressibility in the process adding new degrees of freedom. It is seen that solving exactly for the exact supremizer during the online stage becomes unfeasible so the recommended approach is to actually develop this calculation offline, apply Proper Orthogonal Decomposition (POD), obtain a base for the supremizer

unknowns and treat it as any other reduced variable. The authors achieve a stable ROM by the addition of a few supremizer terms into the system. Later [79] would develop this idea into the field of FSI by adding VMS stabilization into the reduced space for the fluid, similar to what had previously been done by [67], the main difference being when and where the stabilization is carried out. The author's approach is to differentiate between a projected stabilized ROM (consistent) and a non stabilized one (non-consistent). While both methods have the same offline phase, the online phase is critically different. The conclusion is that the consistent ROM is more accurate than its counterparts (consistent enriched by means of supremizers and non-consistent).
In the context of ROM, there is also the possibility to choose between a purely monolithic approach, as in [11, 43], or a partitioned scheme iterated to achieve strong coupling, as in [51, 85, 87]; this last option is adopted in some applications and large scale calculations, as in [88] or the pioneering work [58], in which a complete aircraft is modeled.
For all the formulations for each field (solid or fluid) to be described, we use the Variational Multi-Scale (VMS) approach to design stabilized formulations [32, 48], assuming that the Full Order Model (Full Order Model (FOM)) is a Finite Element (FE) method. As a distinctive feature of this work, we use the same VMS formulation for the ROM as for the FOM, an idea introduced in [67] and later expanded in [66]. This formulation uses dynamic and orthogonal sub-scales (see [30, 34]), properties that we found crucial for the success of our approach. Other attempts to employ VMS ideas in the ROM context can be found in [8, 49, 79].

10 THEORY AND NOTATION

Let us define a high dimensional space $\mathcal{Y}_h$ of dimension M, with $\boldsymbol{\varphi} = \{\boldsymbol{\varphi}^1, \ldots, \boldsymbol{\varphi}^M\}$ its orthonormal basis, whose elements are vectors of D components. Then any element $\mathbf{y}_h \in \mathcal{Y}_h$ can be written as the linear combination $\mathbf{y}_h = \sum_{k=1}^{M} (\mathbf{y}_h, \boldsymbol{\varphi}^k)\boldsymbol{\varphi}^k$, now with $(\cdot,\cdot)$ the L^2-inner product in $\mathcal{Y}_h$. We can also define a low-dimensional subspace $\mathcal{Y}_{rom} \subset \mathcal{Y}_h$ of dimension m, which approximates $\mathcal{Y}_h$ as $m \to M$, with a basis $\boldsymbol{\Phi} = \{\boldsymbol{\Phi}^1, \ldots, \boldsymbol{\Phi}^m\}$. Using this basis, we can approximate any element $\mathbf{y}_h$ as $\mathbf{y}_h \approx \mathbf{y}_{rom} = \sum_{k=1}^{m} \boldsymbol{\Phi}^k a^k$, where a^k is the k-th coefficient which can be computed as $a^k = (\mathbf{y}_h, \boldsymbol{\Phi}^k)$, and which will typically be obtained from the solution of the reduced problem. The accuracy of the approximation depends on how well the basis $\boldsymbol{\Phi}$ approximates the exact basis $\boldsymbol{\varphi}$, as we use a nested basis scheme, a finer basis includes the previous one within its space, we can assume that finer basis indeed will approximate the full order base.

10.1 CONSTRUCTION OF THE BASIS

The method we use to construct the basis of the low-dimensional space is the POD. The objective of this method is finding a basis from a collection of high-fidelity "snapshots", which in our context are solutions in $\mathcal{Y}_h$ of an evolution problem at certain time steps. As it is well known, we need to substract the mean. Thus, taking a set of data as a collection of N snapshots $\{\mathbf{s}_j\}_{j=1}^N = \{\mathbf{y}_{h,j} - \bar{\mathbf{y}}_h\}_{j=1}^N$, the overbar

denoting the mean of the $y_{h,j} \in \mathcal{Y}_h$, we can reproduce any element of this collection as

$$y_{h,j} \approx \bar{y}_h + \sum_{k=1}^{m} (s_j, \phi^k)\phi^k, \tag{10.1}$$

where, in the case of POD, $\{\phi^k\}_{k=1}^m$ is an orthonormal system of $\mathcal{Y}_h$. The POD consists in finding the orthonormal basis $\{\phi^k\}_{k=1}^m$ of $\mathcal{Y}_{rom}$ such that:

$$\min_{\{\phi\}_{k=1}^m} \quad \frac{1}{N}\sum_{j=1}^{N} \left\| s_j - \sum_{k=1}^{m} (s_j, \phi^k)\phi^k \right\|^2,$$
$$\text{subject to } (\phi^i, \phi^j) = \delta_{ij}, \quad 1 \leqslant i, j \leqslant m, \tag{10.2}$$

where $\|\cdot\|$ denotes the L^2 norm. By means of a Singular Value Decomposition (SVD) we can solve for the basis $\{\phi^k\}_{k=1}^m$ from the matrix of snapshots. This basis depends on parameters such as time-step, how often the snapshots were acquired and the reproducibility of the function being analyzed. A reduced basis can be defined by truncating the left singular-vectors at the m-th column. As a criterion for the truncation, we use the retained energy η, defined in [78] as:

$$\eta = \frac{\sum_{k=1}^{m} \lambda^k}{\sum_{k=1}^{M} \lambda^k}, \tag{10.3}$$

where $\{\lambda^k\}_{k=1}^M$ are the singular values of the SVD. The SVD produces a diagonal matrix which contains, from greatest to smallest, the eigenvalues of the associated (singular) eigen-vectors. The ordering of the eigenvalues is a measure of the relative importance of each of the basis functions in the whole system. In general, in a reducible problem (a problem that should be easily reproduced by means of ROM) they decrease quickly in magnitude. If m is sufficiently small, the time to compute the reduced system is minimal.

The stage of the problem in which the basis is calculated is termed as the off-line phase.

Remark. *The snapshots are arrays of M components, and therefore the vectors of the ROM basis are also arrays of M components. In our finite element context, however, we may identify them as piecewise polynomial functions. Indeed, if $\phi^{k,a}$ is the a-th component of the k-th basis vector, $a = 1, \dots, M$, we may identify $\boldsymbol{\phi}^k$ with the function*

$$\phi^k(\mathbf{x}) = \sum_{a=1}^{M} N^a(\mathbf{x})\phi^{k,a}, \ k = 1, \dots, m,$$

where $\mathbf{x}$ is the position vector and $N^a(\mathbf{x})$ the finite element interpolation function of the a-th degree of freedom. Therefore, $\mathcal{Y}_{rom}$ can be identified as a space of functions of dimension m.

In the case of FSI problems, the construction of the basis can be done in a variety of ways, as shown in [6] for domain decomposition problems. In our case, and as a first approach, it was decided to assemble and calculate the snapshots of each sub-domain separately, this is, the basis for the fluid domain from the snapshots of velocity and pressure in the fluid ($\boldsymbol{\phi}_{fl}(\mathbf{u}_h, p_h)$) and the basis for the solid domain from the the snapshots of displacements ($\boldsymbol{\phi}_{sl}(\mathbf{d}_h)$). However, it is also possible to construct and assemble just one basis from the joint snapshots of velocity, pressure and displacement ($\boldsymbol{\phi}_{fl,s}(\mathbf{u}_h, p_h, \mathbf{d}_h)$); the performance of this option is left for future study (see [6] for further details).

11 VMS-ROM

In FSI problems and with the partitioned strategy we have followed, we have to solve one variational problem in the fluid domain and another one in the solid domain. The Galerkin finite element approximation to these problems can be stated as these variational problems restricted to the finite element spaces, both for the unknowns and for the test functions. In a similar way, the ROM could be expressed as the same variational problems, now restricting unknowns and test functions to the ROM spaces, with a much smaller dimension than the finite element spaces. There are other options to state the ROM problem, but the approach described justifies that one may expect similar instability problems for the Galerkin finite element method and the described Galerkin-ROM. Therefore, some sort of numerical stabilization will be required for both fluid and solid problem, excluding the irreducible problem in the latter as the Galerkin method yields a stable and accurate approximation.

The approach we shall follow is the same as for the finite element problem, namely, to use a VMS method with an approximation to the sub-grid scales similar to that given by (5.6). In the ROM case, it is particularly natural to use *orthogonal* sub-grid scales, since the vectors of the basis are mutually orthogonal. Therefore, if the ROM space is obtained by truncating the vectors obtained from a SVD of the collection of snapshots to the first m members, the space of sub-grid scales is simply its L^2-orthogonal complement.

Let $y_{rom} \equiv [u_{rom}, p_{rom}] :]0, t_f[\longrightarrow \mathcal{Y}_{rom}$ and $z_{rom} \equiv [v_{rom}, q_{rom}] \in \mathcal{Y}_{rom}$ be the ROM unknown and test functions of the fluid problem, respectively, where $\mathcal{Y}_{rom}$ is the velocity-pressure pair obtained from the POD basis

(using its interpretation as a function space described in Remark 10.1). According to the previous considerations, and using the BDF2 scheme for the time discretization, the problem we have to solve for the fluid ROM for example is:

$$
\begin{aligned}
&(\rho_{fl}\delta_{2,t}\mathbf{u}_{rom}^{n+1}, \boldsymbol{v}_{rom}) + B(\mathbf{y}_{rom}^{n+1}, \boldsymbol{z}_{rom}) \\
&\quad + \sum_{K} \left\langle \breve{\mathbf{u}}^{n+1}, \rho_{fl}\mathbf{u}_{rom}^{n+1} \cdot \nabla \boldsymbol{v}_{rom} + \mu_{fl}\Delta \boldsymbol{v}_{rom} + \nabla q_{rom} \right\rangle_{K} \\
&\quad - \sum_{K} \left\langle \breve{p}^{n+1}, \nabla \cdot \boldsymbol{v}_{rom} \right\rangle_{K} = L(\boldsymbol{z}_{rom}),
\end{aligned}
\tag{11.1}
$$

where $\breve{\mathbf{u}}^{n+1}$ and $\breve{p}^{n+1}$ are the solution of

$$
\frac{\rho_{fl}}{\Delta t}\left(\breve{\mathbf{u}}^{n+1} - \breve{\mathbf{u}}^{n}\right) + \frac{1}{\tau_1}\breve{\mathbf{u}}^{n+1} = \Pi_{rom}^{\perp}\left(\mathbf{r}\left(\mathbf{y}_{rom}^{n+1}\right)\right), \tag{11.2}
$$

$$
\frac{1}{\tau_2}\breve{p}^{n+1} = -\Pi_{rom}^{\perp}\left(\nabla \cdot \mathbf{u}_{rom}^{n+1}\right), \tag{11.3}
$$

within each element domain K of the finite element partition of the fluid domain, with

$$
\mathbf{r}\left(\mathbf{y}_{rom}^{n+1}\right) = \rho_{fl}\delta_{2,t}\mathbf{u}_{rom}^{n+1} - \mu_{fl}\Delta\mathbf{u}_{rom}^{n+1} + \rho_{fl}\mathbf{u}_{rom}^{n+1} \cdot \nabla\mathbf{u}_{rom}^{n+1} + \nabla p_{rom}^{n+1} - \rho_{fl}\mathbf{f}^{n+1},
$$

and the stabilization parameters computed as in (5.8)-(5.9), replacing $\mathbf{u}_h$ by $\mathbf{u}_{rom}$ in the former. In (11.2)-(11.3), $\Pi_{rom}^{\perp} = I - \Pi_{rom}$, where Π_{rom} is the L^2-projection onto the appropriate ROM space (of velocities or of pressures). The development previously shown is for a two field incompressible Navier-Stokes fluid problem but the concept is exactly the same for any field problem previously detailed in past chapters.

Remark. *Note that we make use of the finite element partition, both in problem (11.1) and in the definition of the stabilization parameters. This is possible because the ROM basis vectors can be understood as piecewise polynomial functions defined on each element of the partition (see Remark 10.1).*

Remark. *Contrary to [8], the space where the subscales belong is directly L^2-orthogonal to the ROM space, whereas in the cited reference it is a subspace of the finite element space.*

As a concluding remark to this section we would like to address our choice of not using modal analysis based methods, which is usually the norm in ROM for solids. It is clear that fluid flow is impossible to be represented via this kind of eigenvalue decomposition, specially for the highly non-linear nature of the flows we are interested in. Even though it is possible to represent the non-linearities present in structural dynamics by modal analysis, as it is mentioned in [82], a basis calculated by this approach needs to be recalculated every so often to guarantee that the solution will reproduce accurately non-linear behavior. Our approach focuses on the idea of “one-for-all" methodology, where by means of one robust formulation any kind of problem can be represented. In conclusion, we apply the same form of decomposition (namely, POD) to both the fluid and the structure.

11.1 A WORD ON ERROR MEASUREMENT

We apply the Root-Mean-Square Deviation (RMSD) to compare results obtained with the ROM to those obtained with the FOM. This way of measuring error is helpful because it shows ‘how far’ the solution is from our full order solution. In this way results presented here are not to be analyzed as a convergence of the method but rather as how well the reduced results reproduce the desired full order problem. The expression for the RMSD is given as:

$$\text{RMSD} = \sqrt{\frac{1}{S}\sum_{j=1}^{S}\left|y_{\text{ROM}}^{j} - y_{\text{FOM}}^{j}\right|^{2}},$$

where y_{ROM}^{j} and y_{FOM}^{j} are the variable that we want to compare in ROM and FOM, respectively, either in the fluid or in the solid, evaluated at time step j, S being the total number of time steps used for comparison.

12 THE ALGORITHM

We describe next the algorithm to solve FSI problems using ROM for both the fluid and the solid, which we denote as ROM-ROM algorithm. However, we first describe the modifications that need to be done in the full order model, that we denote FOM-FOM algorithm, to obtain the necessary data for the ROM-ROM case.

12.1 FOM-FOM CASE

Algorithm 2, essentially the same as in algorithm 1 but with minor differences, corresponds to the off-line phase of a simulation case. We make use of all variables and parameters previously defined and add Φ_{fl} and Φ_{si}; these are the fluid and solid basis, respectively. The dots represent the parts that are the same as in algorithm 1.

Remark. *This process is most efficiently done taking full advantage of parallel solving, both for the FOM and ROM versions of the case. This means that the basis can be calculated and written to disk in parallel as well.*

12.2 ROM-ROM CASE

Algorithm 3 shows the ROM phase for the coupled problem, also known as the on-line phase. We make use of all the parameters defined in Section 12.1 and add $[\bar{u}, \bar{p}, \bar{d}]$, which are the snapshot mean values for the fluid and solid unkwnons (velocity-pressure and displacements).

Algorithm 2 FOM-FOM algorithm previous to a ROM-ROM calculation

Read case parameters and initialize values for fluid and solid domains, number of snapshots to take and parameters for the SVD solver
for $n = 1; n \leqslant n_{last}; n + 1$ **do**
  for $k = 1; k \leqslant k_{max}; k + 1$ **do**
    ...
    for $i = 1; i \leqslant i_{max}; i + 1$ **do**
      Solve fluid domain ...
    end for
    for $i = 1; i \leqslant i_{max}; i + 1$ **do**
      Solve solid domain ...
    end for
    ...
    if $\epsilon^{k+1}_{y_{fl,sl}}$ on $\Gamma_I \leqslant Tol_{coup}$ **then**
      Store snapshot of y^{n+1}_{fl} if required
      Store snapshot of y^{n+1}_{sl} if required
      Coupling converged; Break Coupling loop
    end if
  end for
  ...
end for
Finalize case
Calculate bases Φ_{fl}, Φ_{sl} by solving problem (10.2)
Output if necessary

In essence, it is the same as Algorithm 1 replacing finite element unknowns by ROM unknowns.

It can be seen, from the non-linearity of our operators in both fluid and solid domains, that at the reduced level it is necessary to still assemble the linear system of unknowns to preserve the efficiency and accuracy of the method; this is a costly procedure as it involves the whole array of unknowns and in general it is not scalable. Therefore it is generally critical to think about hyper-reduction as a means to placate this issue by means of selection of critical points which represent the main part of our domain. Such an approach can be termed hyper-reduction and there are various available techniques like Gappy-POD [17], APHR [71] or GNAT method to name a few [18]; an alternative is the recently proposed hyper-reduction by means of adaptive mesh refinement [66]. However our goal is of preliminary investigation on our Field to Field (F2F) FSI-ROM scheme, and no hyper-reduction has been used in the numerical examples presented in part v.

Algorithm 3 ROM-ROM algorithm: Part 1

Read case parameters and initialize values for fluid and solid domains

Initialize Fluid problem: read previously calculated reduced basis Φ_{fl}, and select the desired amount of basis vectors through any criteriom (energy for example).

Initialize Solid problem: read previously calculated reduced basis Φ_{sl}, and select the desired amount of basis vectors through any criteriom (energy for example).

for $n = 1; n \leqslant n_{last}; n + 1$ **do**

  for $k = 1; k \leqslant k_{max}; k + 1$ **do**

    for $i = 1; i \leqslant i_{max}; i + 1$ **do**

      Write $[y_{fl,rom}]^{i+1}$ in terms of Φ_{fl} and $[\bar{y}_{fl}]$

      Solve the fluid problem for $[y_{fl,rom}]^{i+1}$ from u^{k}_{mesh}

      Calculate error $\epsilon^{i+1}_{y_{fl}} = \frac{|y^{i+1}_{fl,rom} - y^{i}_{fl,rom}|}{|y^{i+1}_{fl,rom}|}$

      if $\epsilon^{i+1}_{y_{fl}} \leqslant Tol_{fl}$ **then**

        Non linearity converged; break non-linearity loop

      end if

    end for

    Set $[y_{fl;rom}]^{k+1} \leftarrow [y_{fl;rom}]^{i+1}$

    Calculate tractions t^{k+1}_{fl} on Γ_I (to be transmitted to the solid)

    for $i = 1; i \leqslant i_{max}; i + 1$ **do**

      Write $y^{i+1}_{sl;rom}$ in terms of Φ_{sl} and $\bar{y}_{sl}$

      Solve the solid problem for $y^{i+1}_{sl;rom}$ from t^{k+1}_{fl}

      Calculate error $\epsilon^{i+1}_{y_{sl}} = \frac{|y^{i+1}_{sl;rom} - y^{i}_{sl;rom}|}{|y^{i+1}_{sl;rom}|}$

      if $\epsilon^{i+1}_{y_{sl}} \geqslant Tol_{sl}$ **then**

        Non linearity converged; break non-linearity loop

      end if

    end for

Algorithm 3 ROM-ROM algorithm: Part 2

Set $\mathbf{d}_{\text{rom}}^{k+1} \leftarrow \mathbf{d}_{\text{rom}}^{i+1}$ and $\mathbf{d}_{\Gamma_I,\text{sl}}^{k+1}$ the values of $\mathbf{d}_{\text{rom}}^{k+1}$ on Γ_I

Calculate the residual on the $\mathbf{r}_{\Gamma_I}^{k+1}$ from (8.2)

Calculate relaxation parameter ω^{k+1} from (8.3)

Calculate mesh interface movement $\mathbf{d}_{\Gamma_I}^{k+1} = \mathbf{d}_{\Gamma_I}^{k} + \omega^{k+1}\mathbf{r}_{\Gamma_I}^{k+1}$

Calculate the fluid mesh movement $\mathbf{d}_{\text{mesh}}^{k+1}$ and fluid mesh velocity $\mathbf{u}_{\text{mesh}}^{k+1}$ from $\mathbf{d}_{\Gamma_I}^{k+1}$

Calculate coupling error $\epsilon_{\mathbf{y}_{\text{fl,sl}}}^{k+1} = \frac{|\mathbf{y}_{\text{fl,sl;rom}}^{k+1} - \mathbf{y}_{\text{fl,sl;rom}}^{k}|}{|\mathbf{y}_{\text{fl,sl;rom}}^{k+1}|}$

if $\epsilon_{\mathbf{y}_{\text{fl,sl}}}^{k+1}$ on $\Gamma_I \leqslant \text{Tol}_{\text{coup}}$ **then**

Coupling converged; break coupling loop

end if

end for

Calculate temporal increment $\epsilon_{\mathbf{y}_{\text{fl,sl}}}^{n+1} = \frac{|\mathbf{y}_{\text{fl,sl;rom}}^{n+1} - \mathbf{y}_{\text{fl,sl;rom}}^{n}|}{|\mathbf{y}_{\text{fl,sl;rom}}^{n+1}|}$;

if $\epsilon_{\mathbf{y}_{\text{fl,sl}}}^{n+1} \leqslant \text{Tol}_{\text{time}}$ **then**

Stationary state achieved; break temporal loop

end if

end for

Finalize case

Output if necessary

Part V

TESTING THE THEORY

13 NUMERICAL EXAMPLES

In this section we explore the various numerical examples analyzed during the development of this project. The examples are organized as follows: first numerical benchmarks for the solid formulations developed will be shown, then 2D Fluid-Structure Interaction (FSI) examples and lastly some 3D examples. The idea is to increase progressively the complexity towards more numerically challenging test cases.

13.1 COOK'S MEMBRANE

The following example is a typical benchmark for solid mechanics. A tapered beam is subjected to a shearing load on one of its sides. In our case the shear traction is taken as 30 GN. Figure 13.1 shows the geometry of the beam.

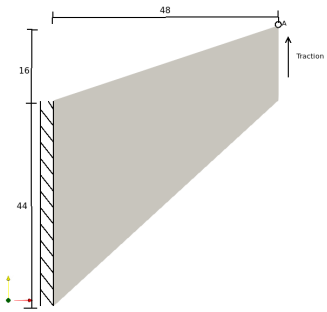

Figure 13.1: Geometry

The properties of the material for all tests in this benchmark are shown in table 13.1. For the irreducible formulation the Poisson coefficient was taken as $\nu = 0.49$, so as to have a material with low compressibility but without locking. For the three-field formulation we deal with an incompressible material ($\nu = 0.5$).

ρ_{sl}	7850.0 [Kg/m^3]
μ_{sl}	80×10^9 [Pa]
λ_{sl}	∞
Model	Neo-Hookean

Table 13.1: Physical parameters

Convergence tests were run for different mesh sizes. Figures 13.2a and 13.2b show examples for quadrilateral (4 node bilinear) and triangular (3 node linear) elements. The notation for the results is detailed in table 13.2.

Name	Formulation	Type of elem
irr_tri	irreducible	linear triangle
irr_sq	irreducible	bi-linear square
sup_tri	three-field	linear triangle
sup_sq	three-field	bi-linear square

Table 13.2: Case parameters

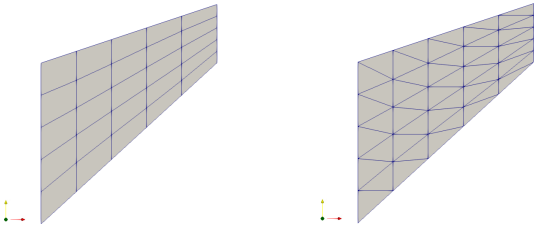

(a) Quad mesh (b) Triangle mesh

Figure 13.2: Mesh examples for benchmark

As it is a bending dominated test, it is of interest to see the displacement at the tip of the beam (point A) both in x and y directions. Figure 13.3 shows the convergence for different mesh sizes in comparison with a solution obtained with a very fine mesh, shown in black.

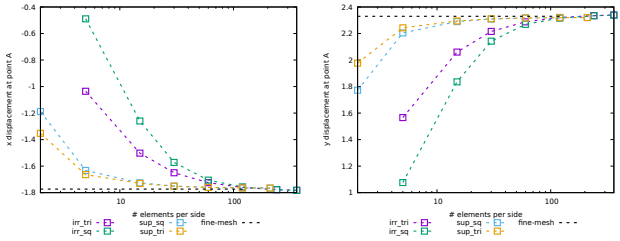

(a) Displacement in x axis (b) Displacement in y axis

Figure 13.3: Displacement of point A

Figure 13.4 shows the evolution of the error for the results shown previously in terms of number of elements; it can be seen that the convergence for the three-field is better, although a fairer comparison can be seen from figure 13.5, which shows error in terms of number of DOFs. Results are in agreement with [27], keeping in mind that their results are shown for the linear case. Both the irreducible and the three-field formulation show good convergence upon mesh refinement, with the three-field model being more precise and having faster

convergence overall. For the three-field formulation, bi-linear square elements and triangular elements show very similar convergence properties; however, in the irreducible case triangular elements appear to be more precise than squares.

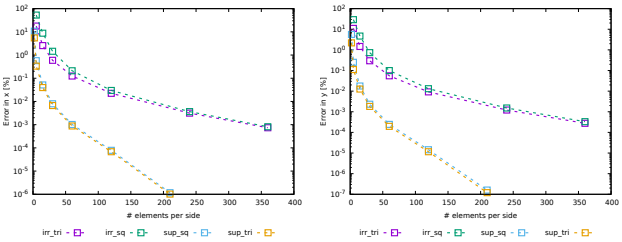

(a) Error in x axis (b) Error in y axis

Figure 13.4: Error for displacement at point A according to # of elements

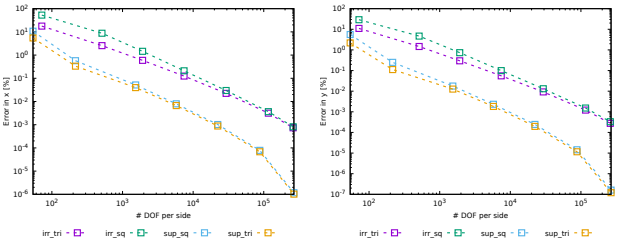

(a) Error in x axis (b) Error in y axis

Figure 13.5: Error for displacement at point A according to # of DOF

Figure 13.6 shows the stress and pressure distribution for the beam using the three-field formulation. It can be seen that smooth and continuous fields have been obtained, without any oscillation in spite of using equal interpolation for all fields.

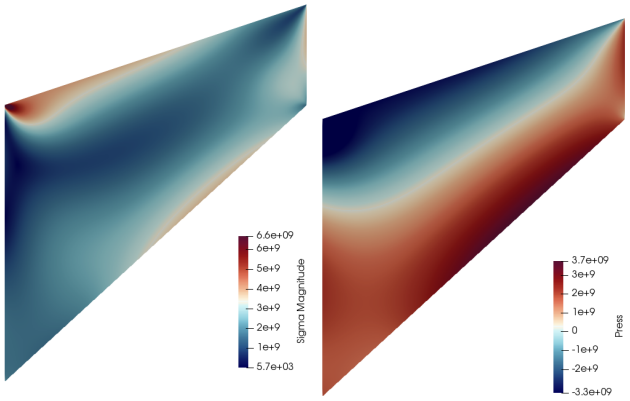

(a) Deviatoric stress magnitude contours

(b) Pressure contours

Figure 13.6: Deviatoric stress and pressure

13.2 DYNAMIC OSCILLATION OF A CANTILEVER BAR

In this section we analyze to test cases for the time evolution of a clamped beam under the effect of gravity. In both cases we compare results against the ones obtained by means of the irreducible formulation.

13.2.1 *Three-field dynamic benchmarking*

Figure 13.7 shows the geometry of the beam and an example of a mesh used. For the initial conditions, the bar starts at rest and then suddenly gravity is applied, so the bar falls in the direction shown.

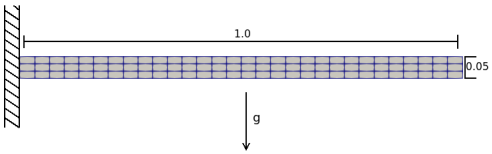

Figure 13.7: Geometry

The properties of the material and parameters for all tests in this benchmark are shown in table 13.3. Note that for the irreducible formulation the Poisson coefficient was taken as $\nu = 0.499$, whereas for the three-field formulation we deal with an incompressible material. The time interval of analysis is $[0, 1]$, with a time step $\delta t = 10^{-3}$.

ρ_{sl}	100.0 [Kg/m^3]
μ_{sl}	2.135×10^7 [Pa]
λ_{sl}	∞
Model	Neo-Hookean
Gravity	2.0[m/s^2]

Table 13.3: Physical parameters

Name	formulation	# elems:	(length)	(height)	type
30_3	three-field		30	3	lin
30_3_irr	irreducible		30	3	lin
80_8_irr	irreducible		80	8	lin
quad_30_3	three-field		30	3	quad
quad_30_3_irr	irreducible		30	3	quad
quad_80_8	three-field		80	8	quad

Table 13.4: Case parameters

Figure 13.8 shows the time evolution of the displacements for different cases run. Solutions were compared for both the three-field and the irreducible formulation for different mesh sizes and elements, linear (lin) or quadratic (quad), only squares were used in this example. The notation for the results is detailed in table 13.4, all elements used are squares.

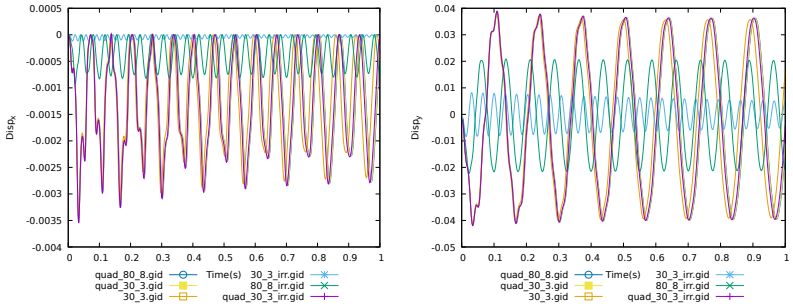

(a) Displacement in x

(b) Displacement in y

Figure 13.8: Displacement at the tip of the beam

Observe from figure 13.8 that there are marked differences between the two formulations for a dynamic case. This is better seen in figure 13.9, which shows a zoom of a portion of the time interval. The three-field formulation approximates a much finer reference solution obtained with linear elements, while the irreducible one is over-diffusive both in

time and space. When quadratic elements are used, the irreducible formulation performs more accurately but the three-field is always more precise, in conserving both phase and amplitude.

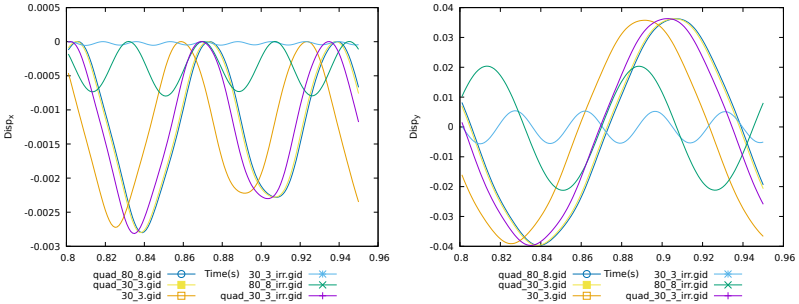

(a) Displacement in x (b) Displacement in y

Figure 13.9: Zoom of displacement at the tip of the beam

13.2.2 *ROM*

This test is a rather simple one in which the purpose is to assess the behavior of all three solid formulations (one, two and three-field approaches), comparing first the Full Order Model (FOM) and then the Reduced Order Model (ROM). The test consists of a cantilevered bar subject to the force of gravity, being initially undeformed at rest. Only a short interval of the oscillation will be analyzed. The geometry and initial position of the bar are shown in figure 13.10, the physical parameters of the bar are given in table 13.5, where ν_{sl} is Poisson's coefficient, and the legend for the results is given in table 13.6.

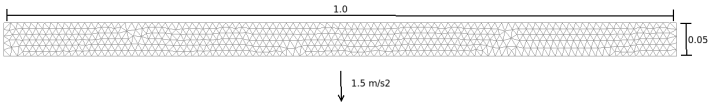

Figure 13.10: Geometry

ρ_{sl}	1000.0 [Kg/m^3]
μ_{sl}	1.93 10^6 [Pa]
ν_{sl}	0.4
Model	Neo-Hookean

Table 13.5: Physical parameters

Name	Formulation	Space	Energy(%)
irr_fom	Irreducible	FOM	
up_fom	Two-field	FOM	
sup_fom	Three-field	FOM	
irr_r9e5	Irreducible	ROM	99.999
irr_r9e6	Irreducible	ROM	99.9999
up_r9e4	Two-field	ROM	99.99
up_r9e5	Two-field	ROM	99.999
up_r9e6	Two-field	ROM	99.9999
sup_r9e3	Three-field	ROM	99.9
sup_r9e4	Three-field	ROM	99.99

Table 13.6: Case parameters

The FE mesh employed consists of 2278 linear elements in all cases and 1290 nodal points. Thus, the number of degrees of freedom is different for the three formulations, although we know from the previous test that the increase in the number of degrees of freedom of the three-field formulation pays-off, i.e., it shows more accurate

results for the same number of degrees of freedom. Here we only wish to compare the three formulations for a given mesh. The time step employed in all cases is $\delta t = 0.001$.

Figure 13.11 and 13.12 show the displacement and acceleration at the tip of the beam, respectively. In these results only a portion of the transient is shown to see the behavior of each formulation. It is instructive to analyze these results because it is seen that all formulations behave in a very similar way. The three-field is the most precise as was previously shown and the two-field falls in the middle between the irreducible and three-field, as was also expected. The results labeled 'fine_mesh' were taken with a very fine mesh with quadratic elements for the irreducible formulation; upon mesh refinement all formulations converge to this results.

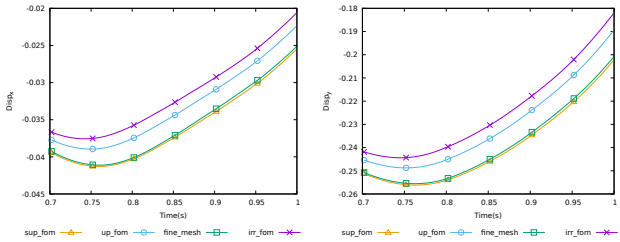

(a) Displacement in x axis (b) Displacement in y axis

Figure 13.11: Displacement at the tip of the beam

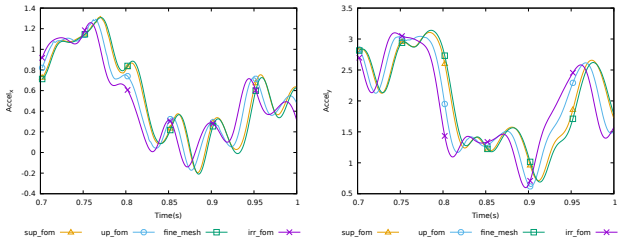

(a) Acceleration in x axis (b) Acceleration in y axis

Figure 13.12: Acceleration at the tip of the beam

The next series of results show the behaviour of each of the formulations compared to their respective ROM counterparts, each one with different amount of energy. The purpose of this set of results is to validate the FOM–ROM behavior to be able to confidently give the step to full FSI–FOM–ROM. Note that all ROM results reproduce its FOM counterpart fairly well. The irreducible FOM-ROM, shown in Fig. 13.13, is the formulation that requires the highest amount of energy, above 99.999%, to show comparable precision with its two other counterparts. The two-field, shown in Fig. 13.14, is as expected in between the one-field and the three field, with a minimum energy requirement of 99.99%. Finally the three-field, shown in Fig. 13.15, requires only 99.9% of energy to obtain ROM results comparable to the FOM ones.

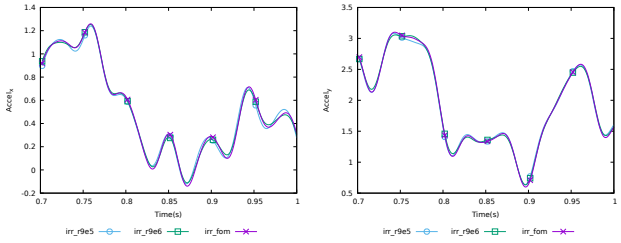

(a) Acceleration in x axis (b) Acceleration in y axis

Figure 13.13: Acceleration at the tip of the beam, FOM–ROM irreducible

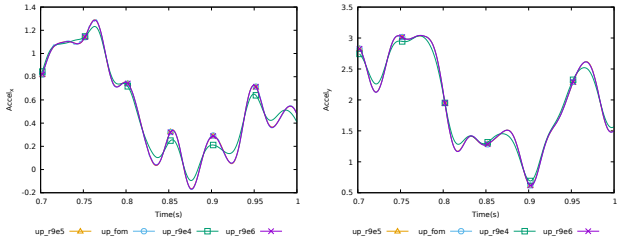

(a) Acceleration in x axis (b) Acceleration in y axis

Figure 13.14: Acceleration at the tip of the beam, FOM–ROM, two fields (UP)

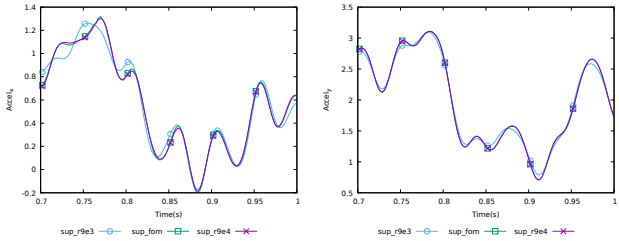

(a) Acceleration in x axis (b) Acceleration in y axis

Figure 13.15: Acceleration at the tip of the beam, FOM–ROM, three fields (SUP)

It is worthwhile to analyze the contour plots shown in Fig. 13.16, as they show the large difference between the basis of each of the formulations. One key aspect is noting that while not much can be said for the basis of the irreducible formulation, shown in Fig. 13.16a, and the two-field, shown in Fig. 13.16b, each of the modes are clearly apparent in the basis of the three-field problem, shown in Fig. 13.16c; this points to the more successful reduction of the problem with the three-field approach, conclusion that is supported by the results.

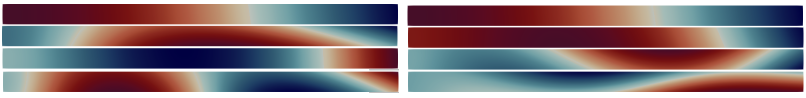

(a) IRR (b) UP

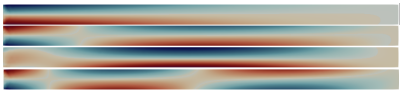

(c) SUP

Figure 13.16: Basis contours for the displacement in y for IRR, UP and SUP

13.3 FLOW AROUND A CYLINDER WITH SUPPORTED FLAG

The following example reproduces the benchmark presented in [83], where a fluid flows around a cylinder with a supported flag. The fluid flows from the left wall and the tractions of the fluid onto the solid initiate the flag motion. After a while this motion is significant enough to move the fluid around it, starting a feedback loop between fluid and solid. The test conditions are shown in Table 13.7.

	Fluid		Solid
ρ_{fl}	1,000.0	ρ_{sl}	10,000.0
μ_{fl}	0.001	μ_{sl}	$0.5 \cdot 10^6$
		λ_{sl}	$2.0 \cdot 10^6$
Model	Newtonian		St.Venant-Kirchoff

Table 13.7: Physical parameters

Figures 13.17 and 13.18 show the geometry and the finite element mesh used in this example. Note that the solid and fluid meshes are non-conforming, making the use of interpolation between sub-domains necessary as discussed in Chapter 8. The length of the fluid domain is $L = 2.5$, its height $H = 0.41$, and the radius of the cylinder is $R = 0.05$. The length of the bar is $l = 0.35$ and its thickness $h = 0.02$.

Figure 13.17: Geometry

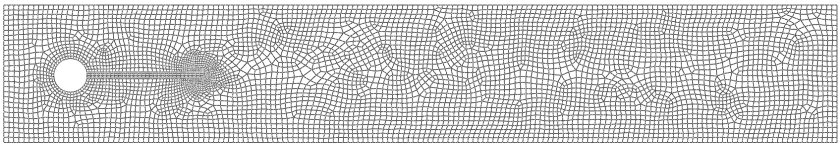

Figure 13.18: Non-conforming mesh

Figure 13.19 shows a zoom for the cylinder and bar.

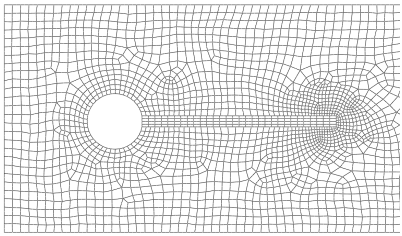

Figure 13.19: Non-conforming mesh - zoom

Tables 13.8 and 13.9 show important mesh parameters and boundary conditions, respectively.

	Fluid	Solid
Element type	Quadratic quads	Quadratic quads
Nodes per element	9	9
# elements	5,531	500
# nodes	22,642	2,211

Table 13.8: Mesh parameters

	Fluid	Solid
$x = 0$:	$u_x = 35.693\, y(0.41 - y)$, $u_y = 0.0$	
$y = 0, H$:	Free slip	
$x = L$:	Free (zero traction)	
Cylinder boundary:	No slip	
Flag boundary:	Solid velocity	Fluid tractions
Flag-cylinder union:		$d_x = d_y = 0$

Table 13.9: Boundary conditions

Out of experimentation it was found that ROM results that accurately represent the full order model are obtained when 99.999999% of the energy of the fluid is taken, amounting to 163 basis vectors, and 99.999999% of the energy of the solid is taken, amounting to 48 basis vectors. From the results it can be seen that if fewer modes are retained the ROM solution starts to deviate from the FOM, this can be seen as well in the spectrum decay of the results. In the same way as previously described, when fewer modes are used the low energy high frequency modes are not approximated correctly and noise is generated in that part of the spectrum, see for example figure 13.30 and the discussion at the end of this section. Results for a basis using 99.9999% of the energy are also shown in the following, in this case using 158 basis vectors for the fluid and 16 for the solid.

Notice that from Table 13.8 it can be calculated that for the fluid problem the amount of DOF is 67,926 while for the solid it is 4,422. For the reduced problem we have 163 DOF for the fluid and 48 for the solid. This means that overall in terms of DOF we are achieving a reduction of 99.76% for the fluid and 98.91% for the solid, for a total reduction of 99.71%.

Figures 13.20 to 13.23 show contours for velocity and pressure, for both the reduced order problem and the full order problem at the last time of the simulation, $t = 1.2$. After this, graphs of significant quantities are compared for both the reduced and full order problems.

Figures 13.20 and 13.21 show velocity contours, Figures 13.22 and 13.23 show pressure contours, and Figure 13.23 shows the strain contours for the solid domain for both problems. In all cases, solutions are very similar.

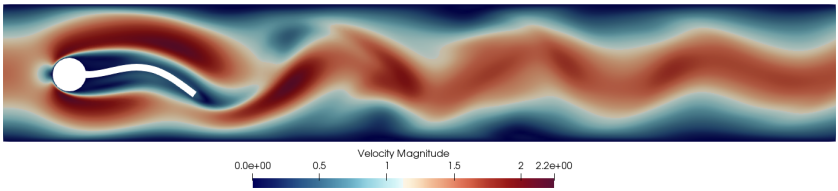

Figure 13.20: FOM - Velocity magnitude

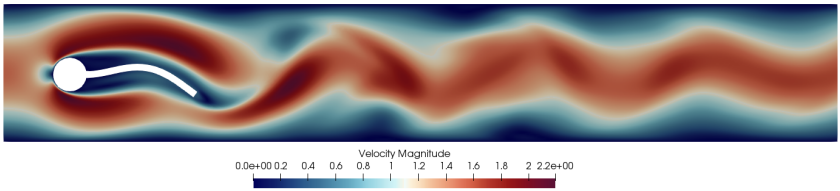

Figure 13.21: ROM - Velocity magnitude

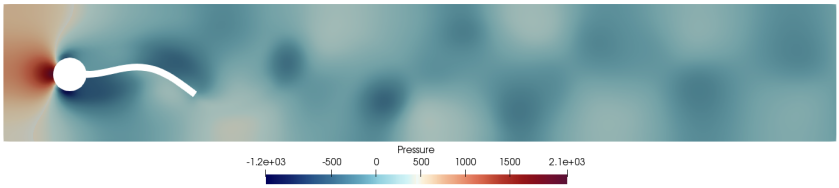

Figure 13.22: FOM - Pressure

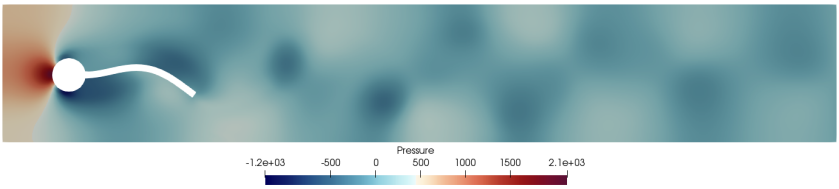

Figure 13.23: ROM - Pressure

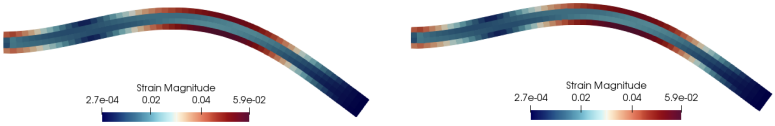

(a) FOM

(b) ROM

Figure 13.23: Strain magnitude for the solid bar

Out of the many results that can be shown, it is considered valuable to see the dependency of the ROM result on the energy percentage used. Results are shown for three particular cases, labeled ROM_A, ROM_B and ROM_C, which correspond to $\eta = 99.9999\%$ the first two and $\eta = 99.999999\%$ the last one. The bases for all three cases were obtained sampling every time-step the FOM solution to collect the snapshots. While cases ROM_A and ROM_B share the same basis and same energy percentage, the difference between them is the stabilization constant for the incompressibility term of the Navier-Stokes equation (see Eq. (5.9)). In this example we explore the effect of a slight variation in constant c_3. For case ROM_A we have used $c_3 = 1.5$, while for case ROM_B we have taken $c_3 = 2.0$.

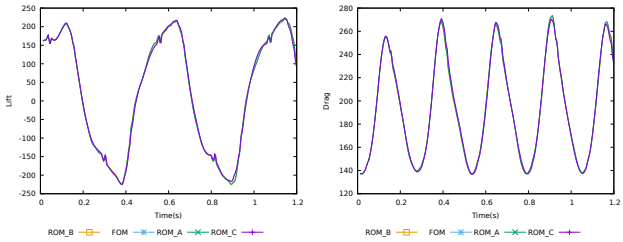

(a) Lift (b) Drag

Figure 13.24: Lift and drag around the flag

Figure 13.24 shows the drag and lift around the geometry of the flag caused by the fluid. Unlike the example shown in section 13.4, this test case is much more complex and requires much more computational time as well as a richer basis to produce meaningful results. Given that the results are very similar it is instructive to see a zoom for the lift, shown in Figure 13.25, where it is evident that a slight variation of the stabilization coefficient for the incompressibility produces a slightly degraded responses and in particular ROM_A slightly spurious by the evidence of oscillations. The loss of accuracy of ROM_A can be explained from figures 13.26a and 13.26b where a lower stabilization coefficient fails to reproduce as accurately as the other two cases correctly the high frequency portion of the spectrum.

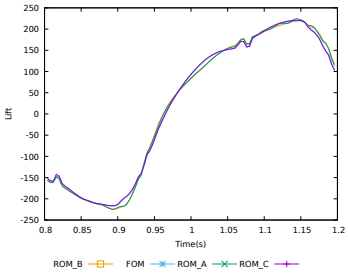

Figure 13.25: Zoom for lift

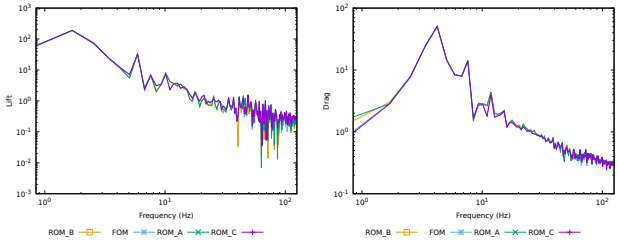

(a) Lift FFT (b) Drag FFT

Figure 13.26: FFT of the lift and drag around the flag

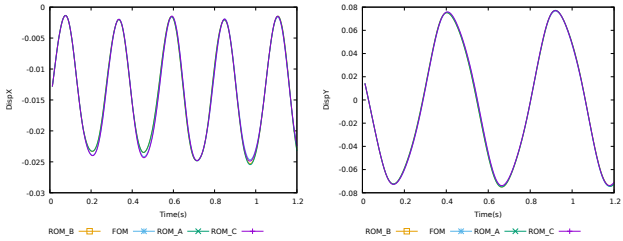

(a) Displacement in x axis (b) Displacement in y axis

Figure 13.27: Displacement at the tip of the flag

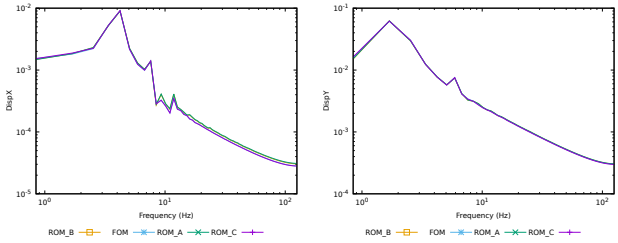

(a) Displacement FFT in x axis (b) Displacement FFT in y axis

Figure 13.28: FFT of the displacement at the tip of the flag

The case seems to be slightly different for the solid, where in figures 13.27 and 13.28 the displacement and its Fourier's transform

at the tip of the flag are shown and seen to reproduce accurately the FOM. Instead the effect of a variation in the stabilization constant for the incompressibility of the fluid is seen in the acceleration and its Fourier transform, shown in Figures 13.29 and 13.30 at the tip of the flag. It appears as though the stabilization constant for the incompressibility affects directly the temporal stability of the solid domain when projected into the ROM space, by restricting further the compressibility constraint we guarantee a more accurate behavior of the reduced problem. As discussed before, taking a lower stabilization constant fails to reproduce dramatically the higher frequency portion of the spectrum, see figure 13.30.

Table 13.10 shows the total times and speedups for all cases shown. It has to be remarked that we have not used any hyper-reduction strategy, and therefore these speedups could be improved. Note that the number of DOF in the fluid for the ROM is just 0.24% of that of the FOM for the richest ROM (163 DOF for the ROM vs. 67,926 DOF for the FOM). An ideal implementation would yield a reduction in the computational time solely determined by the number of DOF.

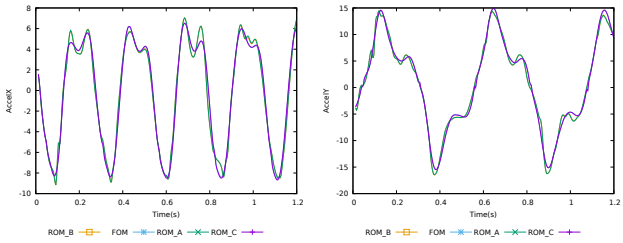

(a) Acceleration in x axis (b) Acceleration in y axis

Figure 13.29: Acceleration at the tip of the flag

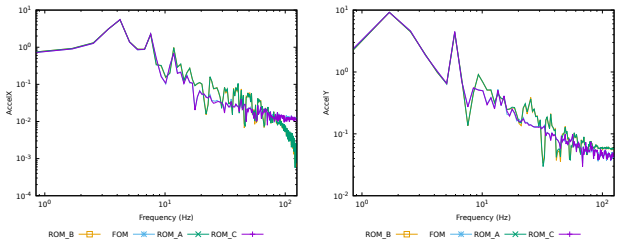

(a) Acceleration FFT in x axis (b) Acceleration FFT in y axis

Figure 13.30: FFT of the acceleration at the tip of the flag

		FOM	ROM_A	ROM_B	ROM_C
Fluid	Time(min)	88.53	16.21	19.33	18.94
	Speedup		81.69%	78.16%	78.6%
Solid	Time(min)	0.79	0.54	0.63	0.684
	Speedup		31.65%	20.25%	13.42%
Total	Time(min)	89.32	16.75	19.96	19.624
	Speedup		81.24%	77.65%	78.3%

Table 13.10: Time and speedup for fluid and solid domains

Finally it is instructive to see the behaviour of the FSI-ROM system when not enough basis energy is included into our reduced problem, the next results show a comparison for 99.99% (ROM_A), 99.9999% (ROM_B) and 99.999999% (ROM_C).

Figures 13.31a and 13.32b show the evolution of the displacement and acceleration for a point at the tip of beam and while it can be seen that for ROM_B and ROM_C the solution matches accurately with the results seen in [83], using less energy, ROM_A, results in a completely different response. Producing over-diffusive displacement, figure 13.31a, and amplified modes in the acceleration, figure 13.32a. From the Fourier transform of these quantities it can be seen that failing to introduce this portion of the spectrum results in an inaccurate

approximation of the lower frequencies and spurious high frequencies, figures 13.31b and 13.32b.

A similar result is seen for the fluid where the pressure is shown in figure 13.33 where the phase and amplitude is completely lost, figure 13.33a. Regarding the spectrum, figure 13.33b, shows a completely inaccurate reproduction of the lower energy modes and a diffusive behaviour towards the higher frequencies side of the spectrum.

Overall it is clear that it is critical to include sufficient energy from both domains otherwise a completely inaccurate solution from the system is obtained.

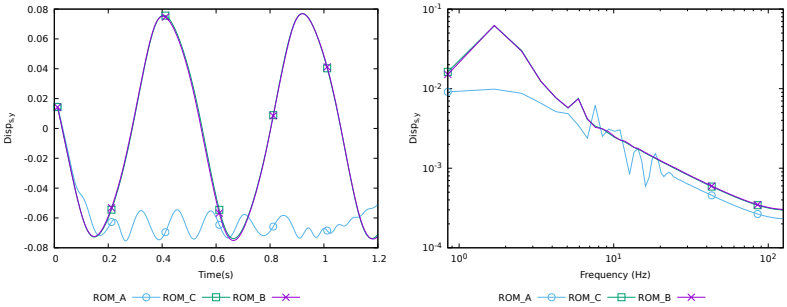

(a) Displacement in y axis

(b) Displacement FFT in y axis

Figure 13.31: Displacement in y and FFT at the tip of the flag

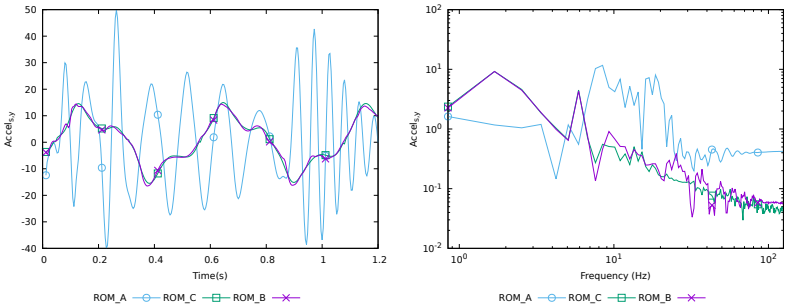

(a) Acceleration in y axis

(b) Acceleration FFT in y axis

Figure 13.32: Acceleration in y and FFT at the tip of the flag

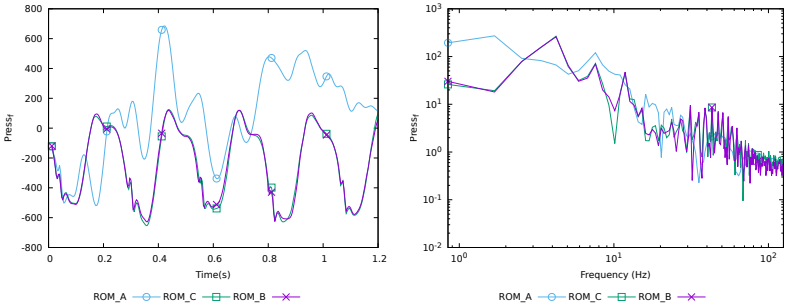

(a) Pressure in y axis

(b) Pressure FFT in y axis

Figure 13.33: Pressure in y and FFT at the tip of the flag

13.4 SEMI-STATIONARY BENDING OF A FSI FLAG

The semi-stationary problem, taken from [5], consists of a supported flag perpendicular to the fluid flow. Once the flow starts from the left wall it will bend the flag. For the particular conditions of the test, a force balance between the tractions imposed by the fluid and the stress on the flag will be achieved where the flag will remain bent without oscillation. The inflow velocity on the left wall is taken as $v_x = 1.0$ in the x direction and $v_x = 0.0$ in the y direction. Table 13.11 shows the boundary conditions, table 13.12 shows important mesh parameters and finally table 13.13 the test conditions.

Fluid	Solid
$x = 0$: $u_x = 1$, $u_y = 0$	$y = 0$: $d_x = d_y = 0$
$y = 0, H$: Free slip	Other boundaries: fluid tractions
$x = L$: Free	
Other boundaries: solid velocities	

Table 13.11: Boundary conditions

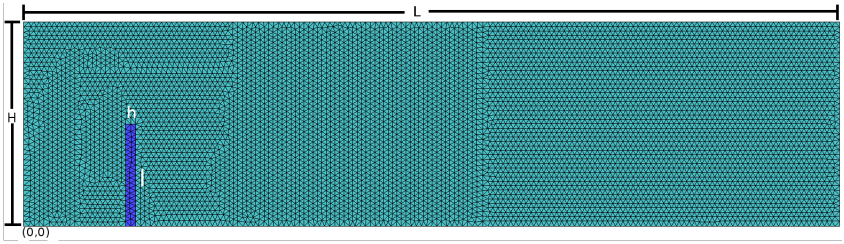

Figure 13.34: Geometry and mesh used for semi-stationary FSI-ROM case

	Fluid	Solid
Element type	Quadratic triangle	Quadratic triangle
Nodes per element	6	6
# of elements	14,308	78
# of nodes	29,057	201

Table 13.12: Mesh parameters

	Fluid		Solid
ρ_{fl}	2.0	ρ_{sl}	10.0
ν_{fl}	0.2	ν_{sl}	0.142857
		Young	55,428.0
model	Newtonian		Neo-Hookean

Table 13.13: Physical parameters

We first show the behavior of the FOM results for each Field to Field (F2F) coupling compared to each other. As it can be seen from figures 13.35 and 13.36 both irreducible and the two-field solutions are very similar to each other, reaching a stationary after 6 seconds, and while some modes can be seen around this region, they quickly dissipate. On the other hand the three-field does not reach a stationary in the interval shown, as we have seen, this formulation tends to be less diffusive than its counterparts. Given enough time all formulations converge to the same stationary. Regarding the pressure for the fluid it can be seen that all formulations have a very similar response. The legend for results is explained in table 13.14

Name	Fluid Formulation	Solid Formulation
1F	Two-field	Irreducible
2F	Two-field	Two-field
3F	Three-field	Three-field
3F/1F	Three-field	Irreducible
2F/3F	Two-field	Three-field

Table 13.14: Case parameters

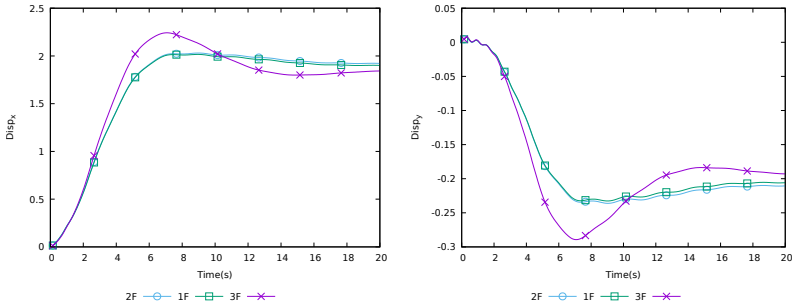

(a) Displacement in x (b) Displacement in y

Figure 13.35: Displacement at the tip of the beam FOM

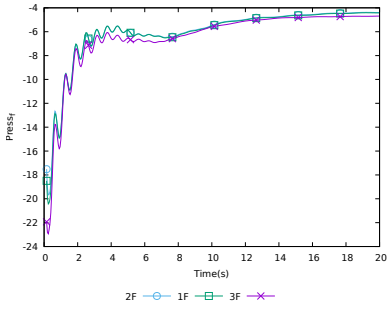

Figure 13.36: Pressure around the tip of the beam FOM

For the ROM solution it is not really helpful to visualize the results in the way shown for the FOM as there are too many results. For this

reason convergence tests where done for different amounts of energy for all three formulations and the Root-Mean-Square Deviation (RMSD) calculated for all samples. Our objective is to test the F2F coupling and its effect on the ROM results, but we cannot ignore the possibility of having mixed couplings and their behavior in the ROM space. In this way we chose to test as well what happens when fluid and solid where solved by mixed fields, namely 3F/1F and 2F/3F. Results are shown in the following plots. Note that while a test can consist of a fixed amount of energy for all three formulations this does not mean that all use the same amount of basis vectors. Figure 13.37 helps understand the correlation between energy and basis vectors. As a general trend this relation is not linear and the reduced problem becomes increasingly expensive as more energy is used, this is specially true for the three-field problem particularly in the solid, shown on figure 13.37a. Also note that for the fluid we are testing only two types of formulations, two-field and three-field, but three types of couplings, reason that explains the increased basis vector usage towards 99.9999% on figure 13.37b.

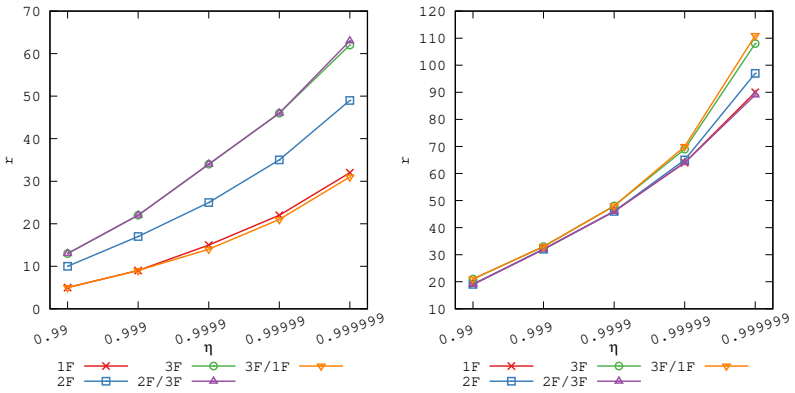

(a) Solid (b) Fluid

Figure 13.37: # basis vectors per energy %

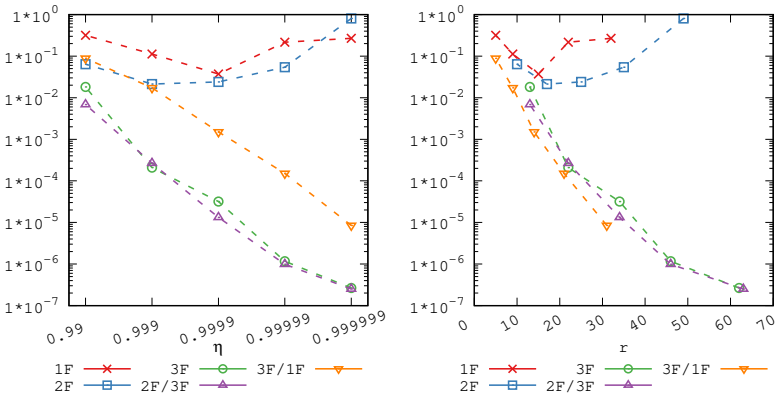

(a) Energy %

(b) # Basis vectors

Figure 13.38: Convergence for ROM Displacement for solid at tip per basis vectors and energy

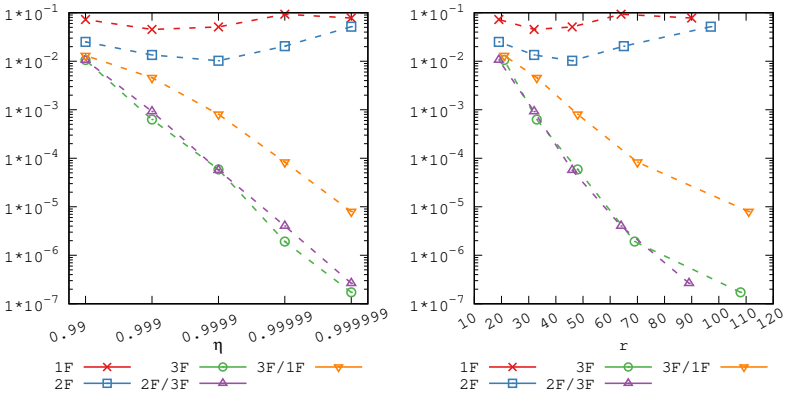

(a) Energy %

(b) # Basis vectors

Figure 13.39: Convergence for ROM Velocity for the fluid per basis vectors and energy

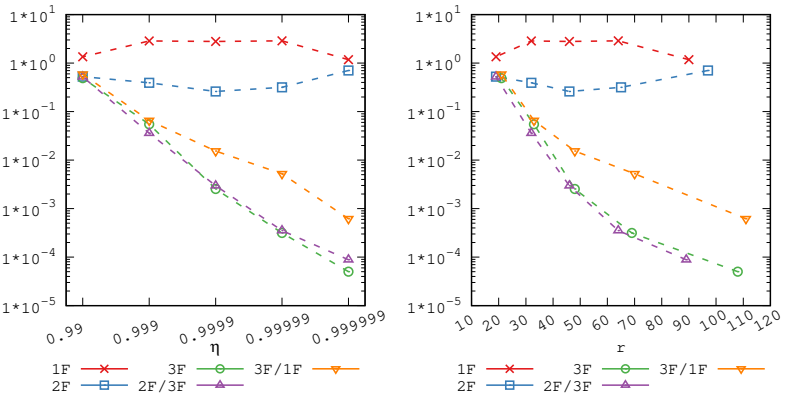

(a) Energy %

(b) # Basis vectors

Figure 13.40: Convergence for ROM Pressure for the fluid per basis vectors and energy

Figures 13.38 to 13.40 show the evolution of the error in terms of energy and basis vectors. Note that in general the 3F and the 2F/3F formulation present the best convergence rate and additionally the most precise results. For the 1F and 2F, as the amount of basis vectors increase the error first decreases and then, after a certain value, starts to slowly increase again, the 1F coupling seems to be most vulnerable to this phenomenon, that we attribute to over-fitting. The two-field coupling, once again, falls in between with the possibility of utilization of more basis vectors before the solution starts to degenerate. Notice how in the interval shown over-fitting is not evident for any of the couplings that make use of a three-field formulation. The standard coupling seems to be very vulnerable to this issue with a very low threshold before solution degeneration, this might hint at the possibility that ROM with the standard FSI coupling is indeed more difficult than its other two counterparts. It seems that while the 3F seems to be most precise coupling, any coupling that makes use of a three-field formulation will have improved convergence properties. Also notice that a F2F coupling is always more precise that the standard coupling. For example in Figures 13.39 and 13.40 the 2F coupling

performs significantly better that the standard (1F) FSI for both velocity and pressure for the fluid.

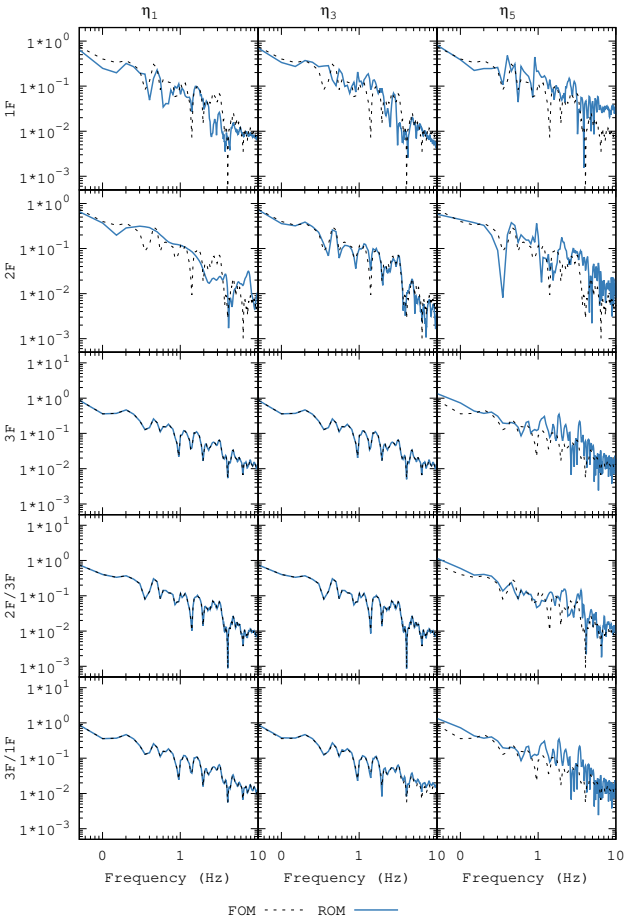

Figure 13.41: Fourier transform for the acceleration at the tip of the beam for the solid

Lastly figure 13.41 shows the fourier transform for the acceleration at the tip of the bar for the solid for all couplings and different amount of energy, being η_1 higher and η_5 lower. It seems that any of the three-field couplings are very resilient to change of energy in basis,

approximating very well the solution in all cases. For the two-field and the standard couplings the best approximation is seen from η_3 where a great part of the spectrum is fairly well approximated.

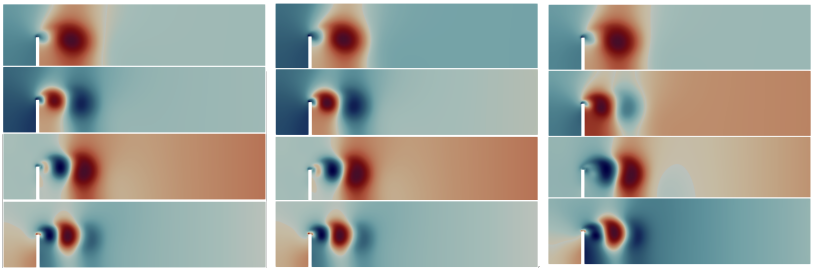

(a) 1F (b) 2F (c) 3F

Figure 13.42: Basis contours for the pressure for 1F, 2F and 3F

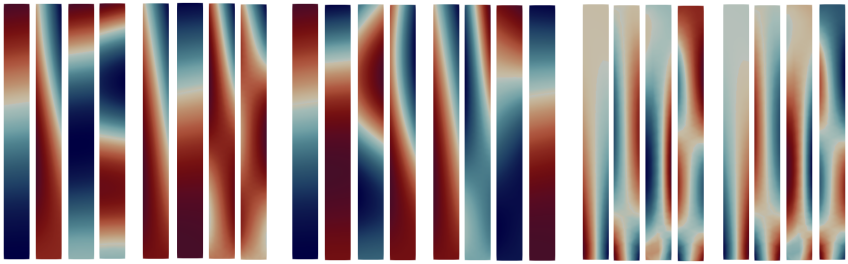

(a) Disp x 1F (b) Disp y 1F (c) Disp x 2F (d) Disp y 2F (e) Disp x 3F (f) Disp y 3F

Figure 13.43: Basis contours for the displacement for 1F, 2F and 3F

As was done for the example in section 13.2 it is illustrative to analyze the contour plots for the basis modes for each of the formulations. As it obvious for the fluid for the 1F and 2F coupling remains unchanged, shown in figures 13.42a and 13.42b, while the 3F basis, shown in figure 13.42c, hints at higher mode magnitude but overall very similar behavior.

On the other hand the solid tells a completely different story. Once again the calculated basis and modes are very different from each

other. Not much can be said for the 1F and 2F couplings for the solid, shown in section 13.4, other than there is very little similitude and no clear modes. The three-field coupling 3F, shown in figure 13.43, once again shows clear modes that hints to a richer basis that produces a more precise reduced problem.

13.5 FLOW INJECTION INTO A CHANNEL WITH AN ELASTIC SOLID

This is a fully dynamic problem that consists of a flow injection into a bifurcating 2D channel with an elastic solid at the bifurcation that acts as a sort of valve. Once the fluid starts interacting with the solid, the latter starts to oscillate, expand and contract, thus changing the direction of the flow into one of the two outlets available. The geometry of the test, mesh and boundary conditions are shown in figure 13.44; notice how in the outlets elongated elements were assigned to prevent back-flow and a smooth exit for the fluid. A horizontal velocity $v_x = 0.75$ is prescribed on the middle one third of the left wall, whereas on the rest of this wall the velocity is fixed to zero.
The test conditions are shown in table 13.15, where $\nu_{fl} = \mu_{fl}/\rho_{fl}$ the kinematic viscosity of the fluid.

	Fluid		Solid
ρ_{fl}	500.0	ρ_{sl}	2 500.0
ν_{fl}	0.1	ν_{sl}	0.3
		Young	2,000.0
model	Newtonian		Neo-Hookean

Table 13.15: Physical parameters (SI units)

Triangular quadratic elements have been used for both the fluid and the solid, with 6 107 elements and 12 848 nodes for the former and 3 072 elements and 6 323 nodes for the latter. The time step size has been taken $\delta t = 0.2$.

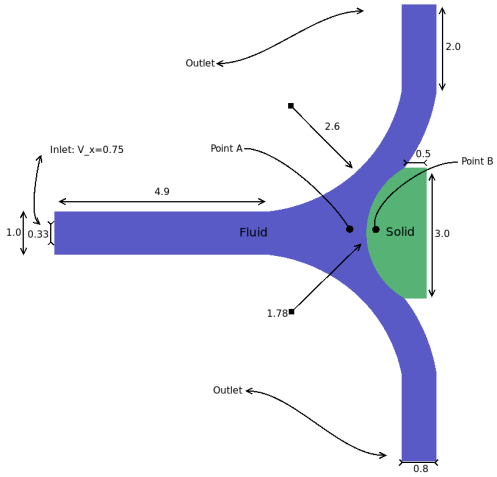

(a) Geometry for test

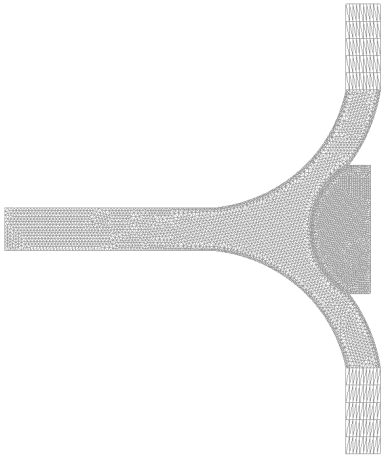

(b) Mesh used in test

Figure 13.44: Geometry and mesh used for fully dynamic FSI-ROM case

We first show the behavior of the FOM results for each formulation. As it is now expected, the both irreducible and the two-field solutions are very similar to each other, while the three-field formulation follows a

similar trend but having a higher frequency response both for pressure and velocity, see figure 13.45, figure 13.46, figure 13.47.

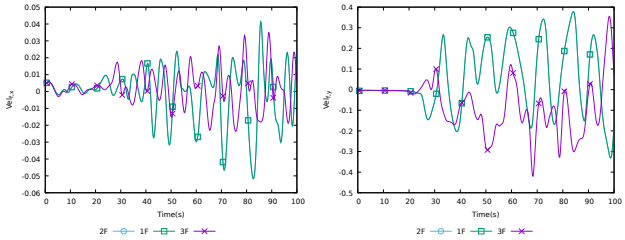

(a) Velocity in x (b) Velocity in y

Figure 13.45: Velocity for the fluid (point A), FOM

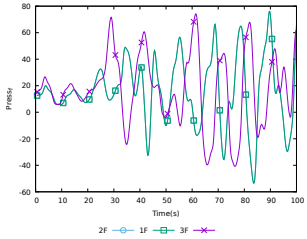

Figure 13.46: Pressure for the fluid (point A), FOM

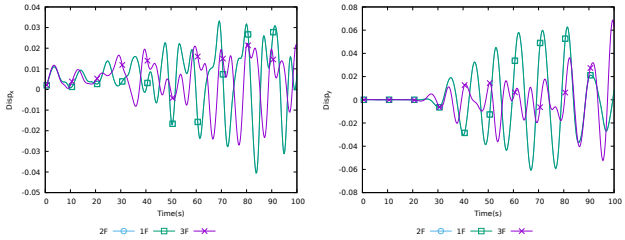

(a) Displacement in x (b) Displacement in y

Figure 13.47: Displacement for the fluid (point B), FOM

Referring now to the ROM, convergence tests were done for different amounts of energy for all three formulations and the RMSD calculated for all samples. Results are shown in the following plots. figure 13.48 shows the correlation between energy and number of basis vectors for all three formulations. For the solid, the curves shown in figure 13.48a are significantly different for the three formulations. The plot for the fluid, shown on figure 13.48b, indicates that all three formulations behave similarly in terms of energy use and the number of associated basis vectors, linearly except for the highest amount of energy. Remember that for the fluid the 1F and 2F couplings use the same velocity–pressure formulation.

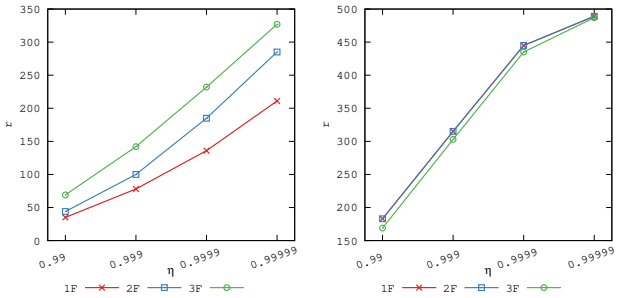

(a) Solid (b) Fluid

Figure 13.48: # basis vectors per energy %

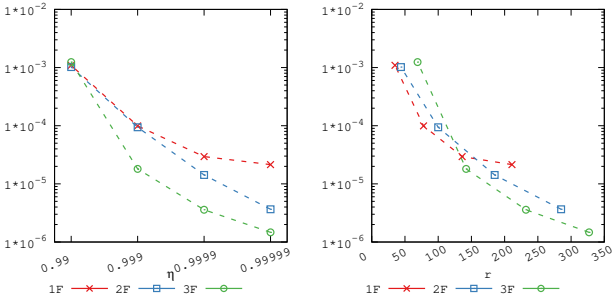

(a) Energy % (b) # Basis vectors

Figure 13.49: ROM convergence: Solid displacement (point B); basis vectors and energy

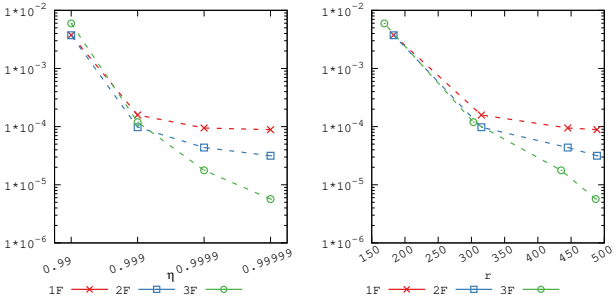

(a) Energy % (b) # Basis vectors

Figure 13.50: ROM convergence: fluid velocity (point A); basis vectors and energy

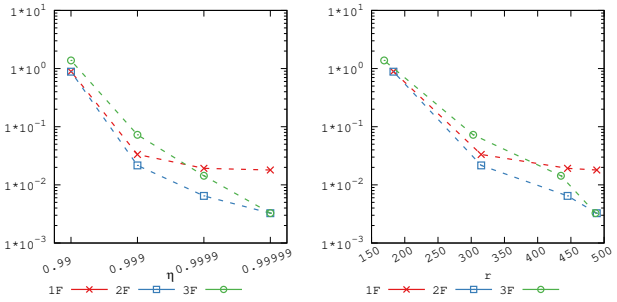

(a) Energy %

(b) # Basis vectors

Figure 13.51: ROM convergence: Fluid pressure (point A); basis vectors and energy

figure 13.49, figure 13.50, and figure 13.51 show the evolution of the error in terms of energy and number of basis vectors. The best approximation for the displacement in the solid is obtained with the three-field formulation. The velocity in the fluid appears to be better approximated by the three-field formulation while the pressure is better approximated by the two-field approach for small values of r, although the slope of the three-field formulation seems to be higher. In general the F2F coupling is more precise than the standard coupling. Good results have been obtained for the approximation of this problem by means of all formulations, but the most precise is the three-field one. It is illustrative to see how the response of the ROM correlates with the FOM. In this order of ideas, graphs of the dynamic response are shown for both FOM and ROM comparing different amounts of energy for the three-field scenario. Table 13.16 shows the explanation for the legend in the graphs.

Name	Formulation	Space	Energy(%)
fom	Three-field	FOM	
rom_99	Three-field	ROM	99.0
rom_9e3	Three-field	ROM	99.9
rom_9e4	Three-field	ROM	99.99
rom_9e5	Three-field	ROM	99.999

Table 13.16: Case parameters

figure 13.52 and figure 13.53 show the displacement of the solid at point B and velocity for the fluid at point A, respectively. Notice that the dynamic response is quite complex, but nevertheless, it is correctly captured by all ROM cases. There is a slight overshoot for the amplitude response for rom_99, but phase is preserved.

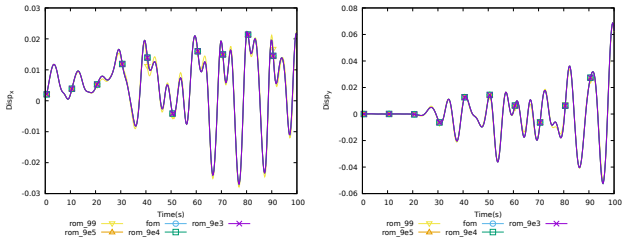

(a) Displacement x (b) Displacement y

Figure 13.52: FOM-ROM for solid displacement (point B) for the three-field formulation

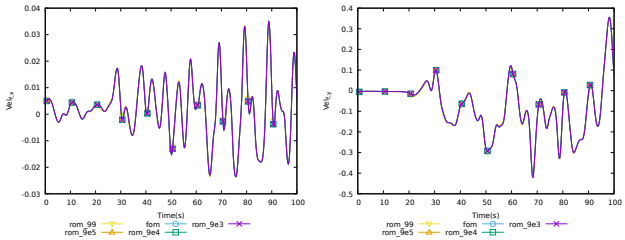

(a) Velocity x (b) Velocity y

Figure 13.53: FOM-ROM for fluid velocity (point A) for the three-field formulation

Lastly, to exemplify the complexity of the flow, contour plots for some variables are shown next for different intervals of the dynamic evolution. Notice how the flow starts, develops, starts affecting the solid and finally a feedback loop is started from the coupling. All contour plots are taken from the rom_9e5 results.

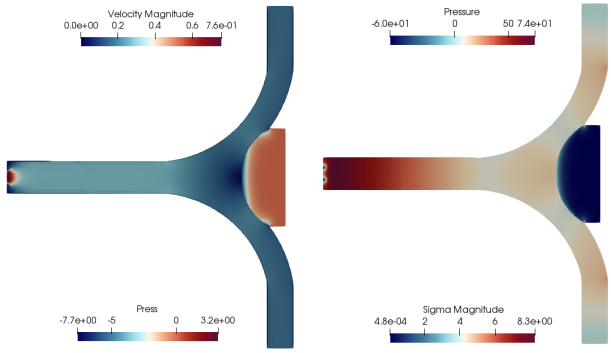

(a) Fluid velocity and solid pressure

(b) Fluid pressure and solid deviatoric stress

Figure 13.54: Fluid and solid solution contours at t = 0 s

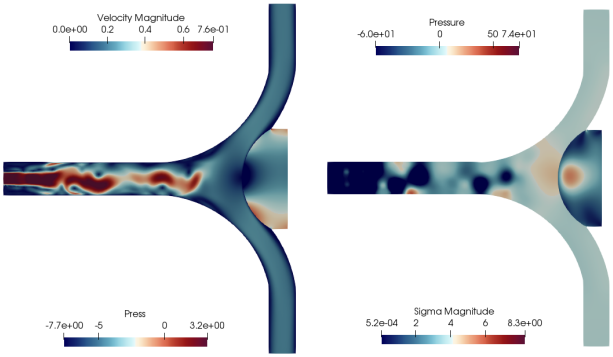

(a) Fluid velocity and solid pressure

(b) Fluid pressure and solid deviatoric stress

Figure 13.55: Fluid and Solid solution contours at t = 20 s

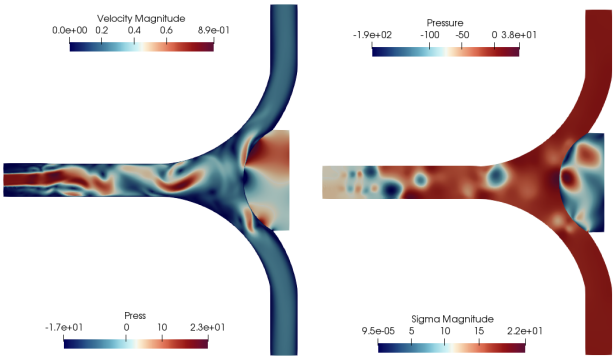

(a) Fluid velocity and solid pressure (b) Fluid pressure and solid deviatoric stress

Figure 13.56: Fluid and solid solution contours for t = 32 s

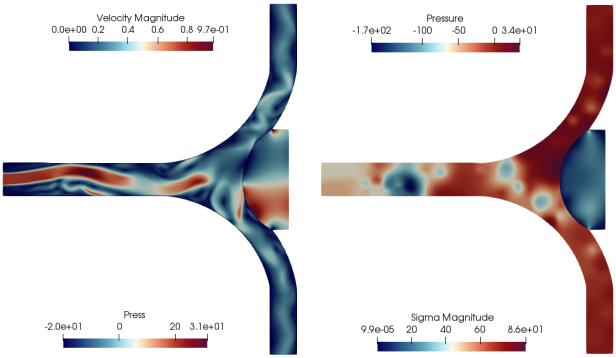

(a) Fluid velocity and solid pressure (b) Fluid pressure and solid deviatoric stress

Figure 13.57: Fluid and solid solution contours for t = 52 s

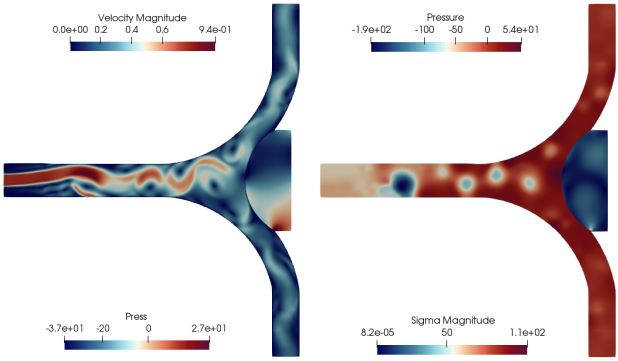

(a) Fluid velocity and solid pressure

(b) Fluid pressure and solid deviatoric stress

Figure 13.58: Fluid and solid solution contours for t = 72 s

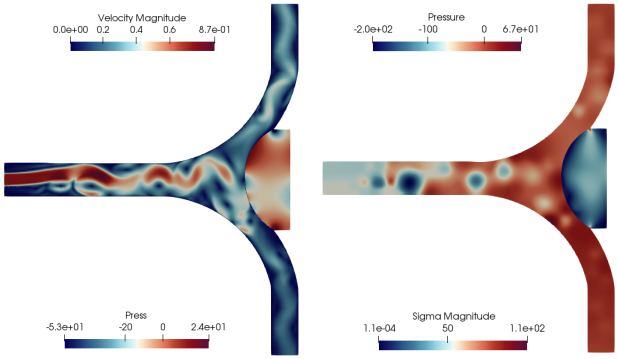

(a) Fluid velocity and solid pressure

(b) Fluid pressure and solid deviatoric stress

Figure 13.59: Fluid and solid solution contours for t = 90 s

Overall this test shows a complex scenario with a challenging dynamic response that was correctly captured by all formulations, the most precise being the F2F couplings.

13.6 3D FLOW AROUND A PLATE

The following example is a 3D version of the one shown in section 13.4. The test conditions are shown in table 13.17.

	Fluid		Solid
ρ_{fl}	100.0	ρ_{sl}	1 000.0
ν_{fl}	1.0	ν_{sl}	0.48
		Young	300×10^3
model	Newtonian		NeoHookean

Table 13.17: Physical parameters

The geometry is shown in figure 13.60. Table 13.18 shows important mesh parameters, geometrical parameters are shown in table 13.19 and table 13.20 shows the boundary conditions.

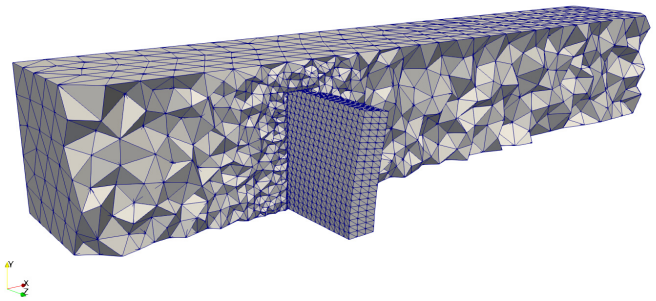

Figure 13.60: Case geometry

	Fluid	Solid
Element type	Linear Tetrahedra	Linear Tetrahedra
Nodes per element	4	4
# of elements	87 941	10 833
# of nodes	16 785	2 491

Table 13.18: Mesh parameters

Height (H):	0.5
Width :	1.0
Length:	3.0
Inlet mean velocity ($\overline{U}$) :	1.0

Table 13.19: Channel dimensions and flow parameters

	Fluid	Solid
Flow inlet:	$1.5\overline{U} \cdot \frac{y \cdot (0.5-y) \cdot z \cdot (1.0-z)}{\left(\frac{H}{2}\right)^2}$	
Flow outlet:	Free	
Channel walls:	No slip	
Plate sides:	Solid velocities	Fluid tractions
Plate bottom:		Fixed

Table 13.20: Boundary conditions

The next series of graphs in figure 13.61, figure 13.62 and figure 13.63 show a comparison between the solution obtained by means of the three-field formulation (labeled 'sup') and using the displacement based one (labeled 'irr').

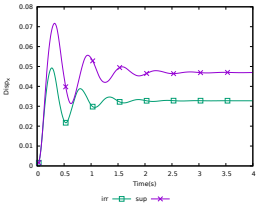

(a) Displacement in x

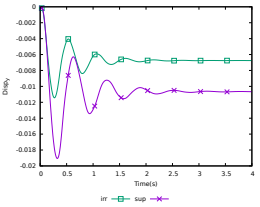

(b) Displacement in y

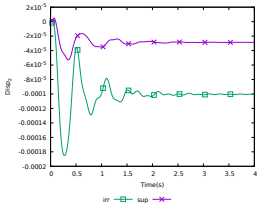

(c) Displacement in z

Figure 13.61: Displacement at the tip of the plate

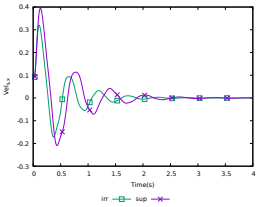

(a) Velocity in x

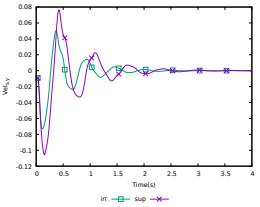

(b) Velocity in y

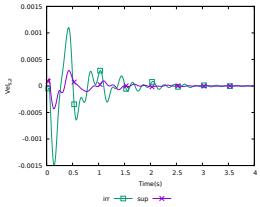

(c) Velocity in z

Figure 13.62: Velocity at the tip of the plate

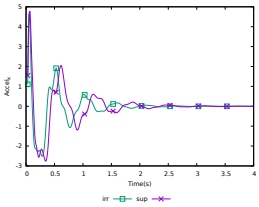

(a) Acceleration in x

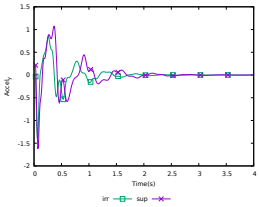

(b) Acceleration in y

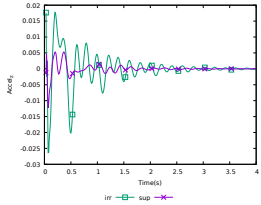

(c) Acceleration in z

Figure 13.63: Acceleration at the tip of the plate

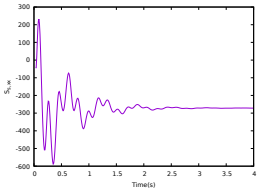

(a) Stress in xx

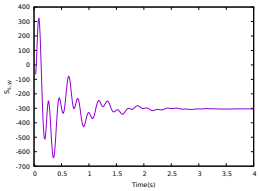

(b) Stress in yy

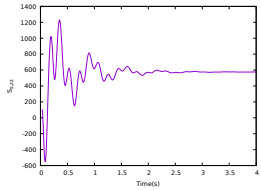

(c) Stress in zz

Figure 13.64: Normal stresses at the tip of the plate

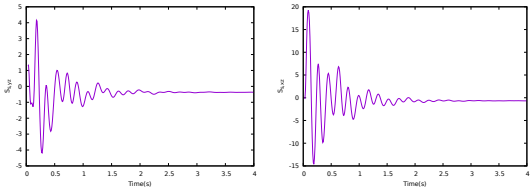

(a) Stress in yz (b) Stress in xz

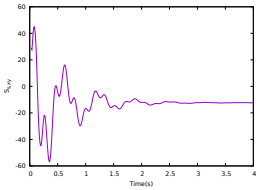

(c) Stress in xy

Figure 13.65: Normal stresses for the tip of the plate

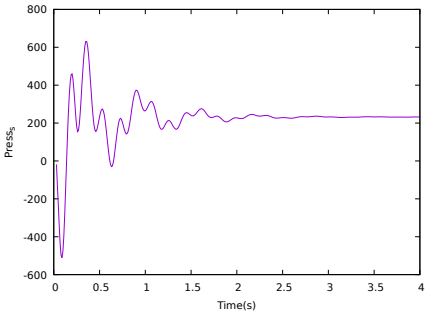

Figure 13.66: Pressure

Notice how the overall behavior of the standard displacement based formulation is over-diffusive and tends to over-dampen the motion of the plate, see figure 13.61. In turn, the velocities and accelerations of the plate in the three-field formulation have a higher amplitude, see

figure 13.62 and figure 13.63. The displacement based formulation reaches a stationary state earlier than the three-field formulation, and it also produces a result with lower frequency, which leads to important phase differences.

Even if we do not have any reference for comparison, it is important to note that the stress and pressure fields shown in figure 13.64, figure 13.65 and figure 13.66 are smooth and continuous and decay to reach a stationary state, as the displacement field.

Finally, and in order to visualize the solution to this problem, figure 13.67, figure 13.68 and figure 13.69 show contours of velocity norm (fluid)–displacement norm contours (solid), stress norm contours (fluid)–displacement magnitude contours (solid), and velocity vectors, respectively, of the solution obtained.

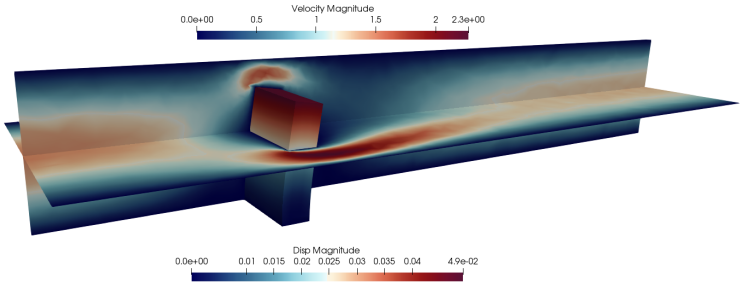

Figure 13.67: Fluid: Velocity contours; Solid: Displacement contours

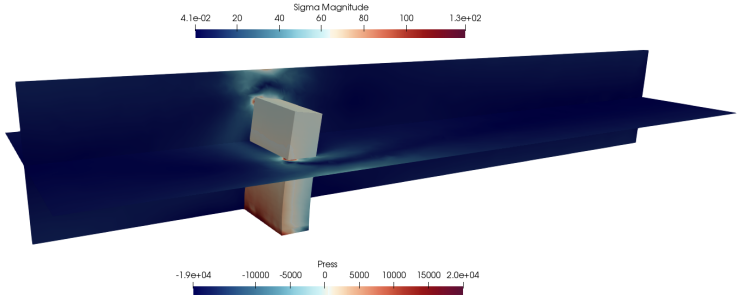

Figure 13.68: Fluid: Stress (sigma) contours; Solid: Pressure magnitude contours

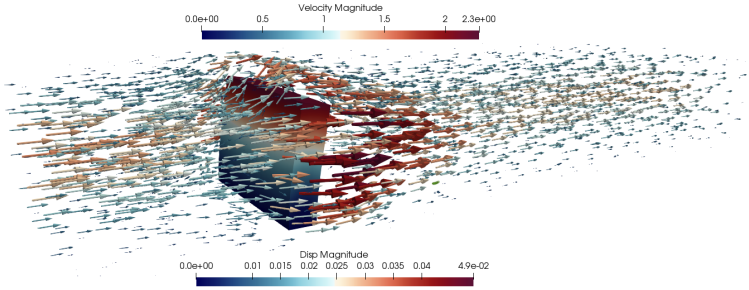

Figure 13.69: Fluid: Velocity vectors; Solid: Displacement contours

ROM

Once the test case has been benchmarked for all F2F-FSI couplings in the Finite Element (FE) space we decided to evaluate the performance of the three-field coupling, that we have seen is the most precise, in the reduced space. These results are shown as a qualitative example that good approximation can even be obtained for very coarse meshes with the three-field coupling. Results are shown as a comparison for the FOM and a series of ROM cases ran with varying amount of energy. The legend for the results can be found in table 13.21.

Name	Formulation	Space	Energy(%)
fom	Three-field	FOM	
rom_e99	Three-field	ROM	99.0
rom_e9e3	Three-field	ROM	99.9
rom_e9e4	Three-field	ROM	99.99
rom_e9e5	Three-field	ROM	99.999

Table 13.21: Case parameters

Accurate results have been obtained for all variable shown. It is seen that the solid tends to a stationary configuration; in spite of a slightly different transient for all formulations considered, this steady state is the same for all approaches.

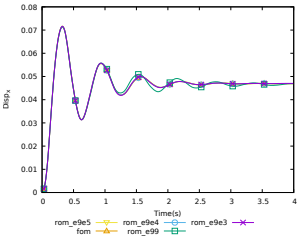

(a) Displacement in x

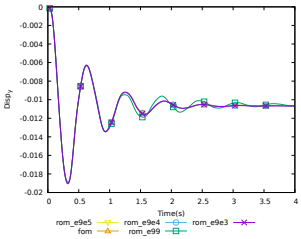

(b) Displacement in y

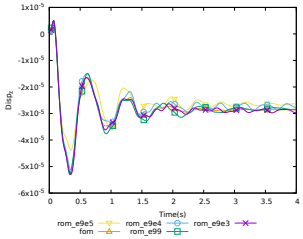

(c) Displacement in z

Figure 13.70: Displacement at the tip of the plate

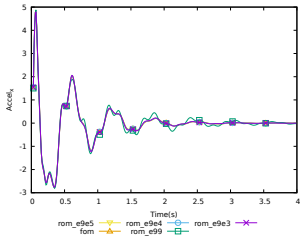

(a) Acceleration in x

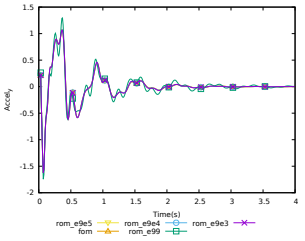

(b) Acceleration in y

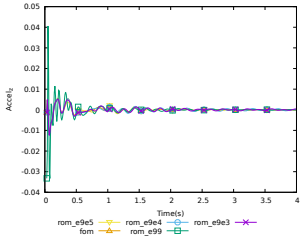

(c) Acceleration in z

Figure 13.71: Acceleration at the tip of the plate

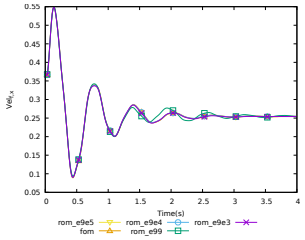

(a) Velocity in x

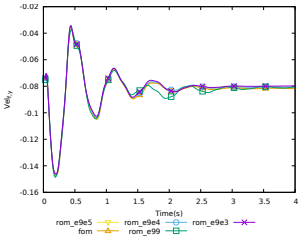

(b) Velocity in y

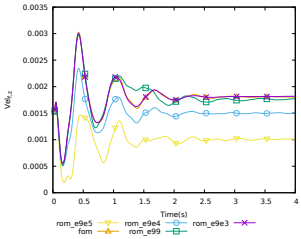

(c) Velocity in z

Figure 13.72: Velocity for the fluid at the tip of the plate

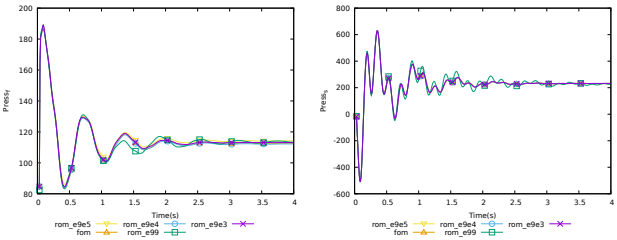

(a) Fluid

(b) Solid

Figure 13.73: Pressure for fluid and solid at the tip of the plate

Notice how overall every ROM test case approximates accurately the FOM solution, although some inaccuracy can be seen in the approximation of the z axis solutions. This is a phenomenon that we have seen, see section 13.7, specially in 3D cases where one of the axis has considerably smaller magnitude than the other two. Regardless of this fact solution for even smaller amounts of energy is accurate specially taking into account the coarse mesh used.

13.7 3D DRIVEN CAVITY

The following example is a 3D version of the one shown [86]. The test conditions are shown in table 13.22 in SI units.

	Fluid		Solid
ρ_{fl}	1.0	ρ_{sl}	5000.0
ν_{fl}	0.01	ν_{sl}	0.1
		Young	250
model	Newtonian		NeoHookean

Table 13.22: Physical parameters

The geometry is shown in figure 13.74. Table 13.23 shows important mesh parameters, the geometry is a cubic cavity of side with length one and table 13.24 shows the boundary conditions.

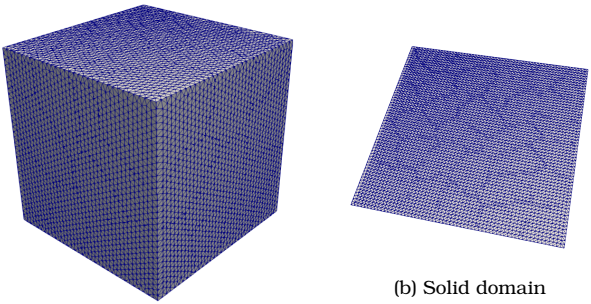

(a) Fluid domain

(b) Solid domain

Figure 13.74: Case geometry

	Fluid	Solid
Element type	Linear Tetrahedra	Linear Tetrahedra
Nodes per element	4	4
# of elements	369 048	64 800
# of nodes	66 321	14,884

Table 13.23: Mesh parameters

	Fluid	Solid
Upper surface:	Case dependent	
Cavity walls:	No slip	
Solid plate sides:		Fixed
Solid plate top:		Fluid tractions

Table 13.24: Boundary conditions

The next series of graphs show a comparison between the solution obtained for the standard FSI coupling for both FOM and ROM scenarios. Regarding the ROM though various cases with different amounts of energy where studied the most accurate one is the one shown (energy for both fluid and solid $\eta = 99\%$). The other cases were either over-diffusive or diverged. Two cases of interest are shown, the first one section 13.7.1 where the velocity boundary condition for the upper surface of the fluid domain follows the following time function: $v_x = 1 - cos(\frac{2\pi t}{5}); v_y = v_z = 0.0$. The second one, shown in section 13.7.2 where the upper surface of the fluid domain has a constant velocity condition: $v_x = 1.0, v_y = v_z = 0.0$. These two cases turned out to be completely different, showing different aspects of the challenges associated with FSI and ROM, more detail in the next sections. In both cases the time step is taken as $\delta t = 0.01$.

13.7.1 *Case 1*

This case is of interest because of the oscillatory nature of the velocity boundary condition of the upper surface of the cavity. The idea is to see what effect does this condition have on the solid and in turn the effects on the flow inside. It turns out that this test does not cause large deformations on the solid due to its inertia as the velocity oscillates from side to side. On the other hand this velocity oscillation does activate the vibration modes of the solid which can be seen in figure 13.80, the matching fluid contours are shown in figure 13.88. Regarding the FOM–ROM behavior figures 13.75 and 13.76 show the dynamic evolution of the plate's displacement and acceleration for a point located at the center of gravity. It can be seen that this test case is fully dynamic and the ROM can represent this behavior accurately. Dynamic response in the z direction is omitted as its magnitude was too small compared to the other two components. Noise was also more evident in the z direction. It is interesting to note that in general through what has been seen during the development of this dissertation a ROM will struggle mostly with high frequencies of low magnitude, as seen in figure 13.76a. The fluid's velocity and pressure, shown in figures 13.77 and 13.78 have been accurately approximated by the ROM.

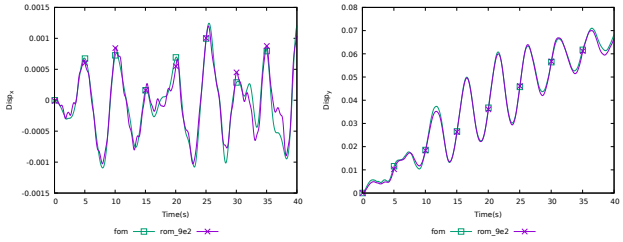

(a) Displacement in x (b) Displacement in y

Figure 13.75: Displacement at at plate center of mass

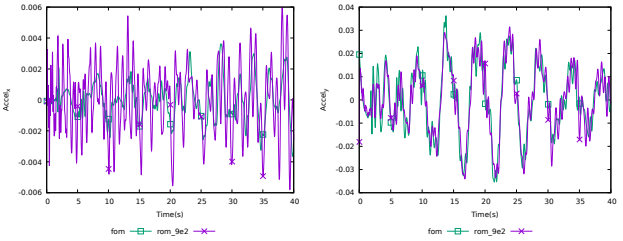

(a) Acceleration in x (b) Acceleration in y

Figure 13.76: Acceleration at plate center of mass

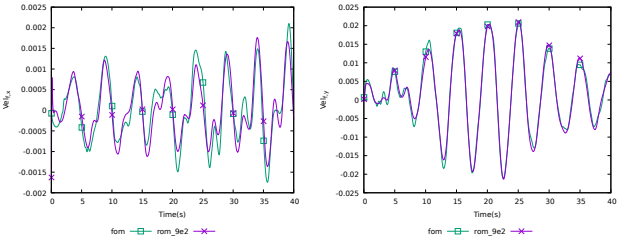

(a) Velocity in x (b) Velocity in y

Figure 13.77: Fluid velocity above plate center of mass

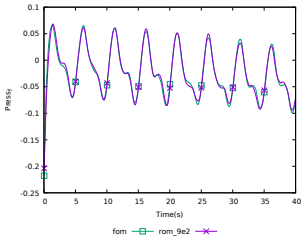

Figure 13.78: Fluid pressure above plate center of mass

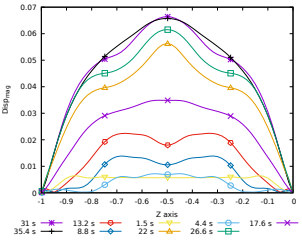

Figure 13.79: ||Disp|| evolution Z axis, X= 0.5, Y = -0.001

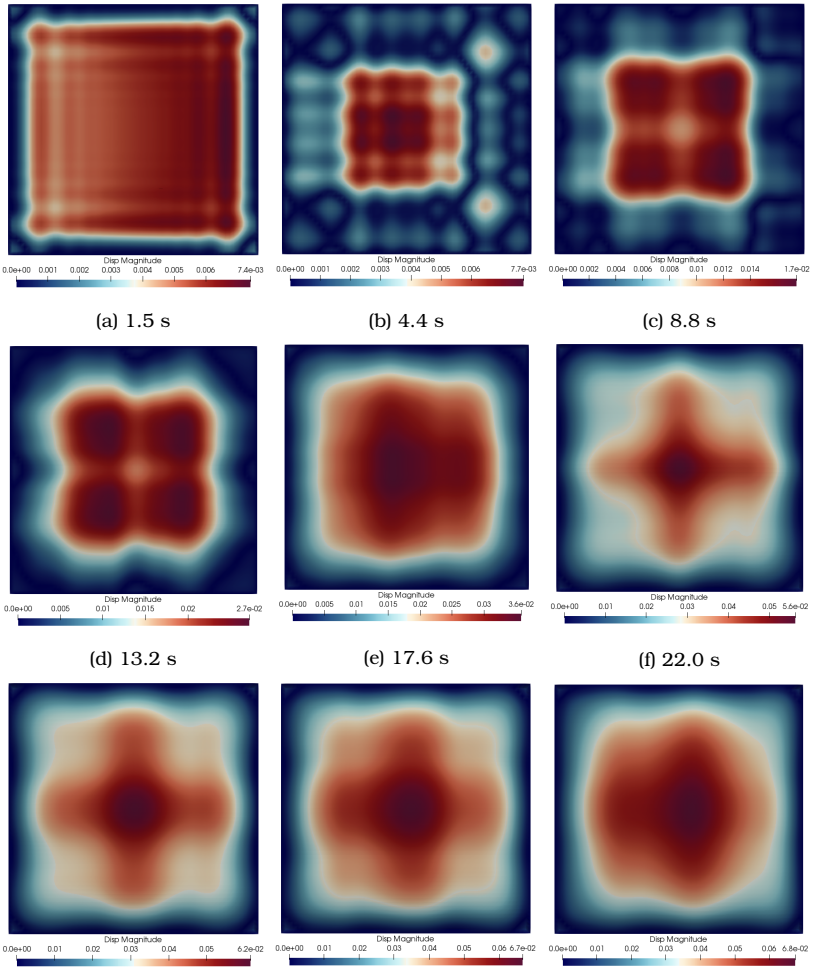

(a) 1.5 s (b) 4.4 s (c) 8.8 s

(d) 13.2 s (e) 17.6 s (f) 22.0 s

(g) 26.6 s (h) 31.0 s (i) 35.4 s

Figure 13.80: Plate displacement contours in time

Figure 13.80 shows the harmonic evolution of the plate displacement caused by the fluid flow. Plotting the evolution of the displacements along the Z axis for all time intervals will reveal that the solution is always continuous as shown on figure 13.79, showing that it is a physical response of the plate where we can see high frequencies

initially, see figures 13.80a and 13.80b, that will be damped leaving only lower frequency modes.

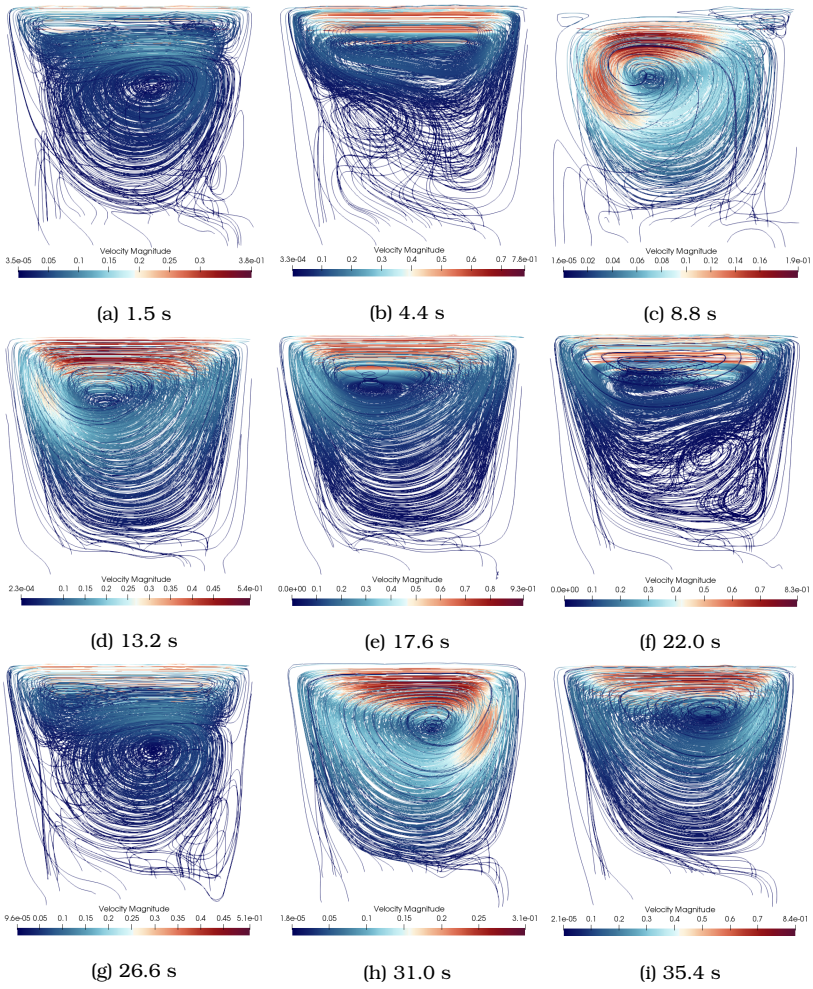

(a) 1.5 s (b) 4.4 s (c) 8.8 s

(d) 13.2 s (e) 17.6 s (f) 22.0 s

(g) 26.6 s (h) 31.0 s (i) 35.4 s

Figure 13.81: Fluid velocity streamlines in time

Figure 13.81 shows the corresponding flow to the displacement of the plate, note how the inner vortex oscillates from side to side as the velocity boundary condition changes. Finally figure 13.82 shows the

full geometry at 26.6 seconds and table 13.25 shows the considerable reduction in terms of degrees of freedom. Notice that in this case it makes sense that the solid requires more basis vectors than the fluid as its behavior is noticeably more complex in terms of frequency response as was previously discussed.

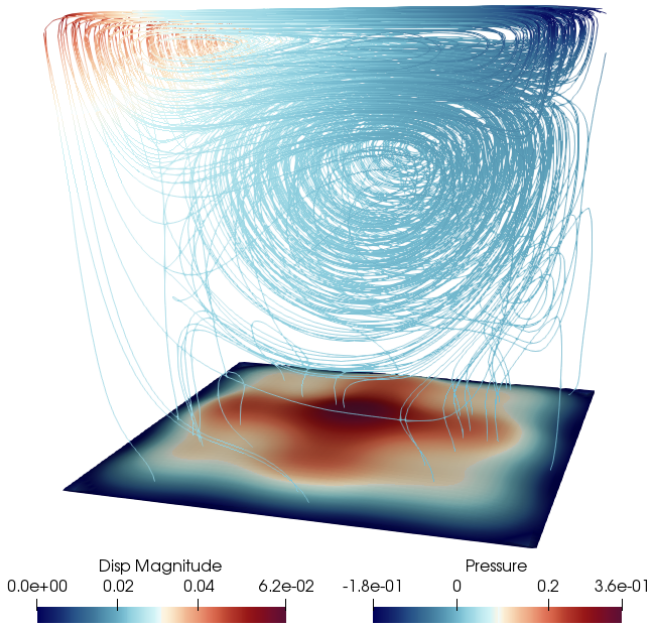

Figure 13.82: Velocity streamlines and plate displacement at $t = 26.6s$

	FOM	ROM	Reduction (%)
Fluid	198 963	28	99,986
Solid	14 884	61	99,59
Total			99,96

Table 13.25: DOF reduction

13.7.2 *Case 2*

This test case as a difference from the one shown in section 13.7.1 has a constant velocity condition on the upper surface of the fluid domain. This causes a constant displacement on the solid so larger magnitudes can be achieved. Note that given that the boundary condition is a prescribed pure shear on the fluid boundary this creates suction inside of the domain that sucks in the plate, therefore the deformation is towards the inside of the domain. In this case, as there is no oscillation of the boundary condition, the deformation of the solid plate at the bottom increases and tends to a stationary, not shown in the sampling interval, and follows the dynamic evolution shown in figures 13.83 and 13.84 for displacements and acceleration respectively. Note that ROM results are also shown in these figures.

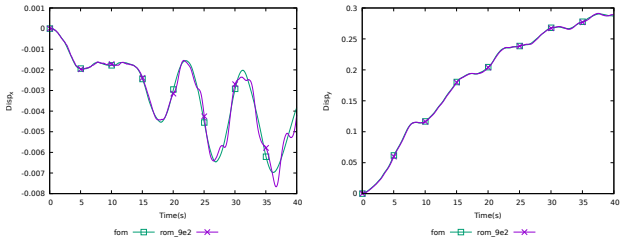

(a) Displacement in x (b) Displacement in y

Figure 13.83: Displacement at at plate center of mass

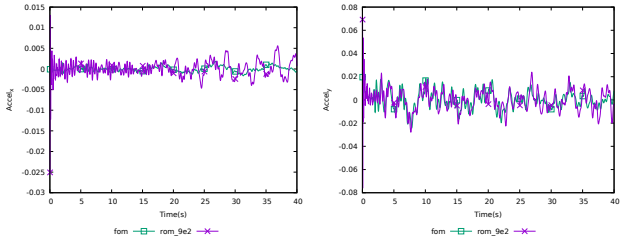

(a) Acceleration in x (b) Acceleration in y

Figure 13.84: Acceleration at plate center of mass

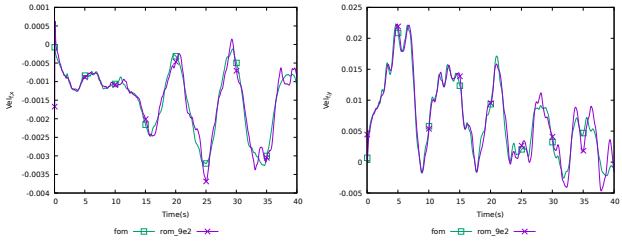

(a) Velocity in x (b) Velocity in y

Figure 13.85: Fluid velocity above plate center of mass

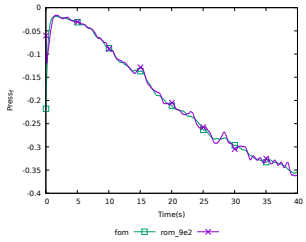

Figure 13.86: Fluid pressure above plate center of mass

As in the previous case contours are shown for displacement in figure 13.87 and velocity streamlines in figure 13.88. Note that the deformation is towards the inside of the domain as previously discussed, also note that as there is a constant velocity profile that

velocity streamlines suffer less change and the main central vortex remains more or less constant though the flow does compress due to the plate upward displacement.

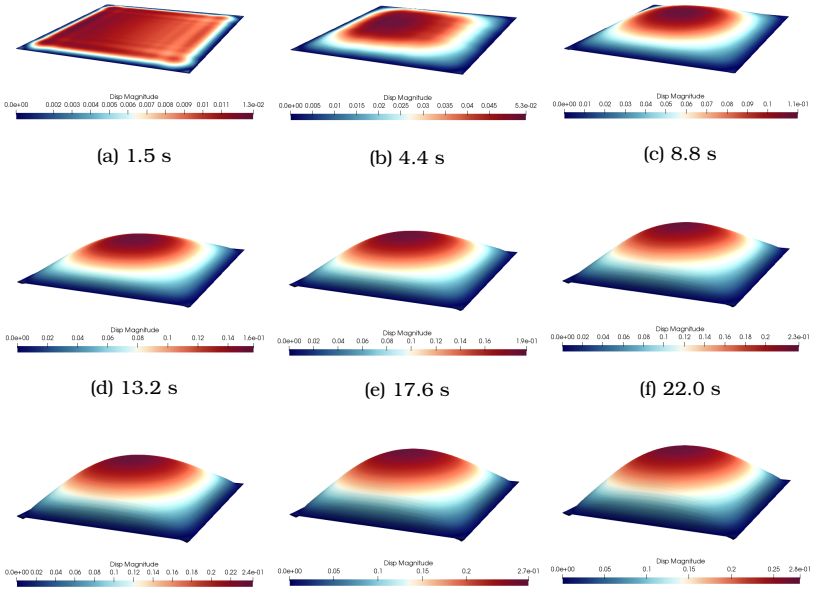

(a) 1.5 s (b) 4.4 s (c) 8.8 s

(d) 13.2 s (e) 17.6 s (f) 22.0 s

(g) 26.6 s (h) 31.0 s (i) 35.4 s

Figure 13.87: Plate displacement contours in time

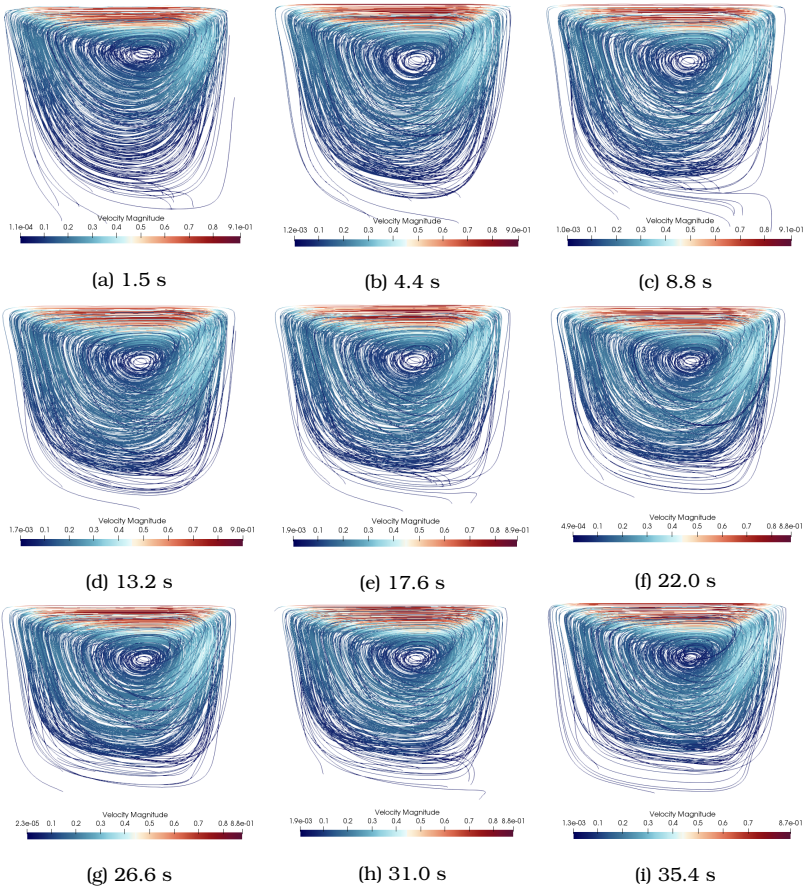

(a) 1.5 s (b) 4.4 s (c) 8.8 s

(d) 13.2 s (e) 17.6 s (f) 22.0 s

(g) 26.6 s (h) 31.0 s (i) 35.4 s

Figure 13.88: Fluid velocity streamlines in time

Finally figure 13.89 shows the full geometry at 26.6 seconds and as in the previous case, table 13.26 shows the reduction in terms of degrees of freedom. In this case the fluid needs more basis vectors than in the past case but still less than the solid.

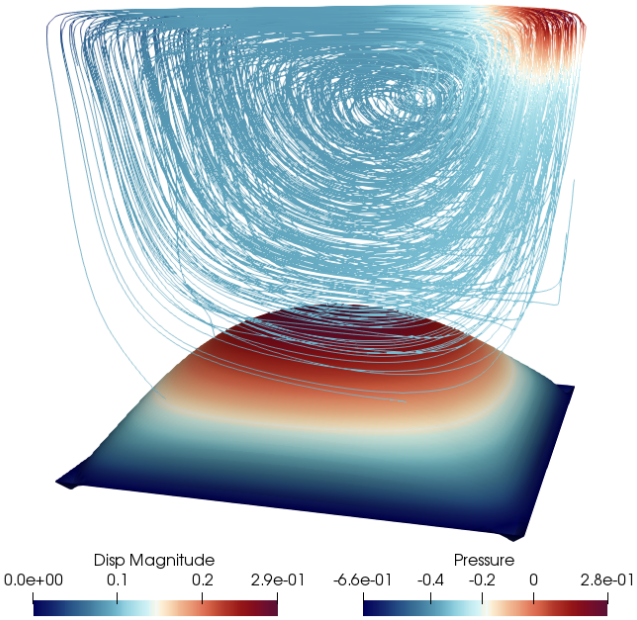

Figure 13.89: Velocity streamlines and plate displacement at t = 26.6s

	FOM	ROM	Reduction (%)
Fluid	198 963	52	99,974
Solid	14 884	68	99,543
Total			99,944

Table 13.26: DOF reduction

Accurate ROM results have been obtained for both test cases, each case highlighting a different kind of FSI behavior. In the first one, the solid is exposed to oscillatory velocity profiles. This kind of motion activates harmonic oscillation on the solid. This can be an issue on structures under wind loading as the exponential nature of resonance can destroy a building or cause critical damage. The same can be said about flutter on aerodynamic structures. The second case shows a constant fluid load on the solid which deforms one order of magnitude

more than the previous test case. Both of these examples show clearly one of the challenges of FSI modeling as greater deformations or more non-linear behavior is achieved greater computational time is required to solve the mathematical system and greater effort has to be made by the interface solver to successfully couple both domains.

SUMMARY

In this dissertation a displacement-stress-pressure formulation for a neo-Hookean solid using an updated Lagrangian formulation has been introduced, followed by a new three-field Fluid-Structure Interaction (FSI) formulation stabilized by means of a Variational Multi-Scale (VMS) approach using time dependent sub-grid scales on both the fluid and the solid regions. Benchmarking was done for the solid formulation under static and dynamic scenarios; on itself the solid three-field formulation proves to be more accurate and less time step dependent than its irreducible counterpart.

The three-field formulation has proved to be robust and precise under all cases analyzed. Compared to the irreducible formulation, it preserves phase and amplitude in time with fewer elements and even with linear elements. This formulation proves to be accurate and efficient, as it is possible to use a coarser mesh that produces more accurate results than its standard irreducible counterpart with a finer mesh.

Additionally a two-field elasto-dynamic formulation was introduced with the objective of completing our Field to Field (F2F) paired FSI models in order to compare three different types of coupling and their advantages. The two-field formulation proves to be more precise than the irreducible formulation with just one more degree of freedom but less so than its three-field counterpart. In fact in every test the two-field was in between the irreducible and three-field formulations.

We have as well proposed a Reduced Order Model (ROM) model for FSI problems based on the VMS framework. In comparison to the work done in [67], where the cases shown could be solved with a basis energy in the range of 80% to 95%, FSI problems seem to be much more sensitive to the amount of energy in the basis necessary

to achieve a solution sufficiently close to that of the FOM. It was found that even for the simplest of the cases shown, the problem would not produce any valuable solution with an energy percentage under 99.0% though this depends greatly in the kind of coupling used, the standard requiring the most amount of energy. It is possible that this hints to the importance of the high frequencies of the spectrum in the solution of a FSI problem. This remains to be studied further and it is an interesting topic for future work. Nevertheless, in spite of the stringent requirements in terms of retained energy by the ROM, the reduction of the number of DOF with respect to the FOM is still very remarkable.

Once the possibility of reducing drastically the number of DOF has been shown, we have not pursued an efficient implementation of the highly nonlinear problems involved in both the solid and the fluid domains. In particular, we have not implemented any hyper-reduction strategy, which should be used on top of the ROM we have proposed. This is critical in test cases with high number of degrees of freedom especially for three-field coupling.

Partitioned FSI problems have a series of restrictions, such as a maximum time step and the need of diffusive time integration schemes for the ALE framework [40], that must be met so as to minimize the effect of instabilities like the added mass effect. This in turn is also a restriction on the ROM, making FSI-ROM cases very dependent on how often a snapshot is taken to be able to capture enough of the physics of the problem while keeping instabilities out of the sampling. A richer basis consists of more basis vectors that contain higher frequencies, and in turn, produce a better approximation to the FOM problem. Again, correlating with the above, this hints to the dependency on the high frequency low energy modes at the end of the spectrum of the basis.

The VMS-ROM formulation we have proposed has been found to be accurate and efficient. From the theoretical point of view, it has the interesting feature that the ROM and the FOM problems are solved

exactly with the same formulation, only changing the spaces where the unknowns and the test functions belong.

While we cannot say yet for sure on what is needed or enough to guarantee stability by means of our ROM formulation as this is still a field of research in our group we can point to factors that affect stability (namely incompressibility stabilization during the ROM phase and time step sampling), factors that enabled us to achieve excellent numerical results.

Convergence test were done for FSI-ROM cases where it was seen that in the ROM space there is a threshold where a reduced problem will give meaningful results, before a solution will not be precise enough and after the solution will be polluted by the effects of over-fitting and will tend to differ form the Full Order Model (FOM). This threshold, though problem dependent, tends to be reduced for the irreducible formulation, larger for the two-field and quite large for the three-field (not even visible in the presented results), making the latter the most efficient as it counts with a wide range of applicability before over-fitting starts to affect the solution.

The performance, both in FOM and ROM spaces but specially in the latter, of the two-field FSI was shown to be superior to the standard coupling even though both use the same velocity–pressure formulation for the fluid. The gain in performance appears to be not from the type for formulation used but rather the type of coupling making F2F coupling worthwhile whenever possible.

The three-field formulation produces in the fluid a richer basis with higher magnitude than its counterparts. In the solid it produces a basis with marked modes. This hints at a better reduction of the problem achieved by a correct splitting of the stress tensor which in turn produces a more accurate reduced problem.

Overall the three-field formulation, both for solid and F2F coupling, proves to be superior, albeit more expensive, both in the FOM and ROM spaces in terms of accuracy. In any case given that this formulation

has been shown to be very resilient to time step, mesh and number of basis used it still remains competitive with regard to the other types of couplings. It was also seen that a mixed field coupling involving any three-field formulation will be more precise than its counterparts, the best one being the one with a three-field formulation in the solid. This is also convenient as generally the fluid is the one with the most amount of degrees of freedom. If a 2F/3F provides accurate results and computational cost is of concern then it should be preferred to its expensive counterpart the full three-field coupling.
It is intuitive to assume that given that there are three versions of the FSI problem both in FOM and ROM it is possible to apply the calculated basis from one problem to another. This idea can have various advantages which are:

- Basis calculated in the more accurate three-field problem applied to the standard problem: The idea in reduced order modeling is to run the most precise offline stage possible so the calculated basis can reproduce the original problem faithfully. In this way it makes sense to calculate it with the three-field approach. Then apply it to an online stage that is focused on performance, this is, it is the fastest possible, for which it makes sense to apply the standard coupling.

- Basis calculated in the less accurate standard problem applied to the more accurate three-field problem: There are real world applications in which the geometry dictates the size of the mesh to be used. High geometric detail can force a very high number of nodes. In this way running a FOM with the three-field coupling can become unfeasible as calculation times become very high. It can be calculated by means of the standard coupling and the online stage run with a more precise three-field approach that guarantees precision in the ROM stage.

Unfortunately neither of the two approaches worked readily meaning that some degree of processing and manipulation should be done to each basis so that it can be applied to another formulation of the FSI problem. This idea is left as future work.

OUTLOOK

The development of the VMS-ROM formulation into the FSI infrastructure and the additional techniques brought us some ideas that can be addressed in the future.

- Delve into manipulation of the basis calculated by these methods to be able to reproduce problems by means of other type of formulations, i.e: Calculate a basis by means of an standard problem and solve the ROM by means of a three field one.
- Apply hyper-reduction with the aim of improving the performance of the F2F problem.
- Look into other type of coupling conditions or mesh movement algorithms.
- Extend the F2F into non-Newtonian flows.

PUBLICATIONS

As a result of the research done in this dissertation we submitted three articles to peer-reviewed scientific journals, in each of them a major part of this dissertation is contained.

1. Tello, A. & Codina, R. *Field to Field coupled Fluid Structure Interaction: A Reduced Order Model study* 2020. Submitted.
2. Tello, A. & Codina, R. *Three Field Fluid Structure Interaction by means of the Variational Multiscale method* 2020. Submitted.
3. Tello, A., Codina, R. & Baiges, J. Fluid structure interaction by means of variational multiscale reduced order models. *International Journal for Numerical Methods in Engineering* **121,** 2601–2625. ISSN: 0029-5981. doi:10.1002/nme.6321 (2020).

BIBLIOGRAPHY

1. Ager, C., Schott, B., Winter, M. & Wall, W. A. A Nitsche-based cut finite element method for the coupling of incompressible fluid flow with poroelasticity. *Computer Methods in Applied Mechanics and Engineering* **351,** 253–280. ISSN: 00457825. doi:10.1016/j.cma.2019.03.015 (2019).
2. Akbay, M., Nobles, N., Zordan, V. & Shinar, T. An extended partitioned method for conservative solid-fluid coupling. *ACM Transactions on Graphics* **37,** 1–12. ISSN: 07300301. doi:10.1145/3197517.3201345 (2018).
3. Aubry, N. On the hidden beauty of the proper orthogonal decomposition. *Theoretical and Computational Fluid Dynamics* **2,** 339–352. ISSN: 09354964. doi:10.1007/BF00271473 (1991).
4. Badia, S., Nobile, F. & Vergara, C. Fluid–structure partitioned procedures based on Robin transmission conditions. *Journal of Computational Physics* **227,** 7027–7051. ISSN: 00219991. doi:10.1016/j.jcp.2008.04.006 (2008).
5. Baiges, J. & Codina, R. The fixed-mesh ALE approach applied to solid mechanics and fluid-structure interaction problems. *International Journal for Numerical Methods in Engineering* **81,** 1529–1557. ISSN: 00295981. doi:10.1002/nme.2740 (2009).
6. Baiges, J., Codina, R. & Idelsohn, S. A domain decomposition strategy for reduced order models. Application to the incompressible Navier–Stokes equations. *Computer Methods in Applied Mechanics and Engineering* **267,** 23–42. ISSN: 00457825. doi:10.1016/j.cma.2013.08.001 (2013).

7. Baiges, J., Codina, R. & Idelsohn, S. Explicit reduced-order models for the stabilized finite element approximation of the incompressible Navier-Stokes equations. *International Journal for Numerical Methods in Fluids* **72,** 1219–1243. ISSN: 02712091. doi:10.1002/fld.3777 (2013).

8. Baiges, J., Codina, R. & Idelsohn, S. Reduced-order subscales for POD models. *Computer Methods in Applied Mechanics and Engineering* **291,** 173–196. ISSN: 00457825. doi:10.1016/j.cma.2015.03.020 (2015).

9. Baiges, J., Codina, R., Pont, A. & Castillo, E. An adaptive Fixed-Mesh ALE method for free surface flows. *Computer Methods in Applied Mechanics and Engineering* **313,** 159–188. ISSN: 00457825. doi:10.1016/j.cma.2016.09.041 (2017).

10. Ballarin, F., Manzoni, A., Quarteroni, A. & Rozza, G. Supremizer stabilization of POD-Galerkin approximation of parametrized steady incompressible Navier-Stokes equations. *International Journal for Numerical Methods in Engineering* **102,** 1136–1161. ISSN: 00295981. doi:10.1002/nme.4772 (2015).

11. Ballarin, F. & Rozza, G. POD-Galerkin monolithic reduced order models for parametrized fluid-structure interaction problems. *International Journal for Numerical Methods in Fluids* **82,** 1010–1034. ISSN: 02712091. doi:10.1002/fld.4252 (2016).

12. Bazilevs, Y., Calo, V. M., Hughes, T. J. R. & Zhang, Y. Isogeometric fluid-structure interaction: theory, algorithms, and computations. *Computational Mechanics* **43,** 3–37. ISSN: 0178-7675. doi:10.1007/s00466-008-0315-x (2008).

13. Bazilevs, Y., Calo, V. M., Zhang, Y. & Hughes, T. J. R. Isogeometric Fluid–structure Interaction Analysis with Applications to Arterial Blood Flow. *Computational Mechanics* **38,** 310–322. ISSN: 0178-7675. doi:10.1007/s00466-006-0084-3 (2006).

14. Belytschko, T., Liu, W. K., Moran, B. & Elkhodary, K. *Nonlinear finite elements for continua and structures* in (ed Wiley) 2nd, 830 (Wiley, 2014). ISBN: 978-1-118-63270-3. doi:10.1016/S0065-230X(09)04001-9.

15. Bordère, S. & Caltagirone, J.-P. A unifying model for fluid flow and elastic solid deformation: A novel approach for fluid–structure interaction. *Journal of Fluids and Structures* **51,** 344–353. ISSN: 08899746. doi:10.1016/j.jfluidstructs.2014.09.010 (2014).

16. Bungartz, H. J., Mehl, M. & Schäfer, M. Lecture Notes in Computational Science and Engineering: Preface. *Lecture Notes in Computational Science and Engineering* **73 LNCSE.** ISSN: 14397358. doi:10.1007/978-3-642-14206-2 (2010).

17. Carlberg, K., Bou-Mosleh, C. & Farhat, C. Efficient non-linear model reduction via a least-squares Petrov-Galerkin projection and compressive tensor approximations. *International Journal for Numerical Methods in Engineering* **86,** 155–181. ISSN: 00295981. doi:10.1002/nme.3050 (2011).

18. Carlberg, K., Farhat, C., Cortial, J. & Amsallem, D. The GNAT method for nonlinear model reduction: Effective implementation and application to computational fluid dynamics and turbulent flows. *Journal of Computational Physics* **242,** 623–647. ISSN: 00219991. doi:10.1016/j.jcp.2013.02.028 (2013).

19. Castanar, I., Baiges, J. & Codina, R. A stabilized mixed finite element approximation for incompressible finite strain solid dynamics using a total lagrangian formulation. *submitted* (2019).

20. Castillo, E. Formulaciones de tres campos de elementos finitos estabilizados en fluidos reológicamente no- newtonianos (2015).

21. Castillo, E. & Codina, R. Stabilized stress–velocity–pressure finite element formulations of the Navier–Stokes problem for fluids with non-linear viscosity. *Computer Methods in Applied Mechanics and Engineering* **279,** 554–578. ISSN: 00457825. doi:10.1016/j.cma.2014.07.003 (2014).

22. Castillo, E. & Codina, R. Variational multi-scale stabilized formulations for the stationary three-field incompressible viscoelastic flow problem. *Computer Methods in Applied Mechanics and Engineering* **279,** 579–605. ISSN: 00457825. doi:10.1016/j.cma.2014.07.006 (2014).

23. Castillo, E. & Codina, R. Dynamic term-by-term stabilized finite element formulation using orthogonal subgrid-scales for the incompressible Navier–Stokes problem. *Computer Methods in Applied Mechanics and Engineering* **349,** 701–721. ISSN: 00457825. doi:10.1016/j.cma.2019.02.041 (2019).

24. Cervera, M., Chiumenti, M., Benedetti, L. & Codina, R. Mixed stabilized finite element methods in nonlinear solid mechanics. Part III: Compressible and incompressible plasticity. *Computer Methods in Applied Mechanics and Engineering* **285,** 752–775. ISSN: 00457825. doi:10.1016/j.cma.2014.11.040 (2015).

25. Cervera, M., Chiumenti, M. & Codina, R. Mixed stabilized finite element methods in nonlinear solid mechanics. *Computer Methods in Applied Mechanics and Engineering* **199,** 2571–2589. ISSN: 00457825. doi:10.1016/j.cma.2010.04.005 (2010).

26. Chiandussi, G., Bugeda, G. & Oñate, E. A simple method for automatic update of finite element meshes. *Communications in Numerical Methods in Engineering* **16,** 1–19. ISSN: 1069-8299. doi:10.1002/(SICI)1099-0887(200001)16:1<1::AID-CNM310>3.0.CO;2-A (2000).

27. Chiumenti, M., Cervera, M. & Codina, R. A mixed three-field FE formulation for stress accurate analysis including the incompressible limit. *Computer Methods in Applied Mechanics and Engineering* **283,** 1095–1116. ISSN: 00457825. doi:10.1016/j.cma.2014.08.004 (2015).

28. Codina, R. Stabilization of incompressibility and convection through orthogonal sub-scales in finite element methods. *Computer Methods in Applied Mechanics and Engineering* **190,** 1579–1599. ISSN: 00457825. doi:10.1016/S0045-7825(00)00254-1 (2000).

29. Codina, R. A stabilized finite element method for generalized stationary incompressible flows. *Computer Methods in Applied Mechanics and Engineering* **190,** 2681–2706. ISSN: 00457825. doi:10.1016/S0045-7825(00)00260-7 (2001).

30. Codina, R. Stabilized finite element approximation of transient incompressible flows using orthogonal subscales. *Computer Methods in Applied Mechanics and Engineering* **191,** 4295–4321. ISSN: 00457825. doi:10.1016/S0045-7825(02)00337-7 (2002).

31. Codina, R. Finite Element Approximation of the Three-Field Formulation of the Stokes Problem Using Arbitrary Interpolations. *SIAM Journal on Numerical Analysis* **47,** 699–718. ISSN: 0036-1429. doi:10.1137/080712726 (2009).

32. Codina, R., Badia, S., Baiges, J. & Principe, J. Variational multiscale methods in computational fluid dynamics. *Encyclopedia of Computational Mechanics Second Edition,* 1–28. doi:10.1002/9781119176817.ecm2117 (2018).

33. Codina, R., Principe, J. & Baiges, J. Subscales on the element boundaries in the variational two-scale finite element method. *Computer Methods in Applied Mechanics and Engineering* **198,**

838–852. ISSN: 00457825. doi:10.1016/j.cma.2008.10.020 (2009).

34. Codina, R., Principe, J., Guasch, O. & Badia, S. Time dependent subscales in the stabilized finite element approximation of incompressible flow problems. *Computer Methods in Applied Mechanics and Engineering* **196,** 2413–2430. ISSN: 00457825. doi:10.1016/j.cma.2007.01.002 (2007).

35. Donea, J., Huerta, A., Ponthot, J. P. & Rodriguez-Ferran, A. *Arbitrary Lagrangian-Eulerian Methods* in *Encyclopedia of Computational Mechanics* 1–25 (John Wiley & Sons, Ltd, Chichester, UK, 2004). ISBN: 0470846992. doi:10.1002/0470091355.ecm009.

36. Everson, R. & Sirovich, L. Karhunen–Loève procedure for gappy data. *Journal of the Optical Society of America A* **12,** 1657. ISSN: 1084-7529. doi:10.1364/JOSAA.12.001657 (1995).

37. Fan, J. *et al.* A monolithic Lagrangian meshfree scheme for Fluid–Structure Interaction problems within the OTM framework. *Computer Methods in Applied Mechanics and Engineering* **337,** 198–219. ISSN: 00457825. doi:10.1016/j.cma.2018.03.031 (2018).

38. Farhat, C. & Lakshminarayan, V. K. An ALE formulation of embedded boundary methods for tracking boundary layers in turbulent fluid-structure interaction problems. *Journal of Computational Physics* **263,** 53–70. ISSN: 00219991. doi:10.1016/j.jcp.2014.01.018 (2014).

39. Farhat, C., van der Zee, K. G. & Geuzaine, P. Provably second-order time-accurate loosely-coupled solution algorithms for transient nonlinear computational aeroelasticity. *Computer Methods in Applied Mechanics and Engineering* **195,** 1973–2001. ISSN: 00457825. doi:10.1016/j.cma.2004.11.031 (2006).

40. Forster, C. *Robust methods for fluid-structure interaction with stabilised finite elements* PhD thesis. Universitat Stuttgart, 2007. Available at:

41. Förster, C., Wall, W. A. & Ramm, E. Artificial added mass instabilities in sequential staggered coupling of nonlinear structures and incompressible viscous flows. *Computer Methods in Applied Mechanics and Engineering* **196,** 1278–1293. ISSN: 00457825. doi:10.1016/j.cma.2006.09.002 (2007).

42. Fortin, M, Pierre, R & K, C. G. On the convergence of the mixed method of Crochet and Marchal for viscoelastic flows. *Computer Methods in Applied Mechanics and Engineering* **73,** 341–350 (1989).

43. Francesco Ballarin, G. R. & Maday, Y. *Reduced-Order Semi-Implicit Schemes for Fluid-Structure Interaction Problems* in *Journal of Scientific Computing* (eds Benner, P. *et al.*) *MS&A* 2-3, 149 –167 (Springer International Publishing, Cham, 2017). ISBN: 978-3-319-58785-1. doi:10.1007/978-3-319-58786-8.

44. Garelli, L., Paz, R. R. & Storti, M. A. Fluid-structure interaction study of the start-up of a rocket engine nozzle. *Computers and Fluids* **39,** 1208–1218. ISSN: 00457930. doi:10.1016/j.compfluid.2010.03.005 (2010).

45. Glowinski, R., Basting, S. & Quaini, A. Extended ALE Method for fluid–structure interaction problems with large structural displacements. *Journal of Computational Physics* **331,** 312–336. doi:10.1016/j.jcp.2016.11.043 (2017).

46. Hou, G., Wang, J. & Layton, A. Numerical methods for fluid-structure interaction - A review. *Communications in Computational Physics* **12,** 337–377. ISSN: 18152406. doi:10.4208/cicp.291210.290411s (2012).

47. Houzeaux, G. & Codina, R. Transmission conditions with constraints in finite element domain decomposition methods for flow problems. *Communications in Numerical Methods in Engineering* **17,** 179–190. ISSN: 10698299. doi:10.1002/cnm.397 (2001).

48. Hughes, T. J. R., Feijóo, G. R., Mazzei, L. & Quincy, J.-B. The variational multiscale method—a paradigm for computational mechanics. *Computer Methods in Applied Mechanics and Engineering* **166,** 3–24. ISSN: 00457825. doi:10.1016/S0045-7825(98)00079-6 (1998).

49. Iliescu, T. & Wang, Z. Variational multiscale proper orthogonal decomposition: Navier-stokes equations. *Numerical Methods for Partial Differential Equations* **30,** 641–663. ISSN: 0749159X. doi:10.1002/num.21835 (2014).

50. Irons, B. M. & Tuck, R. C. A version of the Aitken accelerator for computer iteration. *International Journal for Numerical Methods in Engineering* **1,** 275–277. ISSN: 0029-5981. doi:10.1002/nme.1620010306 (1969).

51. Kalashnikova, I., Barone, M. & Brake, M. A stable Galerkin reduced order model for coupled fluid-structure interaction problems. *International Journal for Numerical Methods in Engineering* **95,** 121–144. ISSN: 00295981. doi:10.1002/nme.4499 (2013).

52. Kamakoti, R. & Shyy, W. Fluid-structure interaction for aeroelastic applications. *Progress in Aerospace Sciences* **40,** 535–558. ISSN: 03760421. doi:10.1016/j.paerosci.2005.01.001 (2004).

53. Küttler, U. & Wall, W. A. Fixed-point fluid-structure interaction solvers with dynamic relaxation. *Computational Mechanics* **43,** 61–72. ISSN: 01787675. doi:10.1007/s00466-008-0255-5 (2008).

54. La Spina, A., Förster, C., Kronbichler, M. & Wall, W. A. On the role of (weak) compressibility for fluid-structure interaction solvers. *International Journal for Numerical Methods in Fluids* **92,** 129–147. ISSN: 10970363. doi:10.1002/fld.4776 (2020).

55. Langer, U. & Yang, H. Partitioned solution algorithms for fluid–structure interaction problems with hyperelastic models. *Journal of Computational and Applied Mathematics* **276,** 47–61. ISSN: 03770427. doi:10.1016/j.cam.2014.08.007 (2015).

56. Le Tallec, P. Fluid structure interaction with large structural displacements. *Computer Methods in Applied Mechanics and Engineering* **190,** 3039–3067. ISSN: 00457825. doi:10.1016/S0045-7825(00)00381-9 (2001).

57. Leong, W. C., Abdullah, M. Z., Khor, C. Y. & Ong, E. E. S. Study on the fluid-structure interaction of flexible printed circuit board electronics in the flow environment. *IEEE Transactions on Components, Packaging and Manufacturing Technology* **2,** 1335–1345. ISSN: 21563950. doi:10.1109/TCPMT.2012.2201939 (2012).

58. Lieu, T., Farhat, C. & Lesoinne, M. Reduced-order fluid/structure modeling of a complete aircraft configuration. *Computer Methods in Applied Mechanics and Engineering* **195,** 5730–5742. ISSN: 00457825. doi:10.1016/j.cma.2005.08.026 (2006).

59. Lumley, J. *Coherent structures in turbulent flow* in *The Role of Coherent Structures in Modelling Turbulence and Mixing* (ed.), Berlin, Fed. Rep. Germany, Springer-Verlag, 1981, Session 1-Theory, p.1-9. (Lecture Notes in, 1–9 (Springer Berlin Heidelberg, Berlin, Heidelberg, 1981). ISBN: 3540102892. doi:10.1016/B978-0-12-493240-1.50017-X.

60. Marchal, J. & Crochet, M. A new mixed finite element for calculating viscoelastic flow. *Journal of Non-Newtonian Fluid Mechanics*

26, 77–114. ISSN: 03770257. doi:10.1016/0377-0257(87)85048-6 (1987).

61. Matthies, H. G. & Steindorf, J. Partitioned strong coupling algorithms for fluid-structure interaction. *Computers and Structures* **81,** 805–812. ISSN: 00457949. doi:10.1016/S0045-7949(02)00409-1 (2003).

62. Mayr, M., Wall, W. A. & Gee, M. W. Adaptive time stepping for fluid-structure interaction solvers. *Finite Elements in Analysis and Design* **141,** 55–69. ISSN: 0168874X. doi:10.1016/j.finel.2017.12.002 (2018).

63. Mayr, M., Klöppel, T., Wall, W. A. & Gee, M. W. A temporal consistent monolithic approach to fluid-structure interaction enabling single field predictors. *SIAM Journal on Scientific Computing* **37,** B30–B59. ISSN: 10957200. doi:10.1137/140953253 (2015).

64. Moreno, L., Codina, R., Baiges, J. & Castillo, E. Logarithmic conformation reformulation in viscoelastic flow problems approximated by a VMS-type stabilized finite element formulation. *Computer Methods in Applied Mechanics and Engineering* **354,** 706–731. ISSN: 00457825. doi:10.1016/j.cma.2019.06.001 (2019).

65. Pasquariello, V. *et al.* A cut-cell finite volume - finite element coupling approach for fluid-structure interaction in compressible flow. *Journal of Computational Physics* **307,** 670–695. ISSN: 10902716. doi:10.1016/j.jcp.2015.12.013 (2016).

66. Reyes, R. & Codina, R. Element boundary terms in reduced order models for flow problems : domain decomposition and adaptive coarse mesh. *Submitted,* 1–32 (2019).

67. Reyes, R., Codina, R., Baiges, J. & Idelsohn, S. Reduced order models for thermally coupled low Mach flows. *Advanced Modeling*

and Simulation in Engineering Sciences **5,** 28. ISSN: 2213-7467. doi:10.1186/s40323-018-0122-7 (2018).

68. Richter, T. A monolithic geometric multigrid solver for fluid-structure interactions in ALE formulation. *International Journal for Numerical Methods in Engineering* **104,** 372–390. ISSN: 00295981. doi:10.1002/nme.4943 (2015).

69. Ruas, V. Une methode mixte contrainte-deplacement-pression pour la resolution de problemes de viscoelasticite incompressible en deformations planes. *Comptes rendus de l'Acad\'emie des Sciences. S\'erie 2* **301,** 1171–1174 (1985).

70. Ruas, V. Finite element methods for the three-field Stokes system. *RAIRO Modelisation Mathematique et Analyse Numerique* **30,** 489–525 (1996).

71. Ryckelynck, D. A priori hyperreduction method: an adaptive approach. *Journal of Computational Physics* **202,** 346–366. ISSN: 00219991. doi:10.1016/j.jcp.2004.07.015 (2005).

72. Sandri, D. Analyse d'une formulation à trois champs du problème de Stokes. *RAIRO Mod\'elisation Math\'ematique et Analyse Num\'erique* **23,** 817–841 (1993).

73. Sauer, R. A. & Luginsland, T. A monolithic fluid–structure interaction formulation for solid and liquid membranes including free-surface contact. *Computer Methods in Applied Mechanics and Engineering* **341,** 1–31. ISSN: 00457825. doi:10.1016/j.cma.2018.06.024 (2018).

74. Schilders, W. *Introduction to Model Order Reduction* in *Model Order Reduction: Theory, Research Aspects and Applications. Mathematics in Industry (The European Consortium for Mathematics in Industry)* 3–32 (Springer, Berlin, Heidelberg, 2008). ISBN: 978-3-540-78840-9, 978-3-540-78841-6. doi:10.1007/978-3-540-78841-6{_}1.

75. Schott, B., Ager, C. & Wall, W. A. A monolithic approach to fluid-structure interaction based on a hybrid Eulerian-ALE fluid domain decomposition involving cut elements. *International Journal for Numerical Methods in Engineering* **119,** 208–237. ISSN: 10970207. doi:10.1002/nme.6047 (2019).

76. Scovazzi, G., Song, T. & Zeng, X. A velocity/stress mixed stabilized nodal finite element for elastodynamics: Analysis and computations with strongly and weakly enforced boundary conditions. *Computer Methods in Applied Mechanics and Engineering* **325,** 532–576. ISSN: 00457825. doi:10.1016/j.cma.2017.07.018 (2017).

77. Shangguan, W. B. & Lu, Z. H. Experimental study and simulation of a hydraulic engine mount with fully coupled fluid-structure interaction finite element analysis model. *Computers and Structures* **82,** 1751–1771. ISSN: 00457949. doi:10.1016/j.compstruc.2004.05.017 (2004).

78. Sirovich, L. & Kirby, M. Low-dimensional procedure for the characterization of human faces. *Journal of the Optical Society of America A* **4,** 519. ISSN: 1084-7529. doi:10.1364/JOSAA.4.000519 (1987).

79. Stabile, G., Ballarin, F., Zuccarino, G. & Rozza, G. A reduced order variational multiscale approach for turbulent flows. *Advances in Computational Mathematics*. ISSN: 1019-7168. doi:10.1007/s10444-019-09712-x (2019).

80. Sudhakar, Y. & Wall, W. A. A strongly coupled partitioned approach for fluid-structure-fracture interaction. *International Journal for Numerical Methods in Fluids* **87,** 90–108. ISSN: 10970363. doi:10.1002/fld.4483 (2018).

81. Takizawa, K., Bazilevs, Y. & Tezduyar, T. E. Space–Time and ALE-VMS Techniques for Patient-Specific Cardiovascular

Fluid–Structure Interaction Modeling. *Archives of Computational Methods in Engineering* **19,** 171–225. ISSN: 1134-3060. doi:10.1007/s11831-012-9071-3 (2012).

82. Thari, A., Pasquariello, V., Aage, N. & Hickel, S. Adaptive Reduced-Order Modeling for Non-Linear Fluid-Structure Interaction, 1–25 (2017).

83. Turek, S. & Hron, J. *Proposal for Numerical Benchmarking of Fluid-Structure Interaction between an Elastic Object and Laminar Incompressible Flow* in *Fluid-Structure Interaction* 371–385 (Springer Berlin Heidelberg, Berlin, Heidelberg, 2006). ISBN: 978-3-540-34595-4. doi:10.1007/3-540-34596-5{_}15.

84. Van Brummelen, E. H. Partitioned iterative solution methods for fluid-structure interaction. *International Journal for Numerical Methods in Fluids* **65,** 3–27. ISSN: 02712091. doi:10.1002/fld.2465 (2011).

85. Vierendeels, J., Lanoye, L., Degroote, J. & Verdonck, P. Implicit coupling of partitioned fluid-structure interaction problems with reduced order models. *Computers and Structures* **85,** 970–976. ISSN: 00457949. doi:10.1016/j.compstruc.2006.11.006 (2007).

86. Wall, W. A., Mok, D. P. & Ramm, E. *Iterative Substructering Schemes for Fluid Structure Interaction* in *Lecture Notes in Applied and Computational Mechanics* 349–360 (2003). ISBN: 9783642056338. doi:10.1007/978-3-540-36527-3{_}43.

87. Wang, W. Q. & Yan, Y. Strongly coupling of partitioned fluid-solid interaction solvers using reduced-order models. *Applied Mathematical Modelling* **34,** 3817–3830. ISSN: 0307904X. doi:10.1016/j.apm.2010.03.022 (2010).

88. Zheng, L., Chen, Y., Chang, S. & Haoxiang, L. A Reduced-Order Flow Model for Fluid–Structure Interaction Simulation of Vocal Fold Vibration. *Journal of Biomechanical Engineering* **142.** doi:10.1115/1.4044033 (2019).

A LINEARIZATION OF CERTAIN TERMS

We can write any variable x in terms of its increment δx in the following form,

$$x = \tilde{x} + \delta x, \tag{A.1}$$

where $\tilde{x}$ is a previously known value of x. By means of equation (A.1) we can express the displacement gradient tensor as,

$$F_{iJ} = \frac{\partial x_i}{\partial X_J} = F_{iJ} = \frac{\partial X_I + u_i}{\partial X_J} = \delta_{IJ} + \frac{\partial u_i}{\partial X_J}. \tag{A.2}$$

Preserving all first order terms:

$$\begin{aligned} F_{iJ} &= \frac{\partial x_i}{\partial X_J} = F_{iJ} = \frac{\partial X_I + u_i}{\partial X_J} = \delta_{IJ} + \frac{\partial u_i}{\partial X_J} == \delta_{IJ} + \frac{\partial \tilde{u}_i + \delta d_i}{\partial X_J}, \\ F_{iJ} &= \tilde{F}_{iJ} + \frac{\partial \delta d_i}{\partial X_J}. \end{aligned} \tag{A.3}$$

Applying equation (A.3) we can define the linearization of the left-Cauchy tensor up to first order as:

$$\begin{aligned} b_{ij} &= F_{iK}F_{jK} \approx \left(\tilde{F}_{iK} + \frac{\partial \delta d_i}{\partial X_K}\right)\left(\tilde{F}_{jK} + \frac{\partial \delta d_j}{\partial X_K}\right), \\ b_{ij} &= \tilde{b}_{ij} + \tilde{F}_{iK}\frac{\partial \delta d_j}{\partial X_K} + \frac{\partial \delta d_i}{\partial X_K}\tilde{F}_{jK}, \end{aligned} \tag{A.4}$$

Once we have b_{ij} linearized its trace can be obtained readily as:

$$b_{ii} = \tilde{b}_{ii} + 2\tilde{F}_{iK}\frac{\partial \delta d_i}{\partial X_K}. \tag{A.5}$$

The determinant J of F_{iJ} can be obtained as follows:

$$\begin{aligned} J = \det F_{iJ} &= \det\left(\tilde{F}_{iJ} + \frac{\partial \delta d_i}{\partial X_J}\right), \\ &= \det\left[\tilde{F}_{iK}\left(\delta_{KJ} + \tilde{F}^{-1}_{Kl}\frac{\partial \delta d_l}{\partial X_J}\right)\right], \end{aligned}$$

where by means of the multiplicative property of determinants we can express the previous expression as

$$J = \tilde{J}\det\left(\delta_{KJ} + \tilde{F}^{-1}_{Kl}\frac{\partial \delta d_l}{\partial X_J}\right),$$

If we construct this determinant we notice that by discarding higher order terms we are left with the trace of said matrix:

$$J = \tilde{J}\left(1 + \tilde{F}^{-1}_{Ji}\frac{\partial \delta d_i}{\partial X_J}\right), \tag{A.6}$$

Finally, using the previous result we can linearize the logarithm of the determinant of the displacement gradient:

$$\begin{aligned}\ln(J) &= \ln\left[\tilde{J}\left(1 + \tilde{F}^{-1}_{Ji}\frac{\partial \delta d_i}{\partial X_J}\right)\right],\\ &= \ln(\tilde{J}) + \ln\left[\left(1 + \tilde{F}^{-1}_{Ji}\frac{\partial \delta d_i}{\partial X_J}\right)\right]\end{aligned}$$

whereby using the fact that for small increments the series $\ln(1+x) = x$ we can express the previous result as:

$$\ln(J) = \ln(\tilde{J}) + \tilde{F}^{-1}_{Ji}\frac{\partial \delta d_i}{\partial X_J}, \tag{A.7}$$